Spin Effects of Excited States in Organic Semiconductors and Hybrid Perovskites for Optoelectronics and Spintronics

A Dissertation Presented for the
Doctor of Philosophy
Degree
The University of Tennessee, Knoxville

Miaosheng Wang

May 2021

I dedicate this dissertation to my parents.

Acknowledgment

Firstly, I would like to express my sincere gratitude to my Ph.D. advisor, Dr. Bin Hu, for his significant support, valuable advice, and insightful guidance in my research work. I would also like to thank my Ph.D. dissertation committee members, Dr. Tessa Calhoun, Dr. Mahshid Ahmadi, and Dr. David Mandrus for their constructive comments and valuable advice on my Ph.D. proposal and dissertation. I would like to give my special thanks to Dr. Claudia Rawn, as the director for the Center for Materials Processing (CMP) at the University of Tennessee, for the funding supporting of my Ph.D. studies.

I wish to devote my gratitude to all of my collaborators who made great contributions to my research work. I truly appreciate Dr. Stefan Haacke for providing me the great opportunity on learning and conducting ultrafast laser spectroscopy studies in Institut de Physique et Chimie des Matériaux de Strasbourg (IPCMS) at the summer of 2018. I also want to thank the tremendous help great friendship from Mr. Han Zou during my visit in France.

I would also like to thank the beamline scientists Dr. Valeria Lauter and Dr. Haile Ambaye in Spallation Neutron Source (SNS), Oak Ridge National Laboratory (ORNL) for their great support and guidance in helping me perform the most elegant experimental studies with neutron beam. I benefit a lot from this research experience in SNS. I also want to acknowledge additional two staff scientists from ORNL, Dr. Jong Keum and Dr. Ilia Ivanov for their significant help in performing experimental studies, analyzing data, and discussing results.

In particular, I would like to express my great appreciation to Dr. Ken-Tsung Wong at National Taiwan University and Dr. Shun-Wei Liu at Ming Chi University of Technology for their significant help in providing the materials and devices, discussing the results, and revising the manuscripts to support my studies. I also like to thank Dr. Kwang-Sup Lee at Hannam University for providing the materials to support my research.

I am particularly grateful to the former labmates, Dr. Yu-Che Hsiao, Dr. Mingxing Li, Dr. Qing Liu, Dr. Ting Wu, Dr. Wei Qin, Dr. Shengbo Ma, Dr. Jeremy Tisdale, and Dr. Hengxing Xu for helping me in my Ph.D. research studies. My gratitude also goes to all of the present group members, Jia Zhang, Yongtao Liu, Yixuan Dou, and Bogdan Dryzhakov for their great help and friendship.

Finally, I owe my greatest thankfulness to my parents and my wife Ling for their tremendous love, support, and understanding during my Ph.D. studies.

Abstract

Organic semiconductors and organic-inorganic hybrid perovskites have demonstrated versatile functionalities for optoelectronic and spintronic applications. Research in this dissertation focuses on the spin effects of excited states in emerging organic semiconductor and hybrid perovskite systems to understand the fundamental working principle. The investigation on the spin effects in excited states can provide insightful guidance for the development of the next-generation organic and hybrid perovskite optoelectronics and spintronics.

In organic semiconductors, the excited states, namely, excitons can be characterized by the total spin angular momentum $\mathbf{S}=\mathbf{S_e}+\mathbf{S_h}$ of the constituent electron and hole, which determines the spin states of singlets and triplets. In chapter 2, magneto-optical effects were investigated in organic optoelectronic devices including microcavity organic light-emitting diodes (OLEDs) and single active layer organic photovoltaic devices. It has been demonstrated that magneto-optical effects can function as the in-operando technique to reveal the spin-related optoelectronic processes in devices by directly changing the spin states. Inspired by the successful demonstration of magneto-optical effects in organics, the comprehensive magneto-optical studies were performed in newly emerging thermally activated delayed fluorescence (TADF) molecules with intramolecular charge-transfer states to provide an in-depth understanding on the spin-dependent reverse intersystem crossing (rISC) process from triplets to singlets. The spin-orbital coupling (SOC) was experimentally revealed to be the dominating spin-mixing mechanism in TADF process, responsible for the efficient rISC to harvest non-radiative triplet states. In chapter 4, spin, energy, and polarization parameters were systemically investigated in exciplex systems with intermolecular charge-transfer states. It was found that spin, energy, and polarization parameters can develop the cooperative relationship in exciplex systems for high-efficiency OLEDs. Moreover, in the exciplex hosted iridium complexes doped systems, the extended polarization memory was revealed to be the key factor in determining the device efficiency through enhanced light out-coupling.

With total angular momentum $\boldsymbol{J}$ in organic-inorganic hybrid perovskites, spin ($\boldsymbol{J}$) states can be manipulated through optical methods. Optically induced magnetization through photoexcited spin states at perovskite/ferromagnet interface was demonstrated in chapter 5. It was found that

optically generated spin (***J***) states in perovskite by using circularly polarized photoexcitation can directly interact with the ferromagnet layer to induce magnetization in perovskite. In chapter 6, spin relaxation dynamics were investigated by using ultrafast laser spectroscopy. The long spin lifetime in nanoseconds was realized in quasi-2D hybrid perovskite at room temperature, which represents a new opportunity to control the optoelectronic processes by using spin states in hybrid perovskites.

Table of Contents

List of Tables

List of Figures

Chapter 1 Introduction

1.1 Magnetic field effects in organic semiconductors

Magnetic field effects (MFEs) are defined as the changes caused by the applied magnetic field in a variety of properties such as photoluminescence, photocurrent, electroluminescence, resistance, and capacitance *et al*.[1, 2] The sign and amplitude of the MFE signals are represented by

$$MFE=(S_B-S_0)/S_0$$

where S_B and S_0 are signals with and without magnetic field. Half a century ago, MFEs on delayed fluorescence and chemical reaction were discovered in non-magnetic organic semiconducting materials.[3, 4] In the past decade, extensive MFEs have been observed on many properties both in organic spin-valve devices by incorporating ferromagnetic electrodes and intrinsic organic semiconductors. Due to the weak spin-orbital coupling (SOC) resulting from light elements in organic materials, the spin relaxation time is expected to be much longer than inorganic semiconductors, which is promising for spintronic applications.[5] Researchers then realized organic semiconductors can be used as a space layer sandwiched by two ferromagnetic electrodes with different coercive fields to develop organic spin-valve devices. The first experimental evidence of spin-polarized injection in organic semiconductors was reported by using a device with the structure of LSMO/sexithienyl/LSMO in 2002.[6] Two years later, the organic spin-valves based on LSMO/Alq_3/Co devices was first demonstrated with giant magnetoresistance (GMR) to show the spin-polarized carrier injection, transport, and detection.[7] Following a different strategy without coupling with the ferromagnetic electrode, MFEs from pure organic semiconductors were observed in many systems focused on different properties. In 1992, it was observed that an applied magnetic field can enhance the photocurrent in PPV film.[8] Later on, Kalinowski and coworkers demonstrated that electroluminescence and current in Alq_3 based device can be improved up to 5% and 3% with the weak applied magnetic field.[9] Large magnetoresistance was found in π-conjugated organic semiconductor thin-film devices at room temperature without using the ferromagnetic electrode.[10] Recently, Zang *et.al* discovered the magneto-dielectric effect in an organic donor: acceptor system which can be mediated by photoexcitation.[11] Distinguished from the organic spin-valve with the application of

ferromagnetic electrodes, MFEs on intrinsic organic semiconductors are strongly believed to be related to the spin process in excited states, charge transport, and electrical polarization.

MFEs have been proved to be a convenient method for studying excited states behaviors in organic semiconductors especially under steady-state or device operating condition. Despite the absence of magnetic elements, organic semiconductors show tremendous magnetic field-sensitive properties at relatively small magnetic fields within 1 Tesla (T). The desire to ravel the new spin physics motivates intensive experimental and theoretical research in MFEs during the past decade. Meanwhile, monitoring the spin-related processes provides a critical understating on the fundamental process in organic optoelectronics such as organic photovoltaic devices, light-emitting diodes (LEDs), and thin-film transistors, *etc*.

1.1.1 Excited states in organic semiconductors

The absorption of light in semiconductors can lead to the formation of bound electron-hole pairs known as excitons. In general, excitons can be classified as Wannier type and Frenkel type, commonly found in inorganic and organic semiconductors, respectively.[12, 13] Wannier exciton is more extended in crystalline structure with small binding energy around 10 meV and a large Bohr radius around 10 nm. On the contrary, Frenkel exciton in organic semiconductors is highly localized in molecules with large binding energy around 1 eV and a small Bohr radius around 1 nm. The closely bound excitonic states in organic semiconductors can subsequently dissociate into pairs of spatially separated charges in donor: acceptor system to form charge-transfer (CT) states. CT states can be divided into intermolecular type, when electron and hole are located at donor: acceptor interface on neighboring molecules, and intramolecular type, when electron and hole are located in a single molecule with donor and acceptor moieties. Similar to CT states, polaron pair and exciplex can be considered as loosely bound electron-hole pairs. It is known that organic materials usually are softer than inorganic materials because of the weak interaction between polymer chains or neighbor molecules originating from Van der Vaals forces. Therefore, the hopping type transportation of charge carriers can induce distortion in organic semiconductors, forming a charged quasi-particle named polaron. When two oppositely charged polarons on polymer chains or adjacent molecules are combined through Coulomb interaction, a polaron pair

is formed. Polaron pair can relax to a more tightly bound state with lower energy called an exciplex. In the exciplex state, the electron and hole polarons reside near neighboring acceptor and donor molecules.

At the same time, we can also classify the excited states by considering their spin configurations. Both electron and hole can carry spins and the paired electron-hole can form antiparallel and parallel spin orientations, leading to singlet and triplet states. The ground state for most of the organic semiconductors is a singlet ground state with the total spin quantum number zero (S=0). The spin quantum selection rule forbids the transition of triplet states with S=1 to the singlet ground states. Because of the same reason, triplet excitons usually cannot be directly excited by the photoexcitation. On the contrary, the electrically injected electrons and holes can form singlet exciton and triplet exciton with a ratio of 1:3 through a random capture process based on the spin statistics without considering spin interactions.[14, 15] Singlets can either recombine to ground states or transfer into long-lived triplets by flipping the spin through the intersystem crossing (ISC) process. Spin flipping is forbidden due to the spin selection rule. However, internal magnetic interactions such as spin-orbital coupling (SOC) and hyperfine interaction (HFI) can break the spin selection rule and realize ISC through spin-mixing between singlets and triplets.[16, 17] Exchange interactions generate the energy barrier between different spin states and serve as a competing mechanism to suppress the ISC through spin-conserving process. Generally, exchange interactions and magnetic interactions can act on different excited states in the form of paired electron-hole including excitons, CT states, polaron pairs, exciplex, *etc*.

Exchange interaction and internal magnetic interaction are believed to play an important role in the context of MFEs in organic semiconductors. Generally, the exchange interaction, responsible for spin conserving, and internal magnetic interaction, responsible for spin mixing, disallows and allows the intersystem crossing between singlets and triplets in electron-hole pairs, respectively. The competition between exchange interactions and internal magnetic interactions establishes a dynamic equilibrium on the singlet and triplet populations. When an external magnetic field is comparable to the exchange interactions or magnetic interactions, it can break the equilibrium between singlets and triplets, changing the singlet/triplet ratio to generate MFEs. Therefore, the

understanding of spin conserving and spin mixing behaviors provides the necessary condition for the discussion of MFEs in organic semiconductors.

1.1.2 Magneto-photoluminescence

Magneto-photoluminescence (magneto-PL) refers to the phenomenon that photoluminescence intensity is changed by an applied magnetic field. Generally, photoluminescence can be generated from both intermolecular and intramolecular excited states under photoexcitation. When a magnetic field changes the singlet and triplet population ratio in intermolecular and intramolecular excited states, magneto-PL can be observed due to the different recombination rates of singlet and triplet excited states. Magneto-PL can be used as an effective experimental tool to investigate the spin-dependent excited states formation, charge dissociation, and recombination process of organic semiconductors. Furthermore, exploring the fundamental mechanism of the magneto-optical phenomenon can lead to the development potential application of light and magnetic field sensing based on organic light-emitting materials.

Intermolecular excited states such as CT complex, excimer, and exciplex, are formed with long electron-hole separation distance resulting in weak exchange interaction, while intramolecular excited states are considered as Frenkel excitons with short electron-hole separation distance can have strong exchange interaction. Experimental studies have revealed that the realization of spin-dependent intramolecular excited states formation requires a large magnetic field at low temperature or incorporation of magnetic structures. In contrast, tuning singlet/triplet ratio of intermolecular excited states can be achieved under a low magnetic field at room temperature through field-dependent ISC. Besides, the deviation of Lande's *g* factor was considered a feasible mechanism to generate magneto-PL in excited states.[18, 19] The *g* factor of positive and negative polarons can be differently deviated from the *g* factor of free electrons under magnetic field due to the different Larmor frequencies, generating ISC.

1.1.3 Magneto-electroluminescence

Magneto-electroluminescence (magneto-EL) refers to the magnetic field-induced change on the steady-state electroluminescence in light-emitting devices through electrically formed excited

states. In 2003, it was first discovered that the current and light output can be improved up to 5 % and 3 % with an external magnetic field in Alq_3 based device organic light-emitting diodes (OLEDs).[9] The authors proposed that the external magnetic field can increase the light-emitting singlet states in polaron-pairs based on Zeeman splitting effect. Recently, this phenomenon started to receive increasing attention due to the demonstration of the third generation of organic light-emitting materials based on thermally activated delayed fluorescence (TADF) and the urgent need to understand the related spin dynamics.[18-20]

In general, the operation of OLEDs is composed of four fundamental processes: i) injection of charge carriers from electrodes; ii) transport of charge carriers under electric field; iii) formation of bounded electron-hole pairs as excited states; iv) Radiative recombination of excitons and light emission. During the operation, the electrons and holes are injected into the highest occupied molecular orbital (HOMO) and lowest unoccupied molecular orbital (LUMO), respectively. When the distance of oppositely charged carriers is smaller than their Coulomb capture radius in the organic materials, they can firstly form loosely bound electron-hole pairs including polaron pairs, CT states, and exciplex states in different systems. Those coulombically bound electron-hole pairs generally have large charge separation distances and can be located on the different molecules or the different segments of the same molecules. Subsequently, the electron-hole pairs can evolve into closely bound Frenkel excitonic states due to the Coulombic attraction. The radiative recombination of excitons generates the electroluminescence outcome. We know that random electron and hole capture through electrical injection generates 25% spin antiparallel states (singlets) and 75% spin parallel states (triplets) based on spin statistics. The ISC between singlets and triplets generally occurs within the electron-hole pairs because of the small exchange energy, as shown in **Figure 1-1**. An external magnetic field can change the ISC in electron-hole pairs but has little influence on the ISC in excitonic states, named as field-dependent and -independent ISC, respectively. The field-dependent ISC can result in a change in singlet and triplet ratio, consequently leading to magneto-electroluminescence.

Magneto-PL can be measured in constant voltage and constant current conditions [20], in which constant voltage mode usually gives larger magneto-PL than the constant current mode. The electroluminescence intensity, *EL*, can be written as

$$EL \propto \eta I$$

where η is the quantum efficiency of electroluminescence and *I* is the injection current. Therefore, the change in either quantum efficiency or injection can result in the change in the total electroluminescence. In constant voltage mode, the external magnetic field can influence both electroluminescence quantum efficiency of excited states and the density of excited states through injection current. In constant current mode, the magneto-PL directly comes from the perturbed quantum efficiency through the population change on singlets and triplets while the density of excited states remains barely unchanged. Thus, the magnetic field enhanced injection can result in the change in the density of excited states, consequently contributing to the magneto-PL in constant voltage mode.

1.1.4 Magneto-photocurrent

In organic semiconductor devices, an external magnetic field can change the electric current generated by photoexcitation, leading to the magneto-photocurrent. Photocurrent generation includes four essential processes: light absorption, formation of excited states, charge carriers' generation from excited states, charge carriers transport. Among these processes, an applied magnetic field can influence charge carrier generation from excited states to generate the magneto-photocurrent. Therefore, MFE on photocurrent can be used as a convenient experimental approach to explore the dissociation, interaction, and recombination process of excited states in organic photovoltaic. [21, 22]

There are two channels, namely exciton dissociation and exciton-charge reaction, to convert photoexcited states into photocurrent in organic semiconductors. The exciton dissociation is driven by intermolecular electrical dipole-dipole interactions, while the exciton-charge reaction occurs mainly through Coulombic scattering between an excited state and a charge carrier resulting in excited states breaking into charge carriers or releasing the trapped charge carriers. Generally, singlet and triplet excited states can have different contributions to the two photocurrent generation

channels due to their different ionic characteristics, binding energies, and lifetimes. Specifically, singlet excitons are first generated due to the spin selection rule under photoexcitation. Singlet excitons can also dissociate into weakly Coulombic bounded singlet polaron pairs. Meanwhile, singlet polaron pairs can be partially converted into triplet polaron pairs through ISC, leading to coexisting of singlet and triplet polaron pairs. For the dissociation channel, the magnetic field can shift the singlet/triplet polaron pairs population ratio by introducing spin precession, consequently changing the photocurrent due to different dissociation rates, leading to magneto-photocurrent. For the exciton-charge reaction channel, the exciton-charge reaction occurs mainly through Coulombic scattering between an excited state and a charge carrier resulting in excited states breaking into charge carriers or releasing the trapped charge carriers. Triplets can dominate the exciton-charge reaction process when experiencing sufficient physical contact with charge carriers due to their relatively long lifetime.

Early studies have been focused on magneto-photocurrent generated within bulk organic semiconductors. It has been revealed that the dissociation channel and exciton-charge reaction channel can contribute to the positive and negative components of magneto-photocurrent, respectively. On the one hand, an applied magnetic field can increase the singlet/triplet ratio through the field-dependent ISC in polaron pair states, yielding a positive component in magneto-photocurrent. On the other hand, the exciton-charge reaction rate can be reduced by an external magnetic field, leading to a negative component in magneto-photocurrent. **Figure 1-2** shows the experimental results of magneto-photocurrent from MEH-PPV, P3HT, and $Ir(ppy)_3$. It can be noted that MEH-PPV with 99% singlet exciton in excited states upon photoexcitation, shows a positive component in magneto-photocurrent from singlet dominated dissociation channel. P3HT with 70% triplet exciton in excited states concurrently shows positive and negative components in magneto-photocurrent, indicating both dissociation and exciton charge reaction can be involved in the generation of magneto-photocurrent. $Ir(ppy)_3$ with 100% triplet exciton in excited states shows negligible magneto-photocurrent because exciton charge reaction rate becomes independent of the external magnetic field due to the strong internal magnetic interaction from SOC.

In the past few years, extensive studies have been focused on organic bulk heterojunction solar cells, in which the magneto-photocurrent is generated from the donor: acceptor interface.[23] In organic bulk heterojunction solar cell, electron-hole pairs can be formed at donor: acceptor interface with spin parallel (triplet) and spin antiparallel (singlet) configuration with ratio 3:1 through random capture. Magnetic field can shift the spin parallel and spin antiparallel electron-hole pairs population ratio by introducing spin precession, consequently changing the photocurrent due to different dissociation rates, leading to magneto-photocurrent. Furthermore, applying an external bias can dissociate the electron-hole pairs formed at the donor: acceptor interfaces, diminishing the magneto-photocurrent signal. Eventually, electron-hole pairs can be completely dissociated when the external bias increases to a critical value, leading to negligible magneto-photocurrent.[24] This critical bias can give an estimate of the electron-hole binding energy. According to this, Hsiao et al, have used magneto-photocurrent to study the optically induced dipole-dipole interaction and its effect on photovoltaic actions in PTB7:$PC_{60}BM$ bulk heterojunction solar cell. By using double beam: 532 nm and 325 nm excitations, to separately excite the donor-PTB7 and acceptor-$PC_{60}BM$ components, excitons, and electrical dipoles can be generated in donor-PTB7 while inducing largely polarized acceptor molecules due to high polarizabilities of acceptor-$PC_{60}BM$. Consequently, a dipole-dipole interaction can occur between the PTB7 and $PC_{60}BM$ components in the bulk-heterojunction system. **Figure 1-3** shows that separately increasing the intensity of one excitation beam with another one at fixed intensity, the critical bias required to completely quench magneto-photocurrent can be reduced. Increasing the electron-hole pairs density at the donor: acceptor interfaces can decrease the critical bias to completely dissociate the electron-hole pairs in the PTB7:$PC_{60}BM$ solar cells when both the donor-PTB7 and acceptor-$PC_{60}BM$ are excited to establish dipole-dipole interaction between donor and acceptor. The experimental study based on double beam excitation based magneto-photocurrent indicates that optically generated dipole-dipole interaction can facilitate the charge dissociation at the donor: acceptor interfaces in the PTB7:$PC_{60}BM$ solar cells. Based on this field-dependent charge generation process, bias-dependent magneto-photocurrent can be used as an in-situ method to analyze the dissociation, recombination, and interaction of excited states under device operation condition in organic solar cells.

1.2. Spin effects in organic-inorganic hybrid perovskites

1.2.1 General properties of hybrid perovskites

In the past few years, organic-inorganic hybrid perovskites have emerged as a new class of semiconductors that exhibiting promising optoelectronic properties and low-cost solution processibility. In particular, the 3D hybrid perovskites, which adopt the chemical structure of ABX_3 (A^+=organic cations such as methylammonium (MA^+) and formamidinium (FA^+), B^{2+}=Pb or Sn, and X^-=I^-, Br^-, and Cl^-, **Figure 1-4a**), has sprung to the forefront of the research in photovoltaics, light-emitting diodes, transistors, and photodetectors in the past few years. More recently, the quasi-2D perovskites have attracted increasing research attention due to the largely enhanced stability and natural multiple-quantum-well structure. The general formula of such quasi-2D layered perovskites is $(RNH_3)A_{n-1}B_nX_{3n+1}$ (n = 1, 2, 3, 4, …) (**Figure 1-4b**), where $(A_{n-1}B_nX_{3n+1})^{2-}$ denotes the conductor layer derived from the 3D perovskite. The conductor layers are isolated from one another through $R–NH_3$, a large aliphatic or aromatic alkylammonium spacer cation, such as phenylethylammonium (PEA) and butylammonium (BA). The thickness, which is decided by the n value in the formula, of each conductor layer can be adjusted by careful control of the stoichiometry in the precursor solutions.

1.2.2 Spin states and spin dynamics of hybrid perovskites

With the strongly coupled orbital motion and spin of the carriers in perovskites, the total angular momentum of the electron and hole ($\boldsymbol{J}_e$ and $\boldsymbol{J}_h$) must be considered to accurately describe the excited states. Consequently, the spin-dependent optical selection rules allow optical orientation and detection of spin-polarized carriers or excitons in perovskites through the circularly polarized light. By utilizing the circularly polarized transient absorption measurements, it was demonstrated that highly polarized carriers can be photogenerated in $MAPbI_3$ perovskite. [25] The polarized carrier populations, as shown by the difference between σ^+ and σ^- probe upon the σ^+ pump excitation, gradually decay within the time scale of picosecond at the room temperature (**Figure 1-5a**). Concomitantly, the equalized populations of carriers ($\sigma^+ + \sigma^-$ probe) eventually undergo carrier recombination on the nanosecond time scale, which is typical for the $MAPbI_3$ perovskite. By cooling the sample down to 77 K, both the initial polarization and spin relaxation lifetime of photocarriers were largely increased due to the inhabited spin relaxation through spin-impurities scattering. The spin relaxation lifetimes were determined to be ~7 ps for electrons and ~1ps for

holes in $MAPbI_3$ at 77 K. Meanwhile, the optical orientation and detection of spin-polarized excitons were also demonstrated in $MAPbI_{3-x}Cl_x$ films through time-resolved Faraday rotation (TRFR).[26] **Figure 1-5b** shows the TRFR decay dynamics of the $MAPbI_{3-x}Cl_x$ films measured in a degenerate pump-probe with the wavelength at the exciton absorption band (1.64 eV for $MAPbI_{3-x}Cl_x$) at 4 K. Therefore, the TRFR primarily measures the spin dynamics of excitons rather than free carriers. In a zero magnetic field, the TRFR signal decays bi-exponentially with two distinct timescales, in which the slow decay component with the lifetime of 1170 ps was attributed to the spin relaxation of excitons. Subsequently, this "puzzling" long-exciton spin lifetime was attributed to the interplay of the Rashba splitting in the exciton bands together with piezoelectric coupling. [27] The unexpectedly long spin lifetimes exceeding 1 ns at 4 K, despite the strong SOC induced by the heavy elements, suggests the great promise for spintronic applications with hybrid perovskites.

1.2.3 Magneto-optical properties of hybrid perovskites

Unlike the organic semiconductors with only light elements, perovskites are previously expected to have negligible MFEs due to short spin relaxation time resulting from the strong SOC. Two decades ago, the magneto-absorption phenomenon was firstly reported in hybrid perovskite ($MAPbI_3$) at a low temperature of 4.2 K and a strong magnetic field (up to 40 T) to investigate the Bohr radius, binding energy, and reduced mass of the exciton [28]. Following the significant progress for perovskite solar cells and light-emitting diodes in recent years, room temperature and low field (< 200 mT) MFEs in photoluminescence, photocurrent, and electroluminescence have been observed in perovskites. In general, the MFEs require the existence of electron-hole pairs in excited states under photoexcitation or electrical excitation. Those electron-hole pairs can form singlets and triplets. It is noted that the dissociation of electron-hole pairs can lead to a generation of the photocurrent, and on the other hand, the radiative recombination of electron-hole pairs gives rise to luminescence. The magnetic field induced change in the populations of singlets and triplets will in turn change the photoluminescence, photocurrent, and electroluminescence when the dissociation and recombination rates for singlets and triplets are not equal to each other.

Despite the restrictions imposed by the strong SOC and thus the short spin relaxation time, significant magneto-photocurrent, magneto-electroluminescence, and magneto-PL responses in excited states have been observed in hybrid perovskite devices and thin films. **Figure 1-6a** shows *J–V* device characteristics of a typical perovskite solar cell (ITO/PEDOT:PSS/$MAPbI_{3-x}Cl_x$/PCBM/Al) under two photoexcitation conditions above and below the bandgap at 400 and 785 nm, respectively. When illuminated with the above bandgap excitation (400 nm), a broad magneto-photocurrent with a magnitude of ~ 0.45 % can be observed (**Figure 1-6b**), which is in the form of a Lorentzian with half-width at half maximum (HWHM), $B_{1/2}$ value ~ 325 mT. No obvious magneto-photocurrent response was obtained with the below bandgap excitation (785 nm). The observed MFEs were attributed to the largely different *g* factors of the electron and hole in their spin 1/2 pair species in hybrid perovskites [29]. Even though the spin relaxation time is shorter compared with typical organic semiconductors, the much larger Δg is possible to cause a larger spin precession frequency difference between electron and hole in their pair state, as shown in the diagram in **Figure 1-6c**. The Δg value of ~ 0.65 has been claimed in $MAPbI_3$, which is orders of magnitude higher than that of other semiconductors. Therefore, the intersystem crossing between singlets and triplets can occur many times to reach a new equilibrium during the spin-pair lifetime. Consequently, the change of populations in singlets and triplets leads to the change in photoluminescence, photocurrent, and electroluminescence with the applied magnetic field.

Furthermore, positive magneto-photocurrent and negative magneto-PL were observed in hybrid perovskites at room temperature and low field when the photoexcitation intensities exceed the threshold values (**Figure 1-7**) [30]. This experimental observation further indicates that the observed MFEs in hybrid perovskite occurred at electron-hole pair states. Singlets and triplets exhibit opposite contributions to generate PL and photocurrent (Jsc) through the preferred radiative recombination and dissociation, respectively. More importantly, it was found that the Magneto-PL and magneto-photocurrent signals are strongly dependent on the photoexcitation intensity. Only when the excitation intensity reaches a certain threshold value, does the magneto-PL become significant to be observed. Later on, the dependence of the observed MFEs on the intensity of photoexcitation is explained in terms of the screening effect of the Coulomb interaction by the free

electron-hole pairs based on the effective-mass model simulation [31]. As the intensity of photoexcitation increases, the exchange is greatly reduced. Meanwhile, the magneto-PL becomes significant.

In summary, both photocurrent and photoluminescence are spin-dependent processes in hybrid perovskites. Therefore, manipulating spins can provide a new approach to control photovoltaic and light-emitting properties in perovskites. The successful observation of MFEs in perovskites indicates that: (1) low field magnetic field less than 1 T can change the populations of singlets and triplets in excited states; (2) the recombination and dissociation rate for singlets and triplets are different; (3) the electron-hole pairs may process longer spin lifetime than single carriers in perovskites.

Appendix

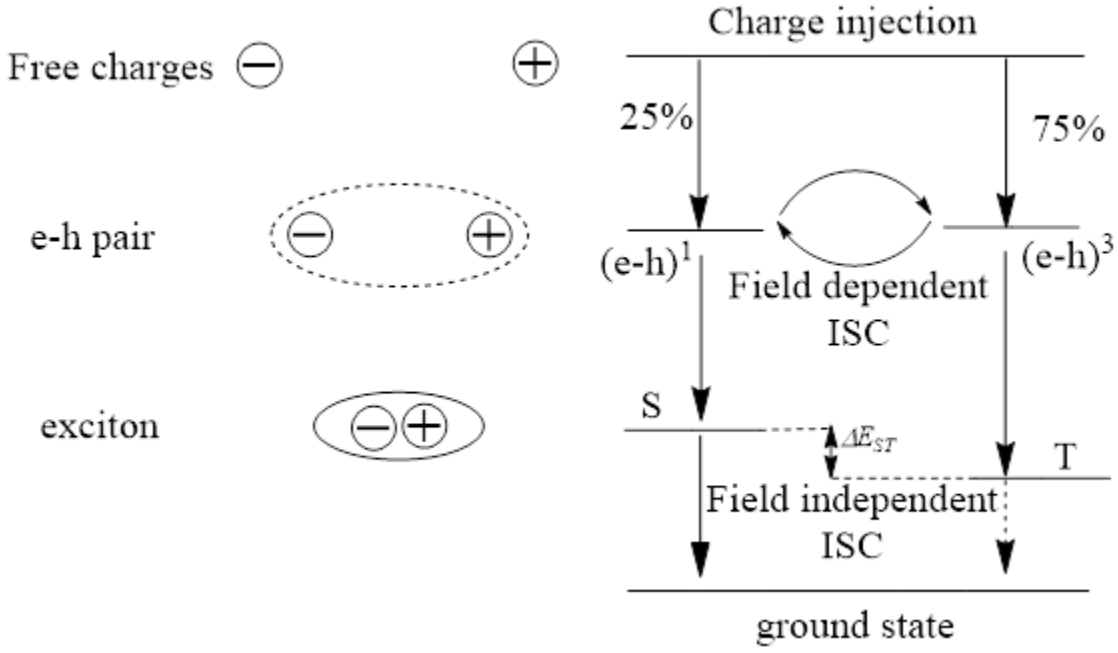

Figure 1-1 Schematic energy level diagram for free charges, electron-hole pairs and excitons in OLEDs.

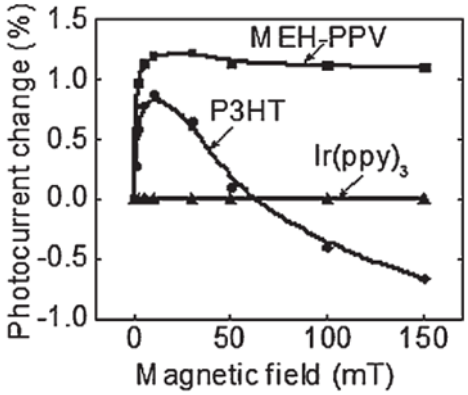

Figure 1-2 Magneto-photocurrent from MEH-PPV, P3HT, and $Ir(ppy)_3$ based devices. Data adapted from Ref. [1]

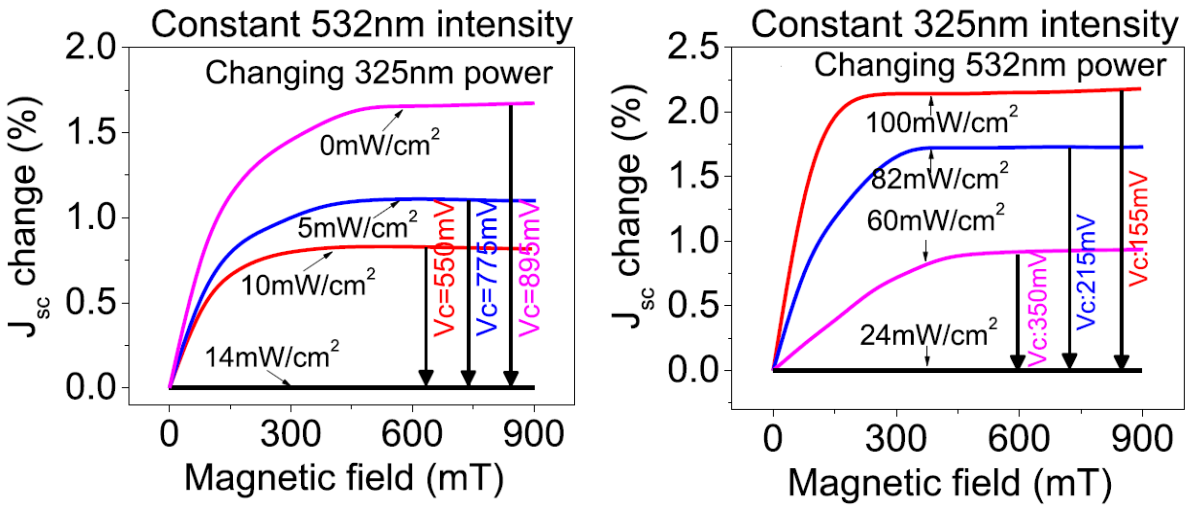

Figure 1-3 Magneto-photocurrent measured by separately exciting donor-PTB7 and acceptor-$PC_{60}BM$. (a) Changing 325nm intensity of exciting acceptor-PC60BM at constant 532 nm intensity (24mW/cm^2) of exciting donor-PTB7. (b) Changing 532nm intensity of exciting donor-PTB7 at constant 325nm intensity (14mW/cm^2) of exciting acceptor-$PC_{60}BM$. Data adapted from Ref. [24]

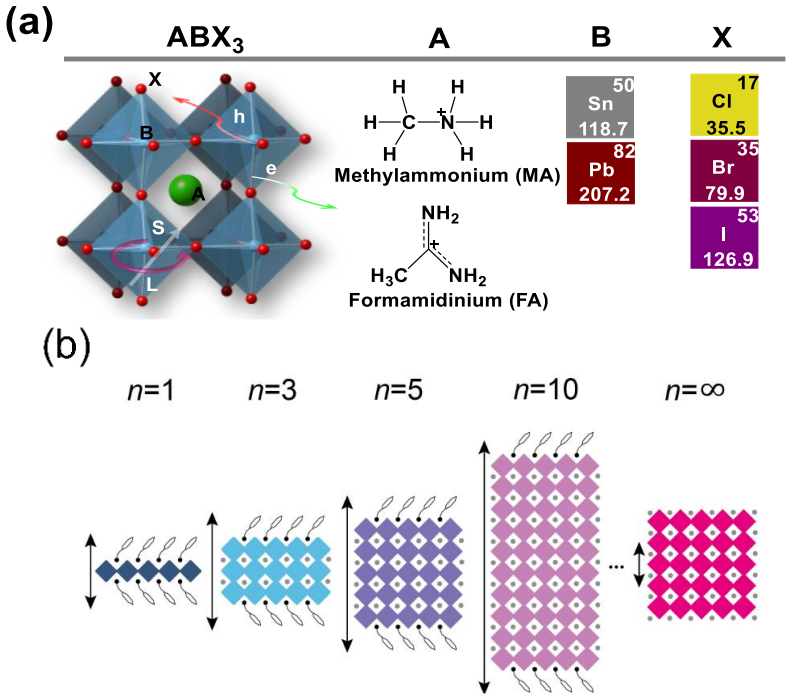

Figure 1-4 Schematic diagram to show the structure of (a) 3D & (b) quasi-2D hybrid perovskites.

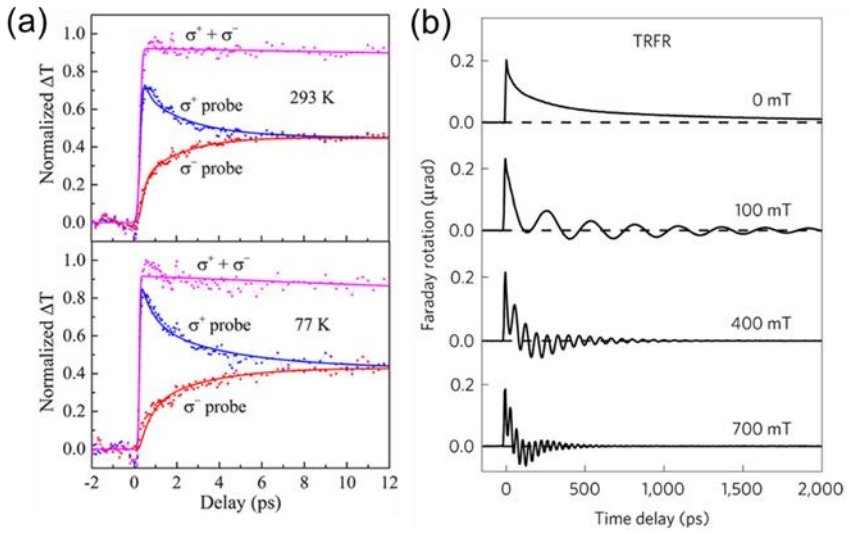

Figure 1-5 (a) Normalized circularly polarized transient absorption decay dynamics at room temperature 293 K (top) and low temperature 77 K (bottom); (b) Decay dynamics of the time-resolved Faraday rotation at low temperature 4 K. The Faraday rotation signal decays bi-exponentially at zero field, in which the slow decay reflects the spin dynamics of excitons with a lifetime of 1170 ps. Data adapted from Ref. [25, 26]

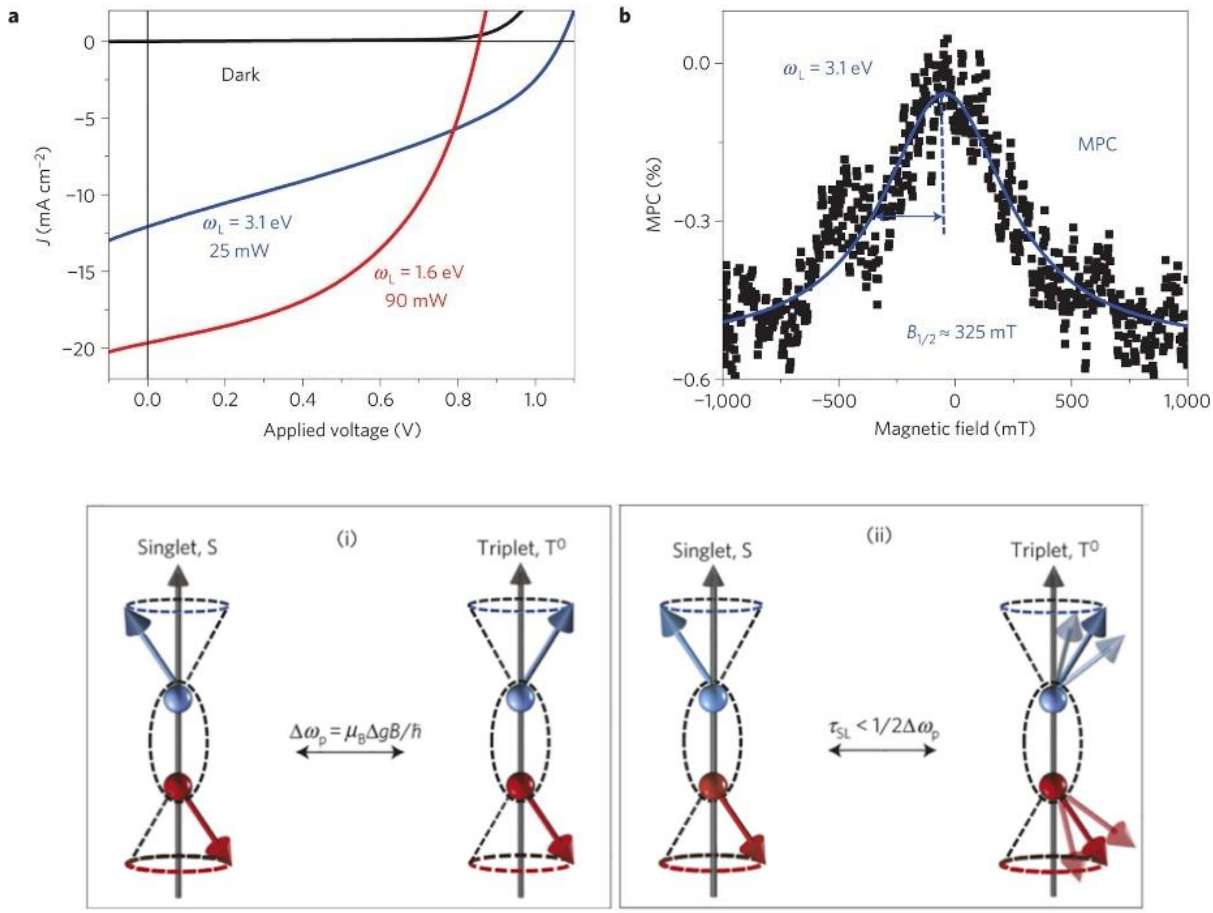

Figure 1-6 (a) *J–V* device characteristics in the dark (black line) and at two laser excitation wavelengths (blue and red lines) as denoted. (b) magneto-photocurrent (MFC) response up to 1 T with the photoexcitation above bandgap at 3.1 eV. The blue line through the data points is a Lorentzian function fit with HWHM ($B_{1/2}$) as indicated. (c) Diagram of the Δg spin-mixing mechanism within an electron-hole spin-pair that shows the intersystem crossing between the singlet and triplet configurations due to different electron and hole precession frequencies around the applied field, B in the z-direction. Panels (i) and (ii) show the situation when the spin relaxation rate is much smaller (larger) than the intersystem crossing rate that gives substantive (diminishing) MFE. In panel (ii) the electron-hole pairs lose coherence on spin precession and consequently, MFE diminishes. Data adapted from Ref. [29]

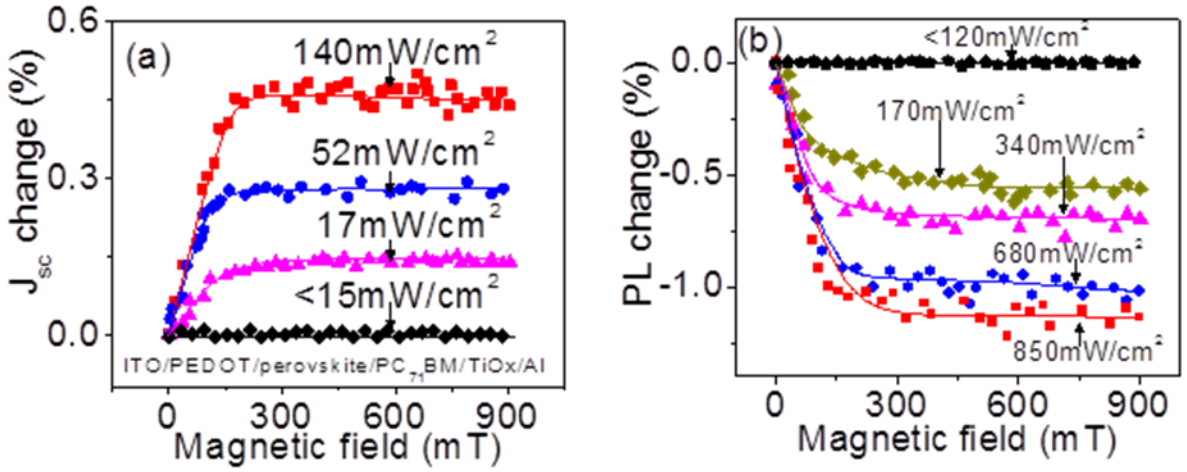

Figure 1-7 (a) Magneto-photocurrent in the ITO/PEDOT:PSS/$CH_3NH_3PbI_{3-x}Cl_x$/$PC_{71}BM$ /TiOx/Al solar cell and (b) magneto-PL in perovskite thin film. The photoexcitation source is from 532nm CW laser. Data adapted from Ref. [32]

Chapter 2 Magneto-optical effects in organic optoelectronic devices

2.1 Abstract

This chapter explores the spin-dependent optoelectronic process in organic light-emitting and photovoltaic devices through magneto-optical effects, including magneto-PL, magneto-EL, and magneto-photocurrent. In chapter 2.4.1, we use magneto-PL and magneto-EL to identify the new excited states, namely, spatially extended states that existed in F8BT microcavity OLEDs, responsible for the emission spectral narrowing phenomenon. This part is revised based on the published article [M. Wang, J. Lin, Y.-C. Hsiao, X. Liu, B. Hu, Nat. Commun. 2019, 10, 1614]. [33] In chapter 2.4.2, we use the bias-dependent magneto-photocurrent measurements to directly monitor the electron-hole pairs dissociation process in ClAlPc single active layer device with the record high photovoltaic efficiency among all the single-layer devices. We have found that the ClAlPc molecules exhibit extremely low electron-hole binding energy due to the symmetrically arranged planar withdrawing-donating (pyrrole-phenylene) structures. This part is revised based on the published article [M. Wang, Y.-Z. Li, H.-C. Chen, C.-W. Liu, Y.-S. Chen, Y.-C. Lo, C.-S. Tsao, Y.-C. Huang, S.-W. Liu, K.-T. Wong, B. Hu, Mater. Horiz. 2020, 7, 1171.]. [34] Clearly, magneto-optical effects provide critical information to understand the excited state behaviors in organic optoelectronic devices.

2.2 Introduction

2.2.1 Organic microcavity light-emitting diodes

Organic semiconductors are known as low-dielectric materials where Frenkel excitons can be formed with high binding energies up to 1 eV.[35, 36] Frenkel excitons are more likely to have radiative recombination through spontaneous emission with large spectral tuning properties. Organic semiconductors have successfully developed unique electroluminescence (EL) actions from thin-film organic light-emitting diodes (OLEDs) based on spontaneous emission mechanism.[37] However, developing lasing actions from thin-film OLEDs has been a long-term challenging endeavor.[38, 39] In contrast, optical pumping has led to significant lasing actions in organic semiconductors by using different optical feedback mechanisms based on microcavities and grating designs to realize cooperative Frenkel excitons with significant photoluminescence

(PL) spectral narrowing phenomenon as increasing pumping density.[40] However, with the success of optically pumped lasing actions, it is still a challenging issue on whether an optical stimulation is sufficient to generate a cooperative interaction between electrically generated light-emitting states under electrical injection. Using high quality factor (high-Q) microcavity OLEDs has led to a significant EL spectral narrowing phenomenon based on light-emitting molecules of Alq_3:DCJTI under electrical pumping. The narrowed EL spectrum with the full width at half maximum (FWHM) of 1.95 nm was successfully observed as the injection current was increased to 1000 mA cm^{-2}. However, it has been a fundamental question on whether this EL spectral narrowing phenomenon is an indication that the electrically generated excited states become coherent within the microcavity or just a normal microcavity effect. The normal optical microcavity effect originates from the weak coupling interaction between light-emitting molecules and the confined electromagnetic field introduced by the microcavity that can increase the spontaneous emission rate in a resonant radiation mode while suppressing the non-resonant spontaneous emission. On the other hand, the microcavity can fundamentally change the characteristics of the excited states through optical resonance, generating an EL spectral narrowing phenomenon and providing the necessary condition towards developing electrically pumped lasing actions.

In chapter 2.4.1, magneto-PL and magneto-EL were used to address whether the microcavity can influence the characteristics of excited states in the F8BT microcavity OLEDs with emission spectral narrowing phenomenon. We should note that magneto-PL and magneto-EL can be widely observed when the spatially extended excited states such as polaron pairs, electron-hole pairs, and charge-transfer states are formed with antiparallel and parallel spins in organic light-emitting materials. In contrast, when spatially extended states are absent, Frenkel excitons, functioning as primary excited states with a strong exchange interaction due to short electron-hole separation distance, do not allow spin mixing between singlets and triplets. In this case, an external magnetic field is not able to change the populations on singlet and triplet Frenkel excitons, leading to negligible magneto-PL and magneto-EL. Here, we select the F8BT thin film with the thickness of 65 nm, which does not show any detectable magneto-PL and magneto-EL without the microcavity, to separately fabricate cavity-based and cavity-free OLEDs. In particular, the microcavities were

fabricated with high-Q, intermediate-Q, and low-Q structures. We found that an optical excitation leads to a clear magneto-PL signal in the cavity-based OLED as contrarily compared to the non-detectable magneto-PL in cavity-free OLED under photoexcitation. This observation indicates that the microcavity induces the formation of spatially extended excited states, in addition to the light-emitting Frenkel excitons, in the F8BT layer under photoexcitation. Furthermore, a similar phenomenon was also observed under electrical injection: the microcavity-based OLED shows an appreciable magneto-EL, indicating the formation of spatially extended excited states, while the cavity-free OLED does not exhibit any detectable magneto-EL. This study indicates that the optical microcavity can indeed influence the characteristics of excited states to generate spatially extended states functioning as intermediate states, leading to the EL spectral narrowing phenomenon under optical and electrical excitations.

2.2.2 Organic single active layer solar cells

In spite of the advantage for efficiently catching photons, organic materials typically possess high electron-hole (exciton) binding energies due to low dielectric constants.[35, 41] As consequence, for most organic solar cells and photodetectors with high photogeneration yield, the photo-responsive layer is either donor/acceptor bilayer-type or a donor: acceptor blend (namely, a bulk heterojunction structure) not only for facilitating the charge carrier generation by virtue of photo-induced charge separation, but also for effective charge transport and collection. Therefore, both the molecular design and device fabrication are crucial for manipulating the intermixed donor: acceptor morphologies. One feasible way for reducing the complexity of making efficient organic optoelectronic devices is to use “single component” as the active layer. In this regard, there are still limited cases being reported to perform promising efficiency due to the inferior photogeneration yield of photo-active materials. Recently, the direct generation of free carriers by photoexcitation has been observed in some phthalocyanine-type molecules such as zinc phthalocyanine (ZnPc), boron subphthalocyanine chloride (SubPc), and boron subnaphthalocyanine chloride (SubNc) through spectroscopic measurements.[42-44] The observed direct generation of free carriers in single-component active layers under photoexcitation presents an interesting evidence that these organic molecules possess extremely low electron-hole binding energies even with low-dielectric constants. Fundamentally, this imposes a critical

question on the underlying mechanisms that are accountable for the significantly low electron-hole binding energies in these organic materials. Technically, these results trigger a new possibility for exploring phthalocyanine-based materials as a "single-component" active layer to realize efficient OPDs without using BHJ designs.

In chapter 2.4.2, we monitor the dissociation of electron-hole pairs through bias-dependent magneto-photocurrent measurements to explore the binding energies in two analogous organic macrocyclic molecules with symmetric and asymmetric planar electron withdrawing-donating structures, namely ClAlPc and ClAlNPc, respectively. In this experimental method, increasing external bias can gradually decrease the amplitude of magneto-photocurrent. Here, the critical bias required to completely quench the magneto-photocurrent signal can be used to estimate the electron-hole binding energies. The magneto-photocurrent measurements conducted on ClAlPc and ClAlNPc molecules based on single-layer device configured as ITO/ClAlPc/Al reveal that the electron-hole pairs in ClAlPc molecule with symmetrically arranged planar withdrawing-donating (pyrrole-phenylene) structures can be completely dissociated at the bias of 24.8 mV, presenting an extremely low binding energy. In contrast, the ClAlNPc molecule with asymmetrical planar withdrawing-donating structures show a much higher binding energy where the electron-hole pairs are completely dissociated at the bias of 525 mV. The low exciton biding energy of ClAlPc molecule is highly beneficial for developing efficient single-layer optoelectronic devices.

2.3 Experimental Methods

2.3.1 Magneto-PL and magneto-EL

The amplitude for magneto-PL and magneto-EL signal is defined by the relative change in percentage: $MFE = \frac{I_B - I_0}{I_0}$, where I_B and I_0 are the signal intensities with and without an external magnetic field. The magneto-EL and magneto-PL measurements were performed by using Horiba Fluorolog 3 spectrometer combined with an electrically controllable magnet. Specifically, the magneto-PL and magneto-PL were measured by recording the emission intensity at the spectral peak wavelength as a function of magnetic field. The electrical excitation source was provided by Keithley-2400. The photoexcitation was provided by a 405 nm continuous wave (CW) laser. The

EL and PL spectra were measured by Horiba Fluorolog 3 spectrometer. All the experimental measurements were carried out with encapsulated devices at room temperature.

2.3.2 Magneto-photocurrent

The bias-dependent magneto-photocurrent signals were measured by monitoring the photocurrent value (Keithley 2400) as a function of magnetic field at room temperature. The magneto-photocurrent amplitude is defined as: $MFE = \frac{I_B - I_0}{I_0}$, where I_B and I_0 are the photocurrents with and without an external magnetic field. The photoexcitation was from 785 nm CW laser.

2.3.3 Impedance measurements

The impedance measurements were carried out by using Agilent E4980A LCR meter under an alternating bias of 50 mV.

2.4 Results and Discussion

2.4.1Magneto-optical studies on spatially-extended excited states in microcavity organic light-emitting diodes

Figure 2-1 a and **b** show the device structure and energy diagram for the cavity-based OLEDs using the F8BT as the light-emitting medium. The absorption and PL spectra of F8BT thin film are shown in **Figure 2-1c**. The chemical structure of F8BT is shown in the inset of **Figure 2-1c**. Essentially, the microcavity is designed based on the distributed Bragg reflector (DBR) structure: the top mirror consists of Al, ZnS, and MgF_2 layers, and the bottom mirror combines TiO_2 and SiO_2 layers. Within the bottom mirror the TiO_2/SiO_2 layers were prepared with 15, 3, and 2 repeating pairs to give different bottom DBR reflectance of 99 %, 81 %, and 44 % at 550 nm, leading to high-Q, intermediate-Q, and low-Q microcavities, as shown in **Figure 2-1d**. The Q-factor of the microcavity structures is varied from 94 (high-Q) to 40 (intermediate-Q) and 13 (low-Q). It can be seen in **Figure 2-2a** that using the microcavity can lead to a significantly narrowed PL spectrum under the photoexcitation (1000 mW cm^{-2}) of continuous-wave (CW) 405 nm laser beam. The FWHM of PL spectra are determined to be 6 nm, 16 nm and 45 nm in high-Q, intermediate-Q and low-Q microcavities. Clearly, by increasing the Q factor the PL spectrum becomes gradually narrowed in the microcavity. It is known that an optical excitation generates Frenkel excitons due to low dielectric constants and give rise to broad PL spectra in organic light-

emitting materials with inhomogeneous morphologies. Here, it remains as a fundamental question on how the narrowed PL is generated by the Frenkel excitons in the microcavity. Essentially, addressing this question requires an understanding on the effects of microcavity on light-emitting states in the cavity-based F8BT OLEDs.

To explore the effects of microcavity on light-emitting states, magneto-PL studies were performed by optically exciting the cavity-based F8BT OLEDs with high, intermediate, and low Q values. We should note that broad PL from Frenkel excitons have a negligible response to an external magnetic field due to strong exchange interaction preserving spin states, lacking magneto-PL under 1 T at room temperature. When the microcavity is not used, the cavity-free OLED shows a non-detectable magneto-PL, which is a normal phenomenon observed on Frenkel excitons in organic light-emitting materials. Here, we observed a surprising phenomenon by using the microcavity: the narrowed PL shows a magnetic field dependence at low field (< 200 mT) and room temperature, leading to a magneto-PL signal (**Figure 2-2b**). Specifically, the PL intensity gradually increases and then becomes saturated with increasing magnetic field, generating a magneto-PL signal at room temperature in cavity-based F8BT OLEDs under photoexcitation. Decreasing the Q factor can directly decrease the magneto-PL signal, simultaneously accompanied with spectral broadening phenomenon. The high-Q and intermediate-Q cavities give the magneto-PL with the amplitudes of 2.0 % and 0.8 %, respectively. The magneto-PL becomes negligible when further decreasing the Q factor. We should point out that the observed magneto-PL generated in the high-Q microcavity is very similar to that generated by light-emitting charge-transfer states, the spatially extended excited states, formed in donor: acceptor composite. Here, the observed magneto-PL clearly indicates that the microcavity can indeed introduce spatially extended excited states, the polaron pairs-like states, in the light-emitting F8BT. Because the spin mixing can easily occur in spatially extended excited states due to weak exchange interaction, an external magnetic field can change the populations on the singlet and triplet spatially extended states through spin mixing, leading to a magneto-PL when the spatially extended states relax to light-emitting Frenkel excitons.

We further discuss whether the observed magneto-PL represents spatially extended excited states by removing the contribution from triplet-triplet annihilation (TTA). It should be mentioned that TTA can occur within Frenkel excitons when two triplet excitons mutually interact within close proximity. The TTA is a bimolecular process which requires a high density of triplet excitons. In general, the TTA is a very limited component in steady-state PL in both organic fluorescent and phosphorescent materials under photoexcitation. As a consequence, both fluorescent and phosphorescent materials do not demonstrate any detectable magneto-PL in steady state at room temperature. In time-dependent measurement where the TTA is selectively monitored, it was found that the TTA gives a negative sign on the magneto-PL/EL signals based on the assumption that a magnetic field decreases the TTA rate constant by perturbing spin interaction.[45, 46] Here, our magneto-PL with positive sign observed in cavity-based F8BT OLEDs does not suggest the TTA occurring in F8BT within the microcavity. Nevertheless, it is very clear that without microcavity, no magneto-PL can be detected in the F8BT, similar phenomenon commonly observed in organic materials under photoexcitation, indicating that the Frenkel excitons are primary light-emitting states in the pristine F8BT. However, with microcavity, our magneto-PL indicates that spatially extended excited states are indeed formed with the characteristics similar to polaron pairs, functioning as intermediate states within cavity-based F8BT OLEDs. This creates an interesting question on how the spatially extended states are induced by the microcavity. Here, we consider the following possibility to understand the effects of microcavity on light-emitting states based on magneto-PL with spectral narrowing phenomenon. When the optical confinement is introduced to form an optical field in the microcavity, the Frenkel excitons placed in an optical field develop into resonant states, leading to spatially extended states with the characteristics similar to polaron pairs. This means that the optical field can extend the wavefunctions of Frenkel excitons in cooperative manner, forming resonant spatially extended states in the microcavity. The resonant spatially extended states with cooperative manor can essentially form coherent light-emitting Frenkel excitons through recombination, generating a narrowed PL. Although this possibility demands further investigation, it is clear that the microcavity introduces the additional excited states with the characteristics similar to polaron pairs, accompanied with spectral narrowing phenomenon, in the cavity-based F8BT OLEDs under photoexcitation, according to the observed magneto-PL.

Now we confirm the characteristics of spatially extended states within the cavity-based F8BT OLED under electrical injection by using magneto-EL measurement at constant-current mode. We know that polaron pairs can be largely formed towards light-emitting excitons in OLEDs under electrical injection. It has been experimentally observed that an external magnetic field can conveniently change the populations on the singlet and triplet polaron pairs, leading to magneto-EL and magneto-current due to largely different recombination rates associated with singlets and triplets. Therefore, magneto-EL can be measured at two different conditions: constant-current and constant-voltage modes, while monitoring the EL intensity with scanning magnetic field. At the constant-current mode, the EL intensity is changed purely by the populations on polaron-pair states through spin mixing caused by magnetic field, leading to spin mixing-based magneto-EL, namely magneto-$EL_{(mixing)}$. At constant-voltage mode, the EL intensity is changed by both magneto-current and the populations through spin mixing under the influence of magnetic field, generating the combination of spin mixing-based magneto-$EL_{(mixing)}$ and current-based magneto-$EL_{(current)}$. Here, we use magneto-EL at constant-current mode to confirm that the spatially extended states are formed in the microcavity under electrical injection based on whether the spin mixing is occurred. By carefully selecting the thickness (65 nm) of active F8BT layer, the cavity-free OLEDs with the same device structure, do not show any detectable magneto-EL signal with a broad spectral width (FWHM = 87 nm). The absence of magneto-EL implies that, at this layer thickness, the injected electrons and holes do not have an opportunity to form the spatially extended states and directly recombine into Frenkel excitons. As expected, the electrically generated Frenkel excitons do not demonstrate a magneto-EL signal due to the negligible spin mixing caused by strong exchange interaction. Interestingly, when the microcavity is used with this selected thickness of active layer, a magneto-EL signal can be clearly observed with a narrow EL spectrum (FWHM = 6 nm), as shown in **Figure 2-2 c** and **d**. Furthermore, we can see that increasing the Q factor in the microcavity can appreciably increase the magneto-EL amplitude from 1.7 % to 2.1 % and 5.1 % with the FWHM changed from 43 nm to 14 nm and 6 nm. This magneto-EL confirms that the microcavity can indeed introduce spatially extended states with the characteristics similar to polaron pairs with spectrally narrowed EL under electrical injection.

2.4.2 Magneto-photocurrent studies on efficient single-layer organic photovoltaic device with low binding energy

Figure 2-3a shows the molecular structure of the ClAlPc and ClAlNPc. **Figure 2-3b** shows the photovoltaic characteristics based on the single-layer devices (ITO/active layer/Al) using the low-binding-energy ClAlPc and the counterpart ClAlNPc as the active layer with two different film thicknesses of 50 nm and 100 nm. The single-layer device with 50 nm ClAlPc shows an excellent power conversion efficiency (PCE) of 0.45% with the open-circuit voltage (Voc), short circuit-current (Jsc), and fill factor (FF) of 0.76 V, 1.3 mA/cm^2 and 45.42 %, respectively. Furthermore, the 100 nm ClAlPc single-layer device still shows a similar photovoltaic performance with the PCE of 0.42%. This thickness-independent photovoltaic performance can be attributed to the extremely low electron-hole binding energy due to symmetric macrocyclic planar structure and sufficient transport channel supported by the vertical electric dipole (Cl^--Al^+). In contrast, both 50 nm and 100 nm ClAlN1Pc single-layer devices show very low photovoltaic characteristics with film thickness dependence due to high electron-hole binding energy. The photovoltaic parameters for ClAlPc and ClAlNPc devices are summarized in **Table 2-1**. **Figure 2-3c** shows the external quantum efficiency (EQE) spectra of the ClAlPc and ClAlNPc single-layer devices. As shown in **Figure 2-3d**, the single-layer ClAlPc and ClAlNPc devices have similar photoactive regime between 350 nm and 700 nm but demonstrate a large difference in PCE by a factor of 15.

Clearly, the high photovoltaic performance in ClAlPc-based single-component active layer device indicates the photogenerated electron-hole pairs can be efficiently dissociated into free charge carriers even without using any bulk-heterojunction design. Here, we notice that the ClAlPc molecule is consisted of four planar isoindole rings symmetrically arranged into a planar cyclic structure with one vertical electric dipole ($Cl^{\delta-}$-$Al^{\delta+}$). By arranging four isoindole units with four-fold symmetry in a molecular ring, upon photoexcitation, the intramolecular charge transfer can lead to symmetrically arranged photo-induced electrical dipoles (phenylene$^{\delta+}$-pyrrole$^{\delta-}$) within a molecular ring. Due to the molecular symmetry, these four electrical dipoles (phenylene$^{\delta+}$-pyrrole$^{\delta-}$) encounter symmetrical head-to-head repulsive interactions, consequently decreasing the Coulomb attraction within each electrical dipole. Essentially, this can significantly lower the electron-hole binding energy of ClAlPc. This presents a fundamental principle that introducing the symmetry of

photoinduced charge density leads to a large reduction on electron-hole binding energy in low-dielectric organic molecules. Here, we directly monitor the dissociation of electron-hole pairs in ClAlPc by using bias-dependent magneto-photocurrent. Generally, the presence of magneto-photocurrent in organic semiconductors indicates that the electron-hole pairs are formed with singlet and triplet states under photoexcitation for the generation of photocurrent.[22] A magnetic field can change the populations on singlet and triplet electron-hole pairs by perturbing intersystem crossing, leading to the change on photocurrent, generating a magneto-photocurrent, due to the different dissociation rates associated with singlets and triplets. On the other hand, applying an external bias can increase the dissociation of electron-hole pairs, decreasing magneto-photocurrent signal. When an external bias reaches a critical value, magneto-photocurrent signal can be completely quenched. Essentially, this critical bias, required to completely quench magneto-photocurrent signal, reflects the electron-hole binding energy. Therefore, combining magneto-photocurrent with external bias provides the convenient experimental tool to *in situ* monitor the dissociation of electron-hole pairs in organic materials when an external bias is applied.[24] **Figure 2-4a** shows the bias-dependent magneto-photocurrent signal in ClAlPc single-layer device with the structure of ITO/ClAlPc(50 nm)/Al. We can see that the photocurrent gradually increases and then becomes saturated with increasing magnetic field, leading to a magneto-photocurrent signal. More importantly, the magnitude of magneto-photocurrent signal is gradually decreased with increasing bias. This indicates that magneto-photocurrent can indeed reflect the dissociation of electron-hole pairs generated in the ClAlPc film with gradually increasing bias imposed on the ITO/ClAlPc/Al device. By plotting magneto-photocurrent amplitude against bias (**Figure 2-4b**), we can determine that the electron-hole pairs are completely dissociated at the low bias of 24.8 mV, indicating the extremely small binding energy of electron-hole pairs, responsible for the efficient free charge carrier generation in ClAlPc molecule. This experimental result brings about a critical question on why free photogenerated carriers can be directly generated in organic materials which normally possess high electron-hole binding energies due to low-dielectric constants.

To verify the symmetry-dependent electron-hole binding energies, we employed the same protocol on an asymmetric planar macrocyclic molecule ClAlNPc having a structure fused with three

pyrrole-phenylene (isoindole) moieties and one pyrrole-naphthylene structure (benzoisoindole). By breaking the symmetry of charge density, the dissociation of electron-hole pairs can become much more difficult, shown as a much higher bias to quench the magneto-photocurrent as indicated by **Figure 2-4c**. Thus, completely quenching the magneto-photocurrent requires the bias as high as 525 mV in the device with ClAlNPc thin film, where the symmetry of charge density is removed, as shown in **Figure 2-4d**. This result indicates that perturbing the symmetry of charge density in a planar macrocyclic system causes a large increase on electron-hole binding energy. Clearly, increasing the symmetry of charge density presents an important mechanism to lower the electron-hole binding energy in organic macrocyclic molecules. Especially, the extremely low binding-energy in four-fold symmetric ClAlPc molecule significantly facilitates the photogeneration of free carriers in a photodetector with the single-component active layer for realizing the extraordinary optoelectronic capability.

Now we discuss the underlying mechanism responsible for the extremely low electron-hole binding energy. The ClAlPc molecule consists of four symmetrically arranged isoindole rings linked by four nitrogen bridges into a fully conjugated symmetric planar molecular ring with a vertical electric dipole ($Cl^{\delta-}$-$Al^{\delta+}$). We should note that photoinduced charge transfer occurring at the isoindole moiety from the outer phenylene to inner pyrrole leads to optically generated electric dipoles (phenylene$^{\delta+}$-pyrrole$^{\delta-}$). With the four-fold symmetry of charge density, the four optically generated electric dipoles are symmetrically arranged with head-to-head configuration. Essentially, these symmetrically arranged optically generated electric dipoles with head-to-head configuration can decrease the attractive interaction between phenylene$^{\delta+}$ and pyrrole$^{\delta-}$ within each dipole, serving as the requirement to significantly lower the binding energy of photogenerated electron-hole pairs towards direct generation of photogenerated carriers. We should point out that this vertical dipole ($Cl^{\delta-}$-$Al^{\delta+}$) can significantly stabilize the formation of optically generated dipoles (phenylene$^{\delta+}$-pyrrole$^{\delta-}$) with four-fold symmetry in ClAlPc molecules. Without this vertical dipole, optically excited electrons in the inner ring have the possibilities to quickly relax back to the outer ring. To verify the formation of optically generated electrical dipoles through photoinduced charge transfer, the capacitance-frequency characteristics were examined for the ClAlPc at different photoexcitation intensities (**Figure 2-5a**). We can see that the photoexcitation clearly increases the

signal amplitude around 1 kHz on capacitance-frequency (C-f) characteristics in the ClAlPc molecule while the ClAlNPc molecule shows a negligible change upon applying photoexcitation (**Figure 2-5b**). The photoexcitation-dependent C-f characteristics provide an evidence to support that the electron withdrawing (pyrrole) and donating (phenylene) units respectively become negatively and positively charged within the ClAlPc molecule as the consequence of exciton dissociation due to extremely low electron-hole binding energy. As comparison, the ClAlNPc molecule with asymmetric planar molecular cyclic structure does not demonstrate appreciable photoexcitation-dependent C-f characteristics, confirming the absence of dissociated charge carriers due to the high electron-hole binding energy.

2.5 Conclusion

In this chapter, magneto-optical methods were applied to investigate the excited state behaviors in microcavity OLEDs and single active layer solar cells. Firstly, it is found that the microcavity generates the magneto-PL signal in F8BT OLED under photoexcitation, which is completely absent when microcavity is not used. This provides an evidence that microcavity leads to the formation of spatially extended states, functioning as the intermediate states prior to the formation of Frenkel excitons in organic materials. The spatially extended states in microcavity OLEDs are confirmed by the magneto-EL solely observed from the cavity-based F8BT OLED under electrical injection. Clearly, the spatially extended states present the necessary condition to realize spectral narrowing phenomenon towards developing lasing actions in cavity-based OLEDs.

Secondly, our bias-dependent magneto-photocurrent studies found that introducing the symmetry of charge density with planar molecular ring provides a fundamental mechanism to significantly lower the electron-hole binding energy in organic molecules for photovoltaic applications. The critical bias required to complete the dissociation of photogenerated electron-hole pairs reaches an extremely low value of 24.8 mV in four-fold symmetry ClAlPc molecules. This reflects a significantly reduced electron-hole binding energy when introducing the four-fold symmetry of charge density through molecular design of planar macrocyclic conjugated ring systems. With the extremely low binding energy in ClAlPc to effectively dissociate photogenerated electron-hole pairs towards direct generation of free carriers under photoexcitation, we have demonstrated

record-high photovoltaic efficiency (0.45 %) in ClAlPc-based single active layer photovoltaic device (ITO/ClAlPc 50nm/Al). Furthermore, by breaking the symmetry of charge density, the critical bias required to dissociate the electron-hole pairs is largely increased to 525 mV in the analogous counterpart ClAlNPc with asymmetric molecular ring composing of three planar isoindole rings and one benzoisoindole ring. Clearly, our bias-dependent magneto-photocurrent studies indicate that increasing the symmetry of charge density presents an underlying mechanism to significantly lower the electron-hole binding energies in organic molecules for energy related optoelectronic applications.

Appendix

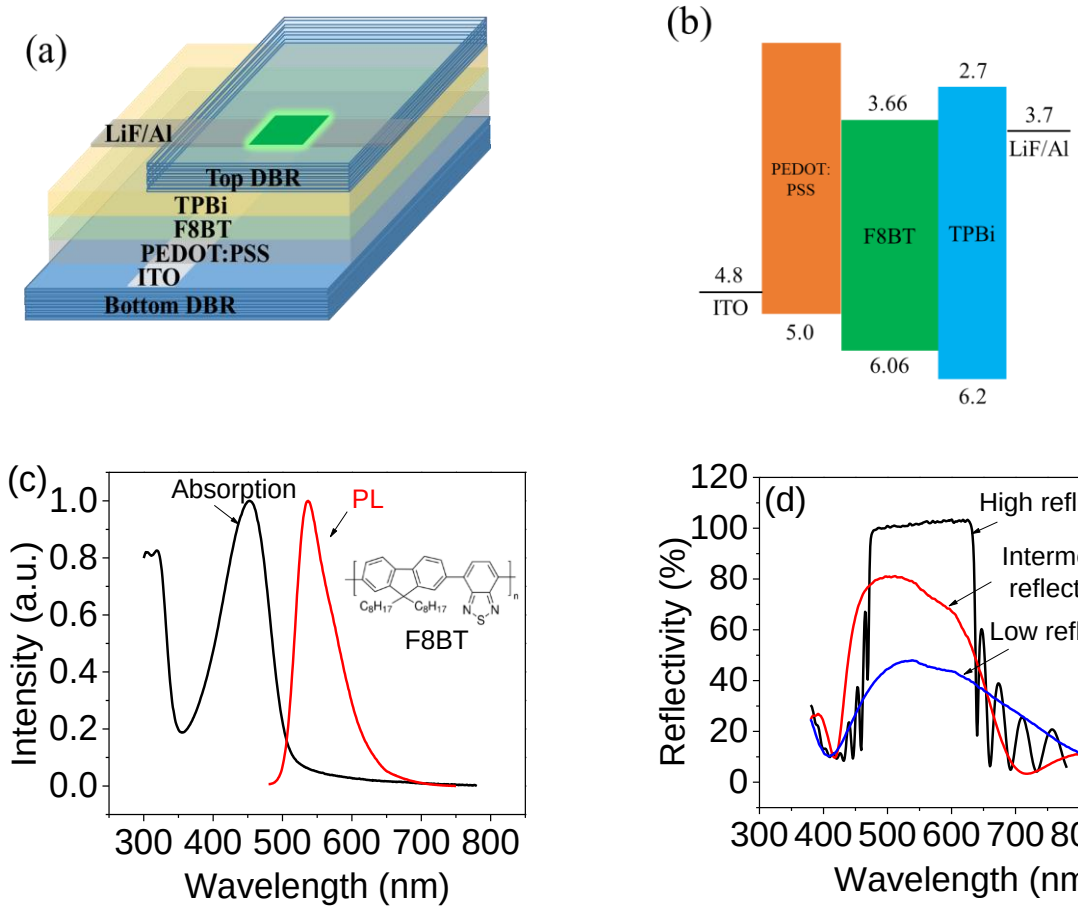

Figure 2-1 Structure and optical characterizations of cavity-based F8BT organic light-emitting diodes (OLEDs) and thin film. (a) Cavity-based F8BT OLEDs with the structure of Bottom DBR/ITO/PEDOT:PSS/F8BT/TPBi/LiF/Al/Top DBR; (b) Energy diagram for F8BT OLEDs; (c) Absorption and PL spectra for F8BT thin film; (d) Reflective spectra at normal incidence angle to bottom DBR used in high-Q, intermediate-Q and low-Q microcavity OLEDs.

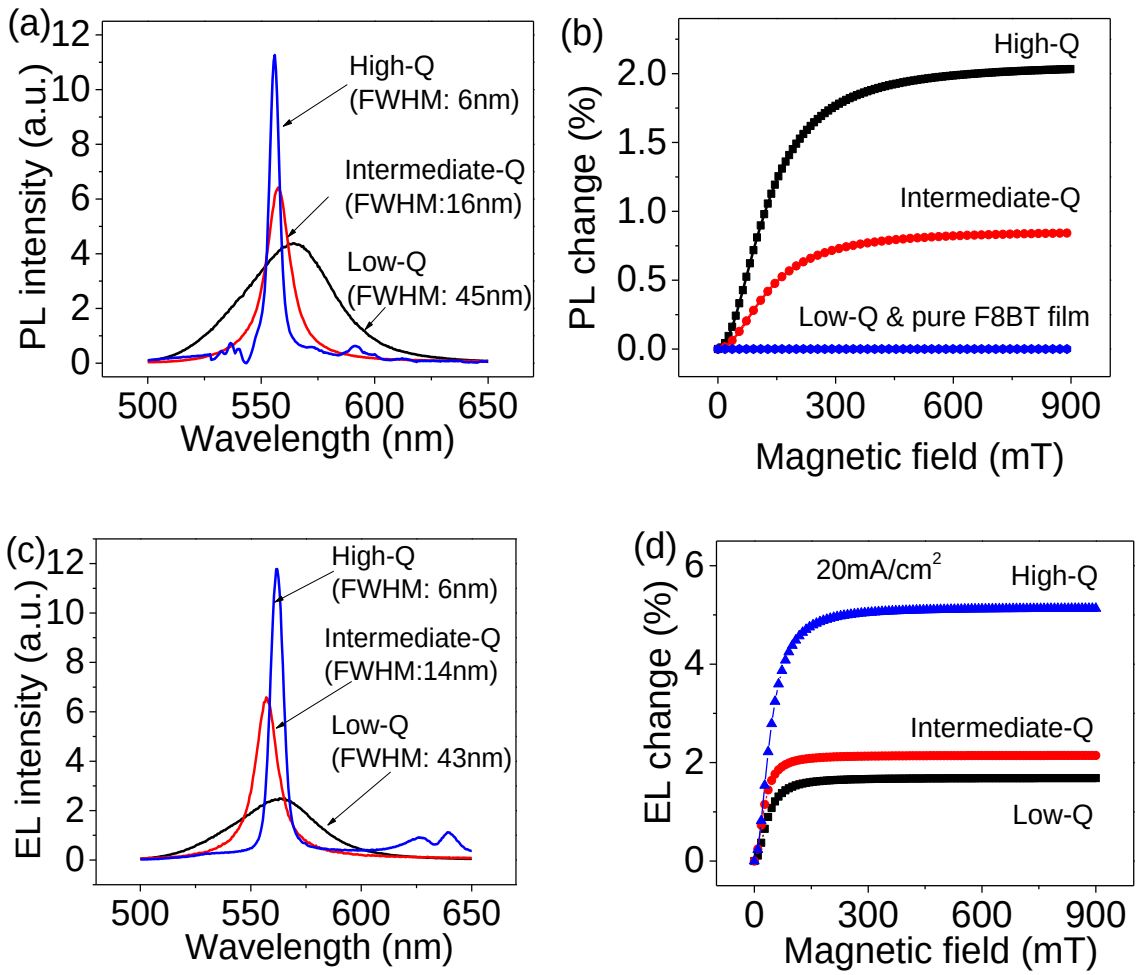

Figure 2-2 Magneto-PL and magneto-EL for cavity-based OLEDs. (a) Narrow PL spectra for cavity-based OLEDs with different Q-factors under CW 405 nm laser excitation; (b) Magneto-PL for cavity-based OLEDs with different Q-factors and F8BT thin film at excitation intensity of 1000 mW cm^{-2}; (c) Narrow EL spectra for cavity-based OLEDs with different Q-factors; (d) Magneto-EL for cavity-based OLEDs with different Q-factors at constant injection current (20 mA cm^{-2}).

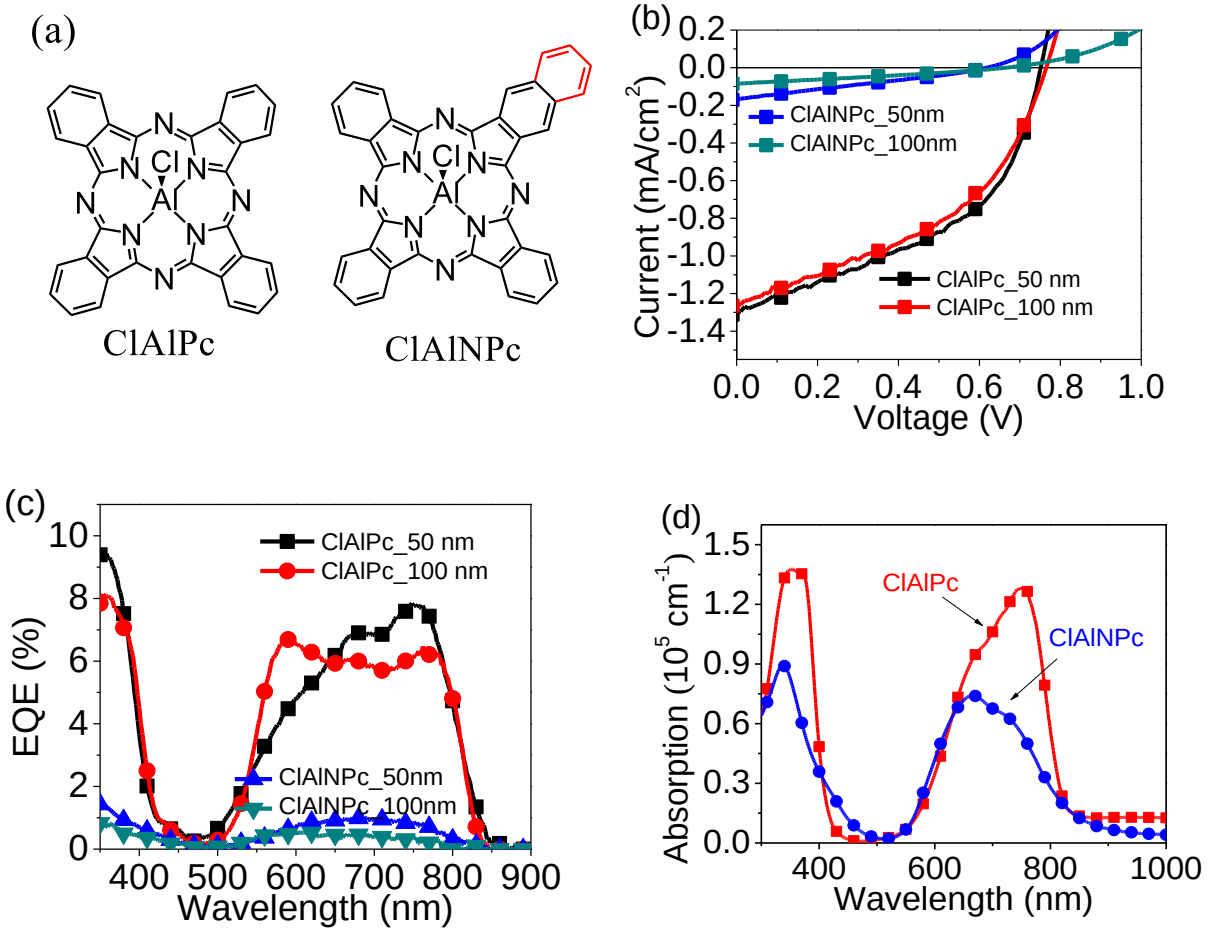

Figure 2-3 Photovoltaic devices performance characterization. (a) Chemical structures for ClAlPc and ClAlNPc molecules; (b) I-V curves under one sun condition for single-layer ClAlPc and ClAlN1Pc devices (ITO/ClAlPc/Al and ITO/ClAlNPc/Al). (c) EQE for ITO/ClAlPc or ClAlNPc/Al devices. (d) Absorption spectra of ClAlPc and ClAlNPc thin films with the same thickness (50 nm).

Table 2-1 Photovoltaic parameters of ClAlPc and ClAlNPc single active layer devices.

Device	V_{OC} (V)	J_{SC} (mA/cm^2)	FF (%)	PCE (%)
ClAlPc 50nm	0.76	1.3	45.42	0.45
ClAlPc 100nm	0.77	1.27	42.9	0.42
ClAlNPc 50nm	0.62	0.17	26.36	0.03
ClAlNPc 100nm	0.67	0.09	28.59	0.02

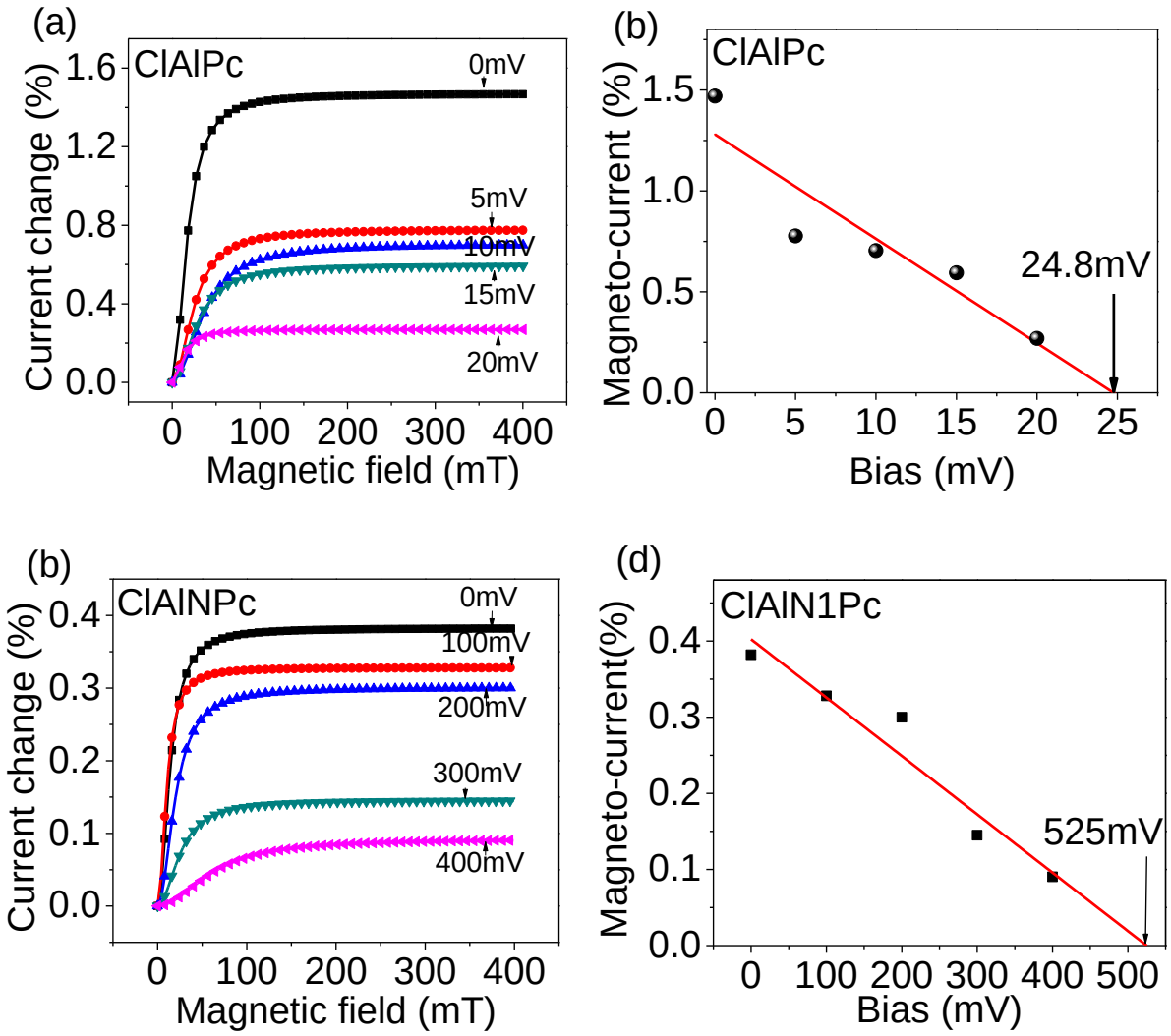

Figure 2-4 Bias-dependent magneto-photocurrent for ClAlPc and ClAlNPc single layer devices. (a) bias dependent magneto-photocurrent and (b) magneto-photocurrent as the function of applied reverse bias for single layer ClAlPc device (ITO/ClAlPc 50nm/Al);(c) bias-dependent magneto-photocurrent and (d) maximum magnitude of magneto-photocurrent as the function of applied reverse bias for single-layer device ClAlNPc device (ITO/ClAlNPc (50 nm)/Al).

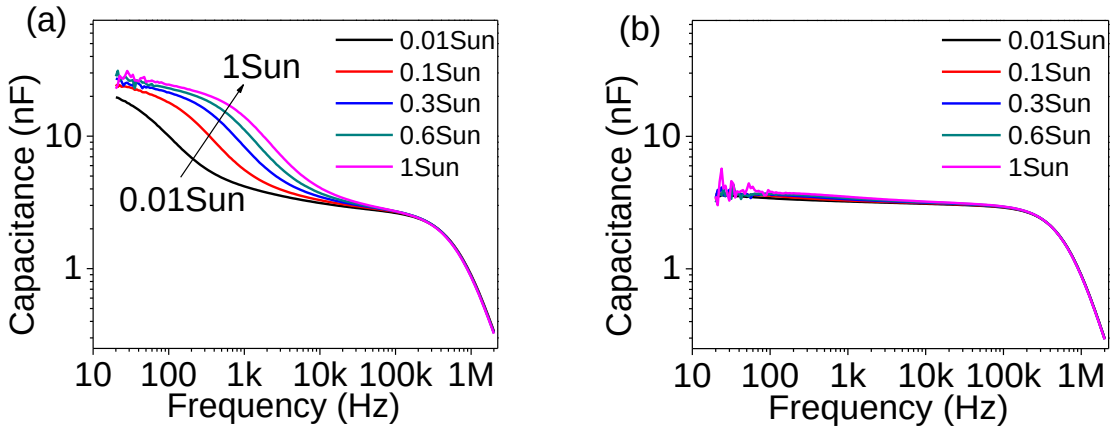

Figure 2-5 C-f curves under simulated sunlight with variable intensities. (a) ClAlPc device (ITO/ClAlPc (50 nm)/Al). (b) ClAlNPc device (ITO/ClAlNPc (50 nm)/Al).

Chapter 3. Spin-Orbital Coupling effects in organic thermally activated delayed fluorescence molecules with intramolecular charge-transfer states

3.1 Abstract

Spin mixing has been recognized as the critical process to enable the conversion from non-radiative triplets into radiative singlets, leading to thermally assisted delayed fluorescence (TADF) in organic TADF molecules with donor-acceptor (D-A) design. This chapter explores the spin-orbital coupling effects responsible for efficient spin mixing in TADF molecules by using magneto-optical methods. In the first part (Chapter 3.4.1), the magneto-PL signal is observed at a high field (up to 900 mT) SOC regime in a typical TADF emitter DMAC-TRZ in solutions. Furthermore, SOC is confirmed to be responsible for realizing spin flipping by directly monitoring the delayed fluorescence while the density of non-radiative triplets is changed by oxygen molecules. More importantly, by using solvent polarity to change the dipole moment in charge-transfer (CT) states, it is revealed that SOC-induced spin flipping is largely changed, presenting a unified relationship between SOC and dipole moment to control the spin flipping to enable the conversion from non-radiative triplets into radiative singlets in TADF. This part is revised based on the published article [M. Wang, T. Chatterjee, C. J. Foster, T. Wu, C.-L. Yi, H. Yu, K.-T. Wong, B. Hu, J. Mater. Chem. C 2020, 8, 3395.]. [47] In the second part (Chapter 3.4.2), we further investigate the spin mixing channels of intramolecular and intermolecular CT states based on a synthesized donor-acceptor-donor (D-A-D) type molecule DMTD-Cz. The PL spectra indicate that the DMTD-Cz molecule shows intramolecular CT states-only in solutions but both intramolecular and intermolecular CT states in solid-state thin films, allowing to separately identify the spin mixing occurring in intramolecular and intermolecular CT states by using magneto-PL measurements. More importantly, the intramolecular and intermolecular CT states exhibit negligible and appreciable magneto-PL signals up to 900 mT at room temperature, respectively. Simultaneously, the intramolecular and intermolecular CT states are shown negligible and appreciable delayed fluorescence, respectively, in thin films. These results provide the direct observation that the SOC generates trivial and vital spin mixing within intramolecular

and intermolecular CT states. This indicates that the triplets in intermolecular CT states can be harvested by using spin mixing mechanism while the triplets in intramolecular CT states should be harvested by using spin conserving mechanism through localized triplet excitons towards developing efficient organic light-emitting materials. This part is revised based on the published article [M. Wang, H. S. Shin, F. Zhou, H. Xu, P. Prabhakaran, B. Dryzhakov, H. Su, K.-S. Lee, B. Hu, J. Phys. Chem. C 2020, 124, 14832.]. [48]

3.2 Introduction

The success of thermally activated delayed fluorescence (TADF) provides an excellent example to indicate that spin-flipping functions as the necessary condition to harvest non-radiative triplets into radiative singlets towards developing high external quantum efficiency (EQE) in organic light-emitting diodes (OLEDs).[49] The experimental studies have indicated that the spin flipping is largely enhanced upon decreasing the singlet-triplet energy difference (ΔE_{ST}) in TADF molecules.[50, 51] There must exist a mechanism to effectively flip the spins of triplets to enable the reverse intersystem crossing (rISC) into light-emitting singlets in TADF molecules. Based on the success of 2nd generation of phosphorescence organic emitters where spin-orbital coupling (SOC) functions as an efficient mechanism to flip the spins of triplet excitons upon using heavy elements, we can expect that TADF molecules possess a strong SOC to enable the spin-flipping to harvest triplet excitons. Several factors can initiate SOC in organic materials such as heavy element effects, aromatic carbonyls, and hydron bonding.[52] Among these factors, the heavy element effect is the most efficient one to generate SOC and consequently harvest triplet states through the phosphorescence process in organic light-emitting materials. However, the experimental investigations on SOC effects in organic TADF emitters with only light elements are still in urgent need.

It is generally believed that decreasing the ΔE_{ST} is an essential approach to facilitate the conversion from non-radiative triplet states to singlet states for generating an efficient TADF. However, the opposite examples of poor TADF compounds with very small ΔE_{ST} and very efficient TADF compounds with large ΔE_{ST} of few hundreds of meV have indicated that energy splitting is not the only determining parameter in the TADF system.[53-55] Indeed, the ΔE_{ST}-dependent rISC can be

validated to generate TADF only if SOC is existed to induce spin flipping of triplet excitons.[56] When the SOC is established as the spin flipping mechanism, the spin mixing between singlets and triplets can be then controlled by the energy parameter. Generally, the spin mixing rate (λ) can be expressed as $\lambda = H_{SO}/\Delta E_{ST}$, where H_{SO} and ΔE_{ST} are the SOC constant and energy difference between S_1 and T_1 states.[57] Therefore, the spin flipping is the precondition to validate the ΔE_{ST}-dependent rISC. However, it has been remained as an un-raveled issue to experimentally address SOC effects responsible for operating high-efficiency TADF. Further intriguingly, after spin flipping, the triplet states must undergo an endothermic process via thermal energy to reach the light-emitting singlets states towards generating a high-efficiency TADF rather than to exothermically relax to the ground state (S_0) for a low-efficiency phosphorescence. This requires an electric-magnetic coupling between singlets and the triplets to enable the rISC towards TADF by preventing the triplet-to-S_0 phosphorescence. In this chapter, we utilized magneto-optical methods in both steady and time-resolved regimes to explore the underlying spin-dependent processes TADF process by using TADF molecule DMAC-TRZ (chapter 3.4.1) and DMTD-Cz (chapter 3.4.2).

3.3 Experimental methods

3.3.1 Materials preparation

DMAC-TRZ molecule was synthesized by Dr. Ken-Tsung Wong's group.[58] The concentration of the liquid solution used for the measurements was 10 mg mL^{-1}. DMTD-Cz molecule was synthesized by Dr. Kwang-Sup Lee's group. The concentration of the liquid solutions of DMTA-Cz used for the measurements was 0.1 mg mL^{-1}. The DMTD-Cz thin film samples with a strong yellow emission band were prepared by thermal evaporation under a high vacuum of 5×10^{-7} torr. The precursor solutions to prepare the spin-casted DMTD-Cz thin films are DMTD-Cz in toluene (3 mg mL^{-1}) and DMTD-Cz (3 mg mL^{-1}) + PMMA (5 mg mL^{-1}) in toluene. The concentration of the DMTD-Cz solution samples used in this study is 5×10^{-4} M.

3.3.2 Magneto-PL measurements

The magneto-EL and magneto-PL measurements were performed by using Horiba Fluorolog 3 spectrometer combined with an electrically controllable magnet. The excitation is from the laser beams.

3.3.3 Absorption and PL characterizations

Absorption spectra of the dilute solutions were characterized on quartz substrates by using UV/VIS spectrometer (Lambda 35, PerkinElmer Instruments) under transmission mode. The PL spectra were measured by using Horiba Fluorolog 3 spectrometer. Time-resolved PL measurements were performed by using the time-correlated single-photon counting (TCSPC) system in Horiba Fluorolog 3 spectrometer. The excitation source was from a nanosecond pulse 371 nm nanoLED for the studies on DMAC-TRZ molecules. The femtosecond pulse laser beam (343 nm, 0.8 nJ cm^{-2}) from the Pharos laser (Light Conversion) combing the harmonic generator (Ultrafast Systems LLC) was used for the measurements of DMTD-Cz molecules. The samples were placed in a vacuum cryostat chamber with the temperature control from a closed-cycle cryostat (Advanced Research Systems).

3.4 Results and Discussions

3.4.1 Spin-orbital coupling effects responsible for efficient spin mixing in TADF molecules

Here, the magneto-EL is used to show the existence of SOC as the dominant spin-flipping mechanism in TADF process by comparing the highly efficient TADF emitter DMAC-TRZ with the traditional fluorescence organic emitter poly(p-phenylene vinylene) (MEH-PPV). The EL spectra of the DMAC-TRZ and MEH-PPV based OLEDs are shown in **Figure 3-1a**. Then we measured the magneto-EL for both OLEDs under constant current mode. We must note that MFEs can occur in hyperfine interaction (HFI) (< 10 mT) or SOC (> 10 mT) regimes when an external magnetic field competes with HFI or SOC to change the singlet and triplet populations, generating the so-called spin-mixing between singlet and triplet states. When the SOC is absent and the HFI governs the spin-mixing, MFEs always occur at low field (< 10 mT).[59, 60] Indeed, in MEH-PPV OLED with negligible SOC, the internal magnetic parameter (B_0) of the magneto-EL curve is in the HFI regime (6.4 mT), as shown in **Figure 3-1b**. When the SOC exists, MFEs can be observed at high field and the width of the curves becomes significantly broader as compared with HFI

condition.[61-63] Therefore, the high field MFEs can serve as evidence to indicate that the SOC is formed to function as the dominating mechanism for spin-flipping in organic systems.[64, 65] Interestingly, we observed magneto-EL in DMAC-TRZ based OLED in high field with much broader curve shape (B_0=70.5 mT), as compared with MEH-PPV based OLED in HFI regime with narrow curve shape. Clearly, this high field magneto-EL in DMAC-TRZ based OLED provides direct evidence to show the existence of SOC as the dominant spin-flipping mechanism in TADF process.

Then we used magneto-PL to illuminate how the SOC is formed to initiate the spin mixing towards TADF process based on DMAC-TRZ molecule in solutions. The molecular structure of the TADF emitter DMAC-TRZ used in this work is shown as the inset in **Figure 3-2a**. **Figure 3-2a** shows the UV-Vis absorption spectrum of DMAC-TRZ in toluene solution. The strong absorption of DMAC-TRZ at around 300 nm belongs to the π-π* excitonic transition, while the broad absorption peak at 386 nm is attributed to the intramolecular CT states. The DMAC-TRZ molecule contains D-A structure within a π-conjugated system. As a result, both excitonic and CT states co-exist within proximity. **Figure 3-2b** shows the PL spectra from DMAC-TRZ toluene solution under 325 nm, 375 nm, and 405 nm continuous wave (CW) laser excitations. The same light-emitting states (^{1}CT) in DMAC-TRZ molecule are generated under different photoexcitation wavelengths, as indicated by the similar PL spectra. **Figure 3-2c** shows interesting magneto-PL behaviors of DMAC-TRZ in toluene solution at different excitation wavelengths (325 nm, 375 nm, and 405 nm) from the laser beams. The magneto-PL signals were observed at the magnetic field much larger than the HFI field strength, confirming that the SOC is indeed formed in this TADF-based molecule. Moreover, it is very interesting to note that this high-field magneto-PL can be observed only if the CT states are excited. For example, exciting CT states by using the photoexcitation at 405 nm and 375 nm generates an appreciable magneto-PL signal at a high field with the B_0 of 224 mT. This reveals that the SOC occurs in CT states. In contrast, exciting the excitonic states by using 325 nm laser beam leads to a negligible magneto-PL signal, indicating that the SOC is lacking in excitonic states. We should note that, by using short-wavelength excitation to excite localized excitonic states, the CT states can be also formed through charge separation. However, the efficiency of generating CT states through localized states separation is much lower than

directly exciting CT states with long-wavelength excitation, as shown in the excitation spectrum in **Figure 3-2d**. Therefore, short-wavelength and long-wavelength excitations can generate low and high densities of CT states, respectively. Clearly, our magneto-PL results show that exciting CT and excitonic states lead to appreciable and negligible SOC in DMAC-TRZ molecules.

Here, the observed magneto-PL signals in organic TADF molecule indicate that there must exist a mechanism to generate SOC by using CT states. Here, we consider that photo-induced charge transfer between the donor (D) and acceptor (A) leads to positively and negatively charged moieties (D^+ and A^-) in a CT state, giving an optically induced dipole $D^+ \rightarrow A^-$. Before exciting CT states, the D and A have negligible SOC due to isotropically distributed orbitals. We propose that the isotropically distributed orbitals are asymmetrically polarized by the optically induced dipole $D^+ \rightarrow A^-$ in CT states. Consequently, asymmetrically polarized orbitals interact with spins on D^+ and A^-, generating SOC within CT states, as schematically illustrated in **Figure 3-2e**. This proposed scenario can be supported by our previous studies, where we found that an optically excited CT state can directly interact with the ferromagnetic nanoparticle, leading to MFEs in the SOC regime (> 10 mT).[66, 67] This observation indicates that the interaction between an electric dipole and a spin dipole can be equivalently considered as SOC. Clearly, the SOC formed in the CT states of a TADF-based molecule provides the necessary mechanism to flip the spins to enable the TADF.

Then, we investigated the SOC-enabled spin flipping to generate TADF through rISC process. In general, there are three possibilities for spin-mixing to occur within excitonic states (between ^{1}LE and ^{3}LE), within CT states (between ^{1}CT and ^{3}CT), and between excitonic and CT states (^{3}LE to ^{1}CT). It should be noted that both excitonic and intramolecular CT states have a strong exchange interaction due to the short electron-hole distance. A strong exchange interaction can largely enhance the spin-conservation behavior, minimizing intersystem crossing between singlet and triplet states. This leads to the only possibility that the intersystem crossing occurs between CT and excitonic states in TADF molecules. Here, we simultaneously monitored the spin-mixing and delayed fluorescence while the density of triplet excitons is changed by using O_2 gas. Using O_2 is a practical method to quench the excited states in solutions.[68, 69] In principle, the O_2 can react

with both excitons and CT states. However, in excitonic states, the O_2 can more selectively react with ^{3}LE due to largely different lifetime and ionic properties between ^{1}LE and ^{3}LE. In CT states, the O_2 can react with both ^{1}CT and ^{3}CT because of a similar lifetime and ionic properties between ^{1}CT and ^{3}CT. Therefore, using the O_2 can confirm the spin flipping occurring in triplet excitons while monitoring magneto-PL. It can be seen in **Figure 3-3a** that the delayed fluorescence intensity is largely decreased upon introducing O_2 molecules. The PL quenching shown in **Figure 3-3b** provides a further indication that introducing O_2 molecules can decrease the density of triplet excitons with the consequence of quenching the delayed fluorescence. Concurrently, the spin-mixing disappeared, shown as a negligible magneto-PL signal (**Figure 3-3c**). In contrast, the magneto-PL signal is preserved under N_2 condition, indicating that the spin-mixing occurs when the triplet excitons are maintained. The simultaneous occurrence of spin-mixing and delayed fluorescence provides direct evidence to support that the SOC flips the spins of triplet excitons to generate a TADF through rISC. The early publications have proposed that the ^{3}LE state can reach an equilibrium with the ^{3}CT state through spin-conserving process and followed by a spin-mixing from ^{3}LE to ^{1}CT to generate a TADF.[70-72] In our studies, we can see that the spin-mixing does not occur in intramolecular CT states (between ^{1}CT and ^{3}CT) because the magneto-PL signal, used to show spin-mixing, disappeared when the ^{3}LE states are quenched by the O_2 molecules. The absence of spin-mixing in intramolecular CT states implies that the CT states have a strong exchange interaction due to the short D-A distance to prevent the ^{3}CT to ^{1}CT conversion. We should note that the absence of spin-mixing in CT states does not cause a loss of the TADF since the ^{3}CT states can convert into ^{3}LE states through spin-conserving process. When the SOC in CT states flips the spins of ^{3}LE state, then spin-mixing occurs from ^{3}LE state to ^{1}CT state towards generating a TADF. This is confirmed by comparing the PL decay curves measured under zero field and magnetic field of 200 mT, in which the time-resolved magneto-PL can be extracted. **Figure 3-4a** shows that in nitrogen condition with the presence of the high field of 200mT, the PL change gradually increases with decay time, reaching 20 % at 102 ns. When the delayed fluorescence is largely reduced by using O_2 molecules to quench the triplet excitons, the PL lifetime becomes insensitive to the magnetic field within the entire time window up to 5 μs (**Figure 3-4b**). Clearly, the results obtained from time-resolved magneto-PL confirm that the SOC in the

CT states flips the spins of ^{3}LE state, generating a spin-mixing to convert the ^{3}LE state into ^{1}CT state towards TADF.

The solvent polarity effects are used to further test the SOC required to allow the spin-mixing between ^{1}CT and ^{3}LE. The polarity of the environment can change the dipole moment and the energy level of CT states while leaving the LE states almost unaffected, leading to solvatochromism effects.[58, 73] Here, we use magneto-PL to monitor the spin-mixing while the dipole moment and energy level of the CT states is changed by increasing the solvent polarity. As shown in **Figure 3-5a**, increasing the solvent polarity from hexane (relative polarity 0.009) to p-xylene (relative polarity: 0.077), and toluene (relative polarity: 0.099) leads to a red-shift on the PL spectrum with the peak wavelength changing from 441 nm to 489 nm and 495 nm, respectively. Clearly, increasing the solvent polarity can down-shift the energy of CT states towards the local excitonic states, increasing the delayed fluorescence component (**Figure 3-5 b** and **c**). Simultaneously, we can see in **Figure 3-5d** that the spin-mixing is largely increased as the solvent polarity is increased, as shown by the increased magneto-PL in high field SOC regime. Furthermore, it can be seen that with further increased solvent polarity in chlorobenzene solution (relative polarity 0.188), both TADF efficiency and magneto-PL signal are reduced as compared with the toluene solution condition because CT states move out of resonance with the LE states. Clearly, this magneto-PL result provides a direct experimental confirmation to show that the spin-mixing is increased through SOC-enabled spin flipping as the energy difference between ^{1}CT state and excitonic state (^{3}LE) is decreased in TADF molecules.

Here we discuss the electric magnetic coupling between ^{1}CT and ^{3}LE to enable the spin-dependent TADF. Our magneto-PL studies indicate that the spin-mixing is occurring from ^{3}LE state to ^{1}CT state when the SOC in CT states flips the spins of triplet excitons, as illustrated in **Figure 3-6**. It should be pointed out that triplet excitons can generate two outcomes after spin flipping by SOC: (i) a delayed fluorescence through endothermic rISC process from ^{3}LE state to ^{1}CT state; (ii) a phosphorescence through the exothermic process from ^{3}LE state to the ground state (^{0}S). The experimental observation of delayed fluorescence implies that there must be an attractive interaction between ^{1}CT and ^{3}LE states to enforce the endothermic process from ^{3}LE state to ^{1}CT

state towards generating delayed fluorescence. Essentially, this attractive interaction together with thermal energy can enable the conversion from ^{3}LE state to ^{1}CT state through an endothermic process which generates delayed fluorescence by preventing the ^{3}LE state relaxing to ground state after the SOC flips the spins of ^{3}LE state. Therefore, the contribution of phosphorescence to the total emission in TADF process is negligible especially at room temperature. It is noted that the vibronic coupling has been proposed to explain the coupling between ^{3}LE and ^{3}CT states based on the observation where the TADF is a function of host polarity.[70-72] Here we consider an electric-magnetic coupling between ^{1}CT and ^{3}LE states as the necessary condition to enable the $^3\text{LE} \rightarrow {}^1\text{CT}$ intersystem crossing. The electric-magnetic coupling can occur with very weak spins such as paramagnetic materials when placed within proximity with electrical dipoles.[74, 75] And triplet excitons can be regarded as paramagnetic.[76] Furthermore, we found that an electric-magnetic coupling can indeed exist between an electric dipole and a spin dipole located within close proximity in ferromagnetic/organic composites.[66, 77] In TADF systems, ^{1}CT and ^{3}LE states are equivalent to electric and spin dipoles, respectively. Therefore, we expect an electric-magnetic coupling between ^{1}CT and ^{3}LE states enables the endothermic $^3\text{LE} \rightarrow {}^1\text{CT}$ intersystem crossing towards TADF, when the energy conversation requirement is satisfied by using thermal energy. The electric-magnetic coupling can occur through three possible channels: 1) long-range Coulomb interaction; 2) midrange spin-orbital coupling interaction; 3) short-range spin-spin interaction, between an electric dipole and a spin. Even though it is still unclear on the contributions for each channel, the electric-magnetic coupling between ^{3}LE and ^{1}CT serves as an important parameter accountable for both spin flipping of ^{3}LE and realizing the endothermic spin-mixing from ^{3}LE to ^{1}CT to generate a high-efficiency TADF.

The electric-magnetic coupling between ^{3}LE and ^{1}CT states allows the conversion from ^{3}LE state to ^{1}CT state, in which the spin-mixing process is accountable for TADF after the SOC in CT states flips the spins of ^{3}LE state. For a high-efficiency TADF, the ^{1}LE and ^{3}CT states must be converted into the light-emitting ^{1}CT state to avoid a loss in excited states. The ^{1}LE state can directly relax to light-emitting ^{1}CT state through a spin-conserving process, according to the PL generated from CT states by exciting excitonic states. Similarly, the ^{3}CT states can relax to ^{3}LE states under spin conservation followed by the spin-mixing towards light-emitting ^{1}CT state. Therefore, both ^{1}LE

and ^{3}CT states can effectively be converted to the light-emitting ^{1}CT state. We should further note that there is a possibility that the ^{3}LE state may be converted to ^{3}CT state under thermal activation through spin-conserving process. If this occurs, it would generate a loss in TADF since the strong exchange interaction does not allow the $^3CT \rightarrow {}^1CT$ conversion. However, this possibility can be eliminated because the spin-mixing from ^{3}LE state to ^{1}CT state can shorten the lifetime of ^{3}LE state as compared to the rate of $^3LE \rightarrow {}^3CT$ conversion, consequently suppressing the backward conversion from ^{3}LE state to ^{3}CT state and enhancing the forward conversion from ^{3}CT state to ^{3}LE state to avoid any loss in TADF.

3.4.2 Identifying Different Spin Mixing Channels Occurring in Charge-Transfer States

The chemical structure of the DMTD-Cz molecule is shown in **Figure 3-7**. It adopts the donor–acceptor-donor (D-A-D) molecular architecture of TADF emitters, with Cz moieties as the electron-donor moiety and DMTD as the electron-acceptor moiety. Because of the strong electron-withdrawing characteristics of the sulfone groups, the LUMO is localized on the DMTD core moiety, i.e. phenoxathiin dioxide, whereas the HOMO is distributed mainly at the Cz moieties on the side chain. Generally, the effective separation between HOMO and LUMO in TADF molecules with the formation of intramolecular CT states is believed to be beneficial for reducing ΔE_{ST} for efficient spin mixing between triplets and singlets. Intriguingly, DMTD-Cz molecules exhibit well-separated dual emission from the co-existing intra- and intermolecular CT states in solid-state thin films prepared by thermal evaporation. The absorption and PL spectrum of the DMTD-Cz film is shown in **Figure 3-8a**. The blue emission band comes from the high-energy intramolecular CT states while the broad yellow emission band results from the low-energy intermolecular CT states formed in thin films. The intermolecular CT states should have a larger electron-hole distance as compared with the intramolecular CT states that are limited by the physical size of the molecule. Indeed, when the electron-hole separation is increased, the emission of CT states shifts to a longer wavelength.[78] Therefore, the formation of intermolecular CT states in neat films can lead to red-shifted emission. [79] The initially formed intramolecular CT states upon photoexcitation can be energy-transferred to form the low-energy intermolecular CT states. Note that a D-A type organic molecule PTZ-BP with dual emission has been observed in both solid states and solutions. It was claimed the dual emission originates from the local excited states and

intramolecular CT states, [80] which is different from our case. On the other hand, the co-existing intra- and intermolecular CT states have been reported in a molecule PhCz-*o*-Trz in films by tuning the concentrations. [79] In this work, the blue emission band exists in both pristine thin films and solutions of DMTD-Cz molecule while the additional broad yellow emission band only shows up in thin films. With the dual emissions from both intra- and intermolecular CT states, the DMTD-Cz thin films serve as the perfect platform to investigate the spin mixing channel in TADF molecules. Here, we investigated whether spin mixing can occur within intra- or intermolecular CT states by using magneto-PL measurements in DMTD-Cz thin films. In general, the intersystem crossing is determined by the competition between spin conserving force from exchange interaction and spin mixing force due to internal magnetic interactions such as hyperfine interaction (HFI) or SOC. A magnetic field can change the populations on singlet and triplet electron-hole pairs by perturbing intersystem crossing, leading to magneto-PL. It should be noted that excitonic states have a strong exchange interaction due to short electron-hole separation distance. A strong exchange interaction can largely enhance the spin conserving behavior, minimizing intersystem crossing between singlets and triplets. Thus, excitonic states only show negligible magneto-PL because the strong exchange interaction does not allow the magnetic field to change the populations on singlets and triplets. On the contrary, it has been shown that the electron-hole pairs including intermolecular CT states and polaron pairs can demonstrate the appreciable magneto-PL due to weak exchange interaction which allows magnetic field-dependent populations on singlets and triplets. As shown in **Figure 3-8b**, positive magneto-PL signals can be observed in intermolecular CT states emission at 540 nm with the magnetic field up to 900 mT while the blue emission band from intramolecular CT states show negligible magneto-PL. Note that magneto-PL has been reported in an exciplex system with mixed D and A molecules, which was attributed to the difference in the g-values of carriers that reside in the D and A molecules, namely, the Δg mechanism.[18] However, in our case of DMTD-Cz with dual emissions, the Δg should be similar for both intra- and intermolecular CT states since they have the same D and A moieties. But the magneto-PL was only observed in yellow emission band from the intermolecular CT states. Therefore, we do not expect the Δg mechanism to play the dominate role in the observed positive magneto-PL from the intermolecular CT states in DMTD-Cz films. Instead, we must note that magneto-PL can occur in HFI (< 10 mT) or SOC (> 10 mT) regimes when an external magnetic

field competes with HFI or SOC to change the singlet and triplet populations. The high field magneto-PL signals from intermolecular CT states indicate that the SOC as the spin flipping mechanism dominates the triplet-to-singlet conversion in intermolecular CT states to generate TADF. Within a CT state the donor and acceptor become positively and negatively charged ions, leading to an electrical dipole $D^+ \rightarrow A^-$. On the other hand, the D and A have negligible SOC due to isotropically distributed orbitals. Essentially, the appreciable SOC can be generated within an intra- or intermolecular CT state when the electrical dipole $D^+ \rightarrow A^-$ partially polarizes the isotropic orbitals on the D and A moieties.[47] Yet the strong exchange interaction prevents the direct conversion between triplets and singlets in intramolecular CT states, as reflected by the negligible magneto-PL at the blue emission band.

To further compare the spin mixing behavior in intra- and intermolecular CT states, we have performed the temperature-dependent time-resolved PL measurements to detect the PL decay dynamics. It can be seen in **Figure 3-8c** that the blue emission band from the intramolecular CT states only shows a prompt fluorescence with a lifetime of 1.8 ns at the room temperature. This confirms the conversion between triplets and singlets is lacking within the intramolecular CT states. Moreover, the PL dynamics do not show obvious change in the temperature range from 40 K to 300 K. Interestingly, the yellow emission band from intermolecular CT states in DMTD-Cz thin film exhibits a multi-exponential decay feature composed of prompt fluorescence with a lifetime of 26 ns and a delayed fluorescence with a lifetime of 3.6 μs at room temperature (**Figure 3-8d**). More importantly, the delayed component drops upon lowering the temperature and disappears at 40 K, confirming that it is indeed TADF. Clearly, our magneto-PL and time-resolved PL results indicate that efficient spin mixing can occur within intermolecular CT states to generate TADF with the presence of SOC and weak exchange interactions.

The photophysical properties of DMTD-Cz in solutions were investigated to further confirm whether spin mixing can occur within intramolecular CT states. The absorption spectra of DMTD-Cz in hexane, toluene, and chlorobenzene solvents are shown in **Figure 3-9a**, where the relative polarities for these solvents are 0.009 (hexane), 0.099 (toluene), and 0.188 (chlorobenzene), respectively. It can be seen that the absorption peak shows a red-shift by increasing the polarity

of the solvent. **Figure 3-9b** shows the PL spectra of the DMTD-Cz molecules in hexane, toluene, and chlorobenzene solvents. Clearly, there is only one blue emission band from DMTD-Cz in solution conditions, which is similar to the high energy emission band in solid-state thin films. Moreover, the PL spectrum gradually red-shifts with increasing solvent polarity. Thus the characteristic of intramolecular CT states in the DMTD-Cz molecules is evidenced by the solvatochromic behavior of the PL spectra in solvents with different polarities.[81] If the blue emission band comes from the localized excitons, then negligible solvatochromic behavior should be observed. Moreover, the time-resolved PL of the DMTD-Cz molecules in these three solvents exhibits a clear single-exponential decay with negligible delayed fluorescence (**Figure 3-9c**). This indicates that the spin mixing between singlets and triplets is inefficient to generate TADF even with the presence of intramolecular CT states. We now further investigate whether intramolecular CT states can undergo spin-flipping in D-A-D type DMTD-Cz molecules in solutions by using magneto-PL measurements. Here, negligible magneto-PL can be observed on DMTD-Cz molecules in solutions with intramolecular CT states (**Figure 3-9d**). This verifies that the intramolecular CT states only, similar to excitonic states, cannot demonstrate efficient spin mixing due to the strong exchange interaction from a short electron-hole distance within a single molecule. Indeed, it is generally believed that the efficient intersystem crossing in D-A or D-A-D type TADF molecules can occur between singlet CT state (^{1}CT) and triplet localized excitonic state (^{3}LE) to generate TADF when the ΔE_{ST} between ^{1}CT and ^{3}LE is sufficiently small.[70-72] Thus the triplets in intramolecular CT states can be harvested by using spin-conserving mechanism to be coupled with ^{3}LE states.

3.5 Conclusions

Firstly, we found that the TADF molecule (DMAC-TRZ) based OLEDs demonstrated a magneto-EL in high field regime (> 10 mT). This high-field magneto-EL signal provides direct evidence to indicate that the SOC is indeed formed, in the absence of heavy elements, towards developing the spin-dependent TADF in OLEDs. This finding brings two open questions: where is SOC formed and how does SOC enable the spin-mixing towards generating TADF? By using magneto-PL to explore the origin of SOC, we observed that exciting CT states can lead to a magneto-PL signal in SOC regime (high field > 10 mT) with a delayed fluorescence while exciting local excitonic states

does not generate any detectable magneto-PL signal. This observation provides the first experimental indication that the SOC is formed in CT states. We propose that an optically induced electrical dipole between D^+ and A^- can partially polarize the orbitals on D^+ and A^-, and consequently generates a strong SOC within a CT state. To understand the spin-mixing in developing the TADF, we found that decreasing the density of triplet excitons (^{3}LE) by using O_2 can largely decrease the delayed fluorescence and magneto-PL signal, both in steady-state and transient measurements. This result indicates that the SOC in CT states flips the spins of ^{3}LE state to enable the spin-mixing from ^{3}LE state to ^{1}CT state towards TADF. Furthermore, the spin-mixing from ^{3}LE state to ^{1}CT state requires an attractive interaction between ^{3}LE and ^{1}CT states to enable this endothermic process towards delayed fluorescence by avoiding the exothermic spin-mixing from ^{3}LE state to ^{0}S state towards phosphorescence. We consider the electric-magnetic coupling between ^{1}CT and ^{3}LE states as the underlying mechanism to enable the endothermic intersystem crossing ($^3\text{LE} \rightarrow {}^1\text{CT}$) which in turn generates a high-efficiency TADF. Clearly, our magneto-PL studies provide an insightful understanding on the SOC effects of spin-mixing towards generating TADF. We believe that the results disclosed in this work can shed light on the detailed mechanisms involved in TADF with intramolecular CT features and can trigger new ideas for creating more efficient molecules for practical applications in OLEDs.

Secondly, we found that the D-A-D type molecule (DMTD-Cz) exhibits dual emission from co-existed intra- and intermolecular CT states in solid-state thin films, which show negligible and appreciable delayed fluorescence, respectively. More importantly, the negligible magneto-PL signal in intramolecular CT states emission band indicates that the strong exchange interaction prevents the direct conversion between triplets and singlets states in intramolecular CT states with short electron-hole separation distance. Therefore, the triplets in intramolecular CT states cannot be directly converted to singlets and they must be coupled with ^{3}LE states through the spin-conserving process to be harvested. In contrast, the intermolecular CT emission band shows clear magneto-PL signals in high field at the SOC regime. This observation provides direct evidence that the spin mixing can efficiently occur in intermolecular CT states with SOC as the spin flipping mechanism. Clearly, our magneto-PL studies provide a deeper understanding on spin-mixing channels through intra- and intermolecular CT states utilized in TADF and exciplex systems.

Appendix

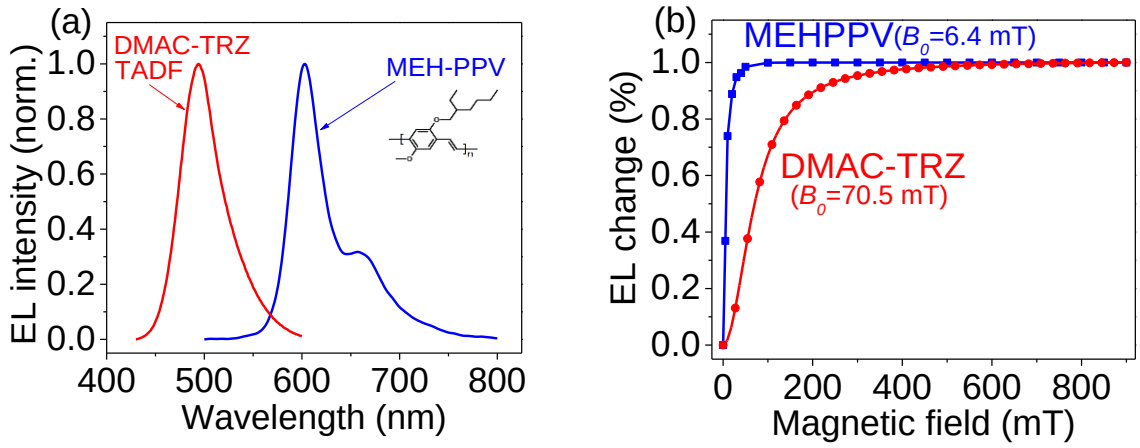

Figure 3-1 (a) EL spectra for MEH-PPV and DMAC-TRZ OLEDs. The OLED devices were fabricated with the structure of ITO/PEDOT:PSS/ active layer/Bphen/Al. (b) Magneto-EL occurring at hyperfine interaction regime (< 10 mT) in MEH-PPV and at spin-orbital coupling regime (> 10 mT) in DMAC-TRZ, shown as narrow and broad curve shapes. The internal magnetic parameter B_0 was fitted by using Lorentzian equation $MFE = \alpha \frac{B^2}{B^2+B_0^2}$.

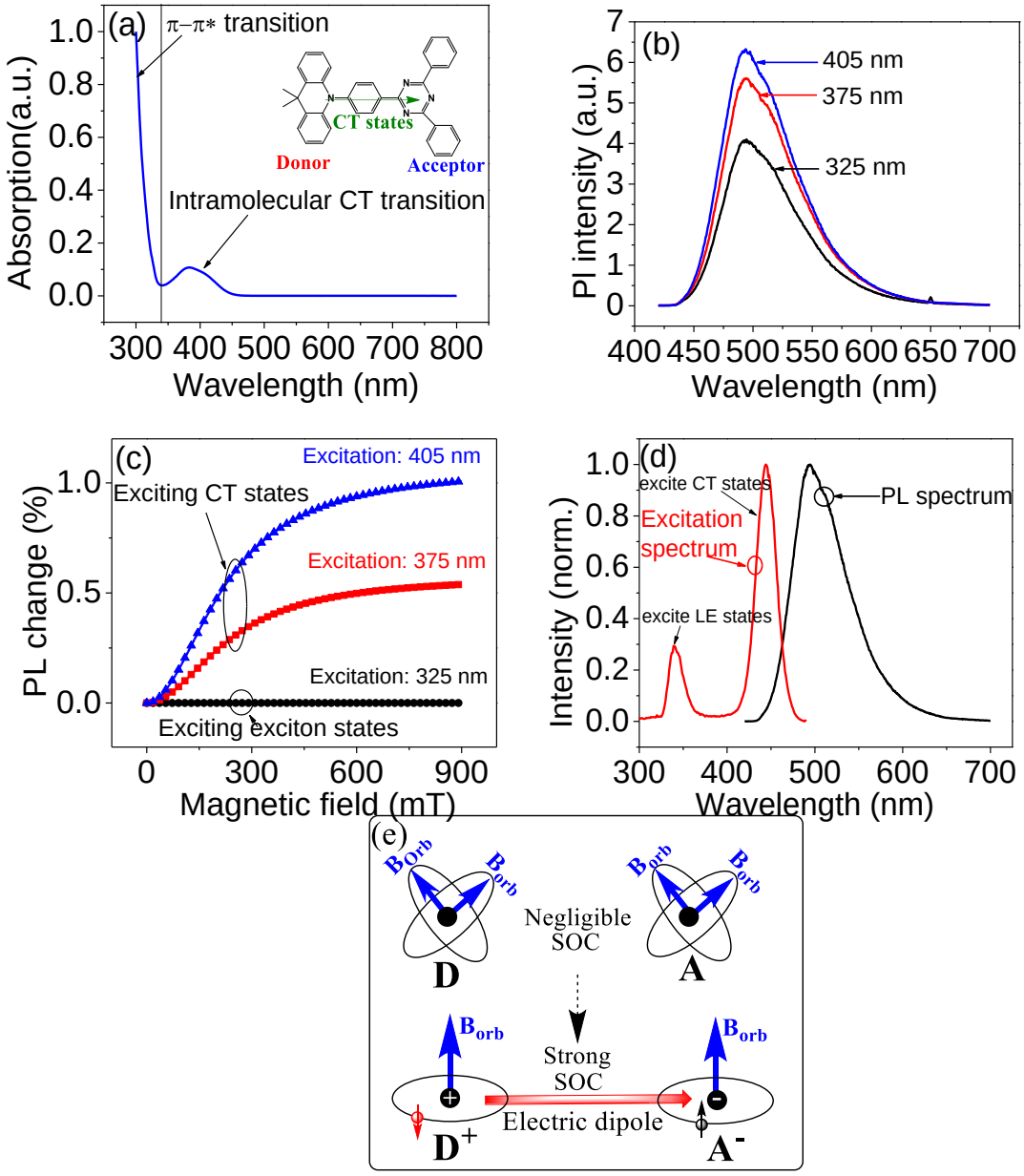

Figure 3-2 Excitation wavelength dependence of magneto-PL. (a) UV-Vis absorption spectrum of DMAC-TRZ in toluene solution. The inset shows the molecular structure of DMAC-TRZ with donor and acceptor moieties; (b) PL spectra and (c) magneto-PL for DMAC-TRZ in toluene solution under 325nm, 375nm and 405nm laser beam excitation; (d) Excitation and PL spectrum for DMAC-TRZ toluene solution. The excitation spectrum is measured by recording the PL peak intensity at 495 nm as the function of the excitation wavelength. PL spectrum is recorded by using 405 nm wavelength excitation. There are two excitation peaks corresponding to localized states excitation and CT states excitation, respectively. The directly excitation of CT states gives stronger emission compared with localized states excitation; (e) SOC generated by polarizing orbitals due to electrical dipole between D^+ and A^- within a CT state.

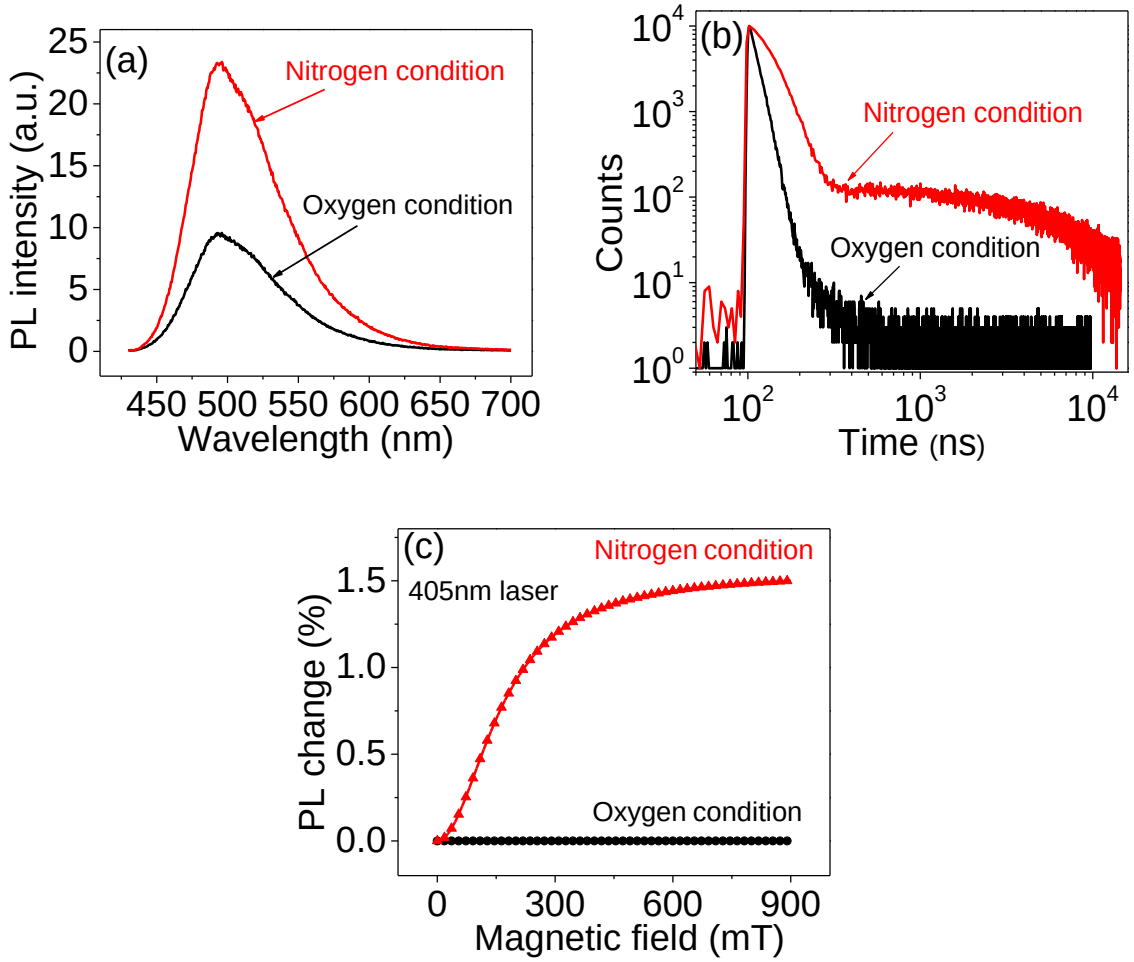

Figure 3-3 Characterization on DMAC-TRZ in toluene solutions separately applied with N_2 and O_2: (a) steady state PL spectra; (b) PL decay curves; (c) magneto-PL signals under 405 nm laser beam excitation with the intensity of 400 mW/cm^2.

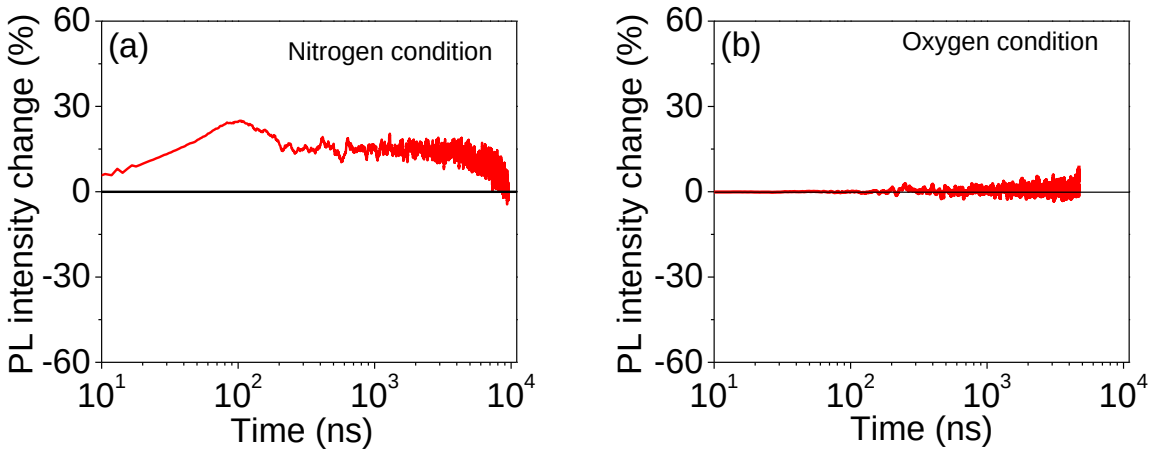

Figure 3-4 PL decay dynamics with magnetic field (200 mT) at SOC regime for DMAC-TRZ in toluene solution. The PL intensity change, defined as (PL $_{magnetic\ field}$ - PL $_{zero\ field}$)/ PL $_{zero\ field}$, is measured by comparing the PL decay curves in magnetic field (200mT) and zero field. (a) PL intensity change as the function of decay time under nitrogen condition. (b) PL intensity change as the function of decay time for oxygen condition. The magnetic field has negligible influence for PL decay dynamics under oxygen condition.

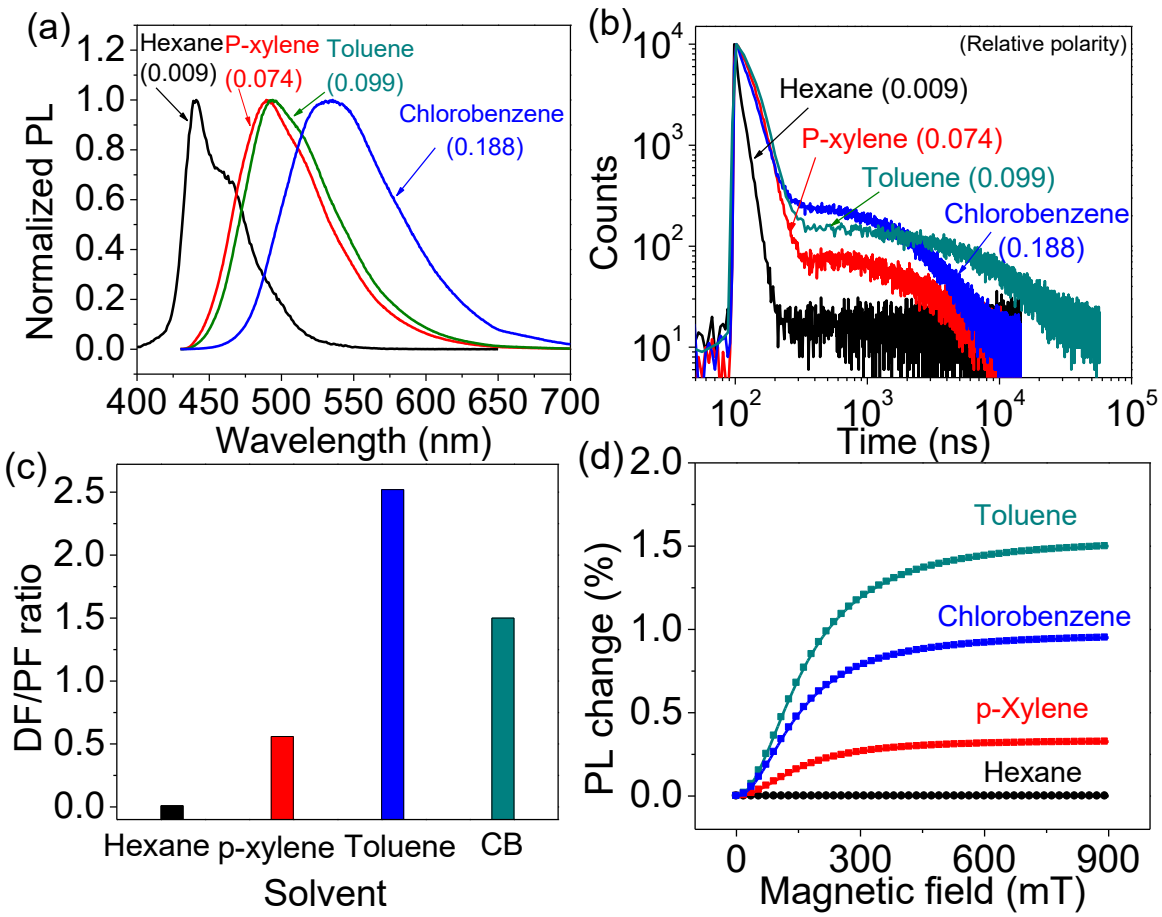

Figure 3-5 Characterization on DMAC-TRZ in solutions with four different solvents: Hexane (relative polarity 0.009), p-xylene (relative polarity 0.077), toluene (relative polarity 0.099), and chlorobenzene (CB) (relative polarity 0.188). The polarity of water is set to be unity. (a) Normalized PL spectra; (b) PL delay curves; (c) DF/PF ratio calculated from PL delay curves; (d) Magneto-PL for those DMAC-TRZ solutions under 405 nm laser excitation with the intensity of 400mW/cm^2.

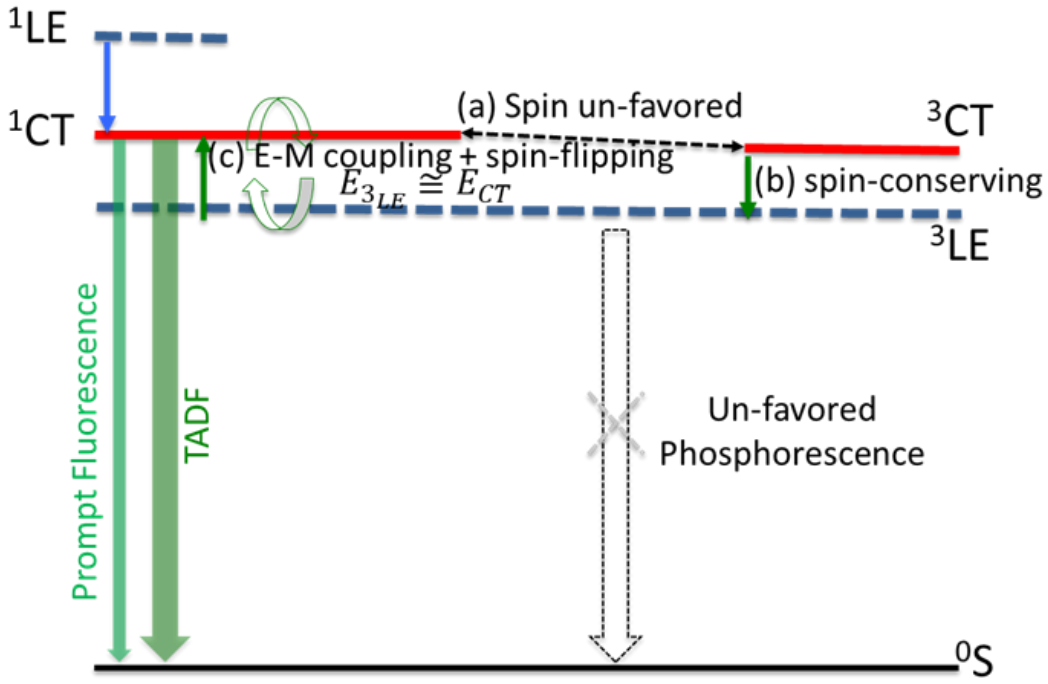

Figure 3-6 The prompt fluorescence by the ^{1}LE-^{1}CT-^{0}S process (blue) and TADF based on the ^{3}LE-^{1}CT-^{0}S process (green), and proposed mechanism for transition between ^{1}CT, ^{3}CT and ^{3}LE states. In order to realize the efficient TADF through ^{3}LE -to-^{1}CT conversion, ^{3}LE state should have similar energy level with CT states ($E_{3_{LE}} \cong E_{CT}$). (a) The intersystem crossing between ^{3}CT to ^{1}CT is un-favored due to intramolecular exchange interaction. (b) Internal conversion from ^{3}CT to ^{3}LE is allowed through spin conservation, (c) Spin mixing from ^{3}LE state to ^{1}CT is critically required to generate TADF through endothermic process due to SOC-induced spin flipping under electric-magnetic (E-M) coupling between ^{1}CT and ^{3}LE. The un-favored exothermic transition from ^{3}LE to S_0 is suppressed by the E-M coupling between ^{3}LE and ^{1}CT to generate a low-efficiency phosphorescence.

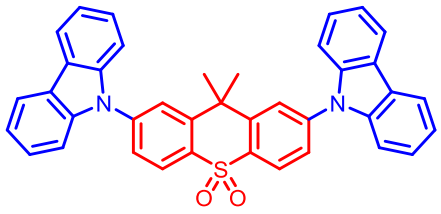

Figure 3-7 Molecular structure of DMTD-Cz.

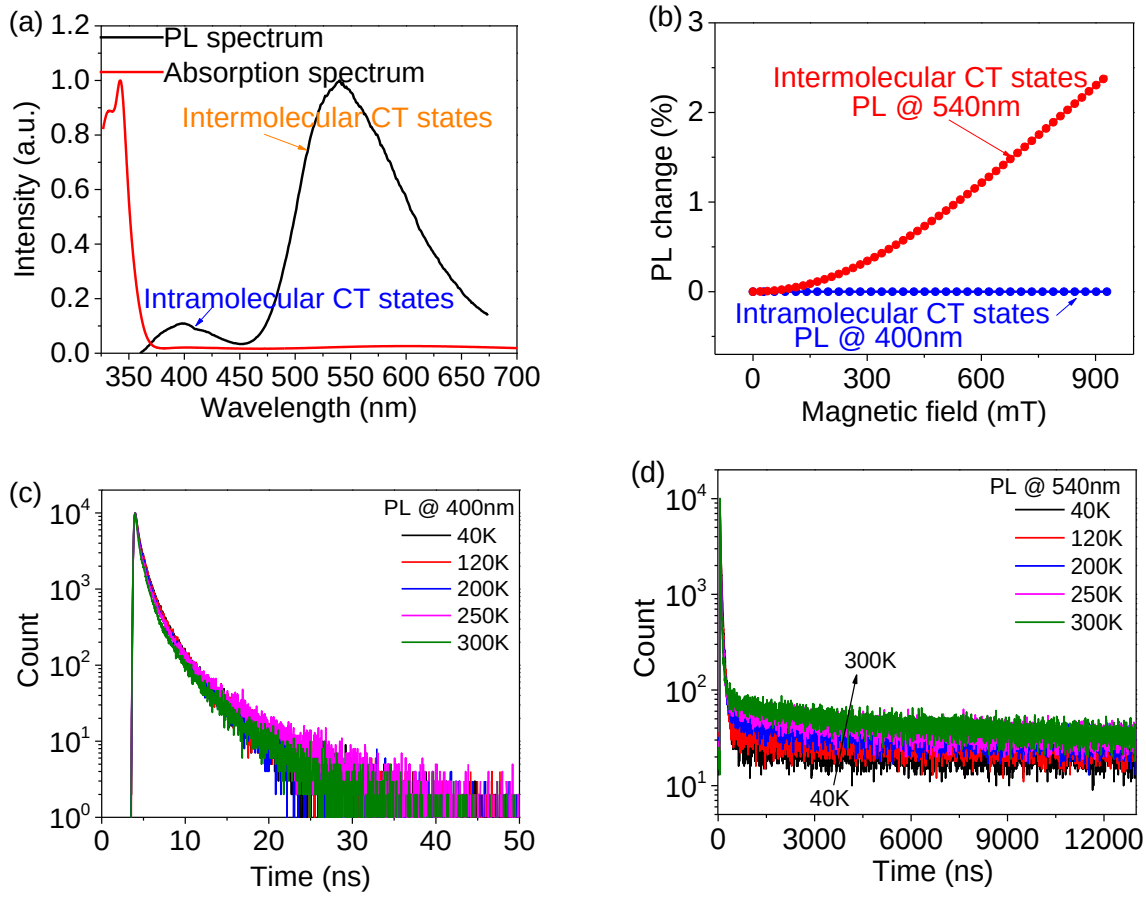

Figure 3-8 (a) PL spectra for the DMTD-Cz molecule with dual emission from both intra- and intermolecular CT states in thin films prepared by thermal evaporation; (b) Positive magneto-PL from intermolecular CT emission and negligible magneto-PL from intramolecular CT emission; (c) PL decay curve of intramolecular CT emission monitored at 400 nm in thin film; (d) PL decay curve of intermolecular CT emission monitored at 540 nm in thin film.

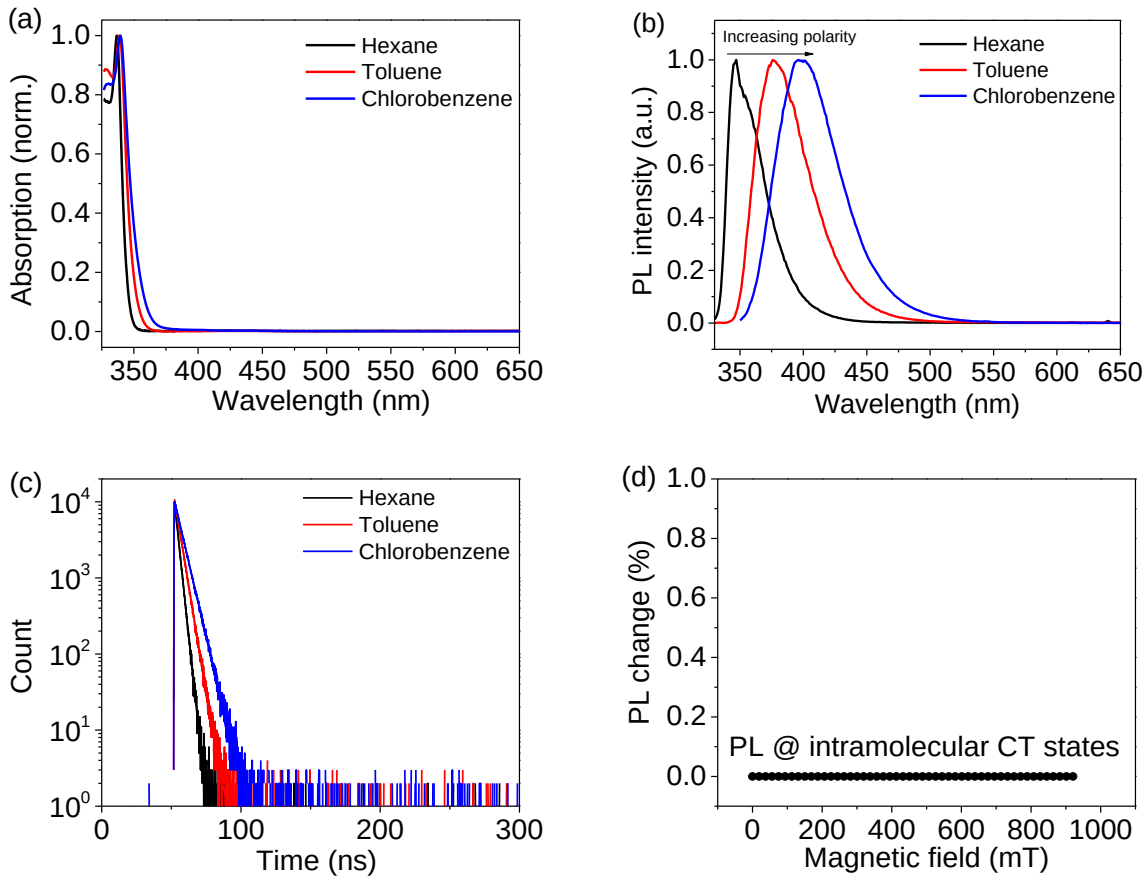

Figure 3-9 (a) absorption spectra, (b) PL spectra and (c) PL lifetime for DMTD-Cz in different solvents: hexane, toluene, and chlorobenzene; (d) negligible magneto-PL can be observed in intramolecular CT states in DMTD-Cz solutions.

Chapter 4 Spin, Energy and Polarization Parameters in Exciplexes with intermolecular charge-transfer states

4.1 Abstract

This chapter explores the spin, energy, and polarization parameters in the light-emitting donor:acceptor exciplex systems with thermally activated delayed fluorescence (TADF) for efficient organic light-emitting diode (OLED) applications. We first compared the two pristine exciplex systems: BCzPh:CN-T2T and BCzPh:B3PYMPM exciplexes. The magneto-PL studies found that the triplet-to-singlet conversion in pristine exciplexes involves spin-orbital coupling (SOC) as the spin-flipping mechanism. The photoinduced electron parametric resonance measurements indicate that the intermolecular charge-transfer occurs with forming electric dipoles ($D^+ \rightarrow A^-$), providing the ionic polarization to generate a SOC in exciplexes. By having different singlet-triplet energy differences (ΔE_{ST}) in BCzPh:CN-T2T (ΔE_{ST}=30meV) and BCzPh:B3PYMPM (ΔE_{ST}=130meV) exciplexes, the SOC generated by the intermolecular charge-transfer states in BCzPh:CN-T2T and BCzPh:B3PYMPM exciplexes shows large and small values (reflected by different internal magnetic parameters: 274mT versus 17mT) with high and low maximum external quantum efficiency (EQE_{max}) values of 21.05% versus 4.89%, respectively. The wavelength-dependent PL studies revealed that, when the electron clouds become more deformed (i.e. stronger polarization) at longer emitting wavelength due to a reduced dipole ($D^{+\delta} \rightarrow A^-$) size, the enhanced SOC and decreased ΔE_{ST} can simultaneously occur to increase the triplet-to-singlet conversion. This confirms the cooperative relationship between spin, energy, and polarization to operate the delayed fluorescence in exciplexes. This part is revised based on the published article [M. Wang, Y. H. Huang, K. S. Lin, T. H. Yeh, J. Duan, T. Y. Ko, S. W. Liu, K. T. Wong, B. Hu, Adv. Mater. 2019, 31, 1904114.]. [82] Furthermore, we further investigated the energy transfer and polarization memory of the transient dipoles of emitting systems based on the exciplex host (BCzPh:CN-T2T) and Ir-complex dopants ($Ir(ppy)_2(acac)$ & $Ir(ppy)_3$). The OLED based on exciplex:$Ir(ppy)_2(acac)$ demonstrates a high maximum external quantum efficiency (EQE_{max}) of 34.01% while the device with exciplex: $Ir(ppy)_3$ gives 27.65 % EQE_{max} with the same device structure. The efficient Förster and Dexter energy transfer channels from exciplex to Ir-

complexes were verified through magneto-optical measurements together with the measurements for the dynamics of singlet and triplet states in the pristine exciplex and the exciplex:Ir-complex systems through the transient absorption. More importantly, with the steady-state and time-resolved PL anisotropy measurements, we have revealed that the $Ir(ppy)_2(acac)$ molecule exhibits much stronger polarization memory of the transient dipoles during the energy transfer process than the $Ir(ppy)_3$ molecules. Thus, the $Ir(ppy)_2(acac)$ molecule can more effectively retain the preferred horizontal dipoles initially formed in the exciplex, consequently enhancing the light-out coupling efficiency of the emitting layer to realize high EQE.

4.2 Introduction

Excited states in organic light-emitting diodes (OLEDs) are inevitably formed with both singlets and triplets under electrical excitation. Singlets and triplets are allowed and forbidden to recombine, respectively, due to spin selection rule. It has been shown that the triplets can be almost 100% converted into singlets in thermally activated delayed fluorescence (TADF) molecules based on the design of chemically combining donor and acceptor moieties to enable intramolecular charge-transfer states.[83] Recently, various TADF molecule based OLEDs with extremely high external quantum efficiency (EQE) exceeding 35% have been successfully demonstrated.[84, 85] Similarly, high EQEs can also be conveniently realized by physically mixing donor and acceptor components to form intermolecular charge-transfer states in exciplex systems, where the non-radiative triplets are also largely converted into radiative singlets. The advantages and versatile applications of exciplex systems for giving high-efficiency OLEDs have been highlighted recently.[86] More significantly, OLEDs with exciplex-forming systems as emitting layer have been reported to achieve EQE higher than 19%,[87-89] manifesting their bright and promising prospects in OLED technology based on physically mixing donor and acceptor molecules. Light-emitting states possess three fundamental parameters: spin, energy, and polarization that essentially govern the triplet-to-singlet conversion. It has been widely demonstrated that a small singlet-triplet energy difference (ΔE_{ST}) is the necessary condition to harvest non-radiative triplets into radiative singlets, providing the basic information on energy parameter effects. Meanwhile, spin-orbital coupling (SOC) has been considered as the key mechanism to flip the spins of triplets, enabling the triplet-to-singlet conversion towards developing delayed fluorescence.[57, 72] Moreover, the preferred

horizontally orientated transient dipoles have been realized in TADF systems to further improve the external quantum efficiency of the devices via improving the light out-coupling efficiency. However, the polarization parameter of the charge-transfer states has been reminded as an un-addressed issue to be related to spin and energy parameters (SOC and ΔE_{ST}). In particular, revealing the relationship between these three fundamental parameters (SOC, ΔE_{ST}, and polarization) can provide critical guidelines to design organic light-emitting materials to harvest non-radiative triplets to radiative singlets for further advancing optoelectronic applications. Furthermore, the pristine exciplex systems generally suffer from the low PL quantum yield (PLQY), which makes device performance of the pristine exciplex-based OLEDs far behind that of the conventional TADF molecules with EQE exceeding 35 %.[84, 90] Therefore, the exciplex host doped with phosphorescent emitters has been developed to largely enhance the device performance. However, the universal criteria to design the high performance exciplex host:phosphorescent dopant systems are still lacking. In particular, we believe revealing the detailed energy transfer process and the polarization dynamics of the transient dipoles can provide critical guidelines to further advancing the optoelectronic applications.

In the first part chapter 4.4.1, we explore the underlying relationship between spin, energy, and polarization parameters based on exciplex systems by using magneto-PL (magneto-PL), photoinduced electron paramagnetic resonance (EPR), and time-resolved PL measurements. Two exciplex systems of BCzPh:CN-T2T and BCzPh:B3PYMPM with high maximum EQE value (EQE_{max}) of 21.05% and low EQE_{max} of 4.89%, respectively, were selected to investigate the relationship between SOC, ΔE_{ST}, and polarization of charge-transfer states towards harvesting non-radiative triplets into radiative singlets. These two exciplex systems, BCzPh:CN-T2T and BCzPh:B3PYMPM, exhibit similar energy level alignments and thus lead to resembling exciplex emissions, yet different ΔE_{ST} values of 30 and 130 meV, respectively. The SOC was studied by magneto-PL *in-situ* measured on exciplex films. The formation of intermolecular charge-transfer dipoles ($D^+ \rightarrow A^-$) was identified by photoinduced EPR characterization. More importantly, by selectively monitoring different PL emission wavelengths, we simultaneously change SOC, ΔE_{ST}, and polarization parameters to study the triplet-to-singlet conversion. Our studies found that

increasing polarization through larger deformation of electron clouds, enhancing SOC, and reducing ΔE_{ST} can concurrently occur, establishing a cooperative relationship of spin, energy, and polarization parameters to maximize the triplet-to-singlet conversion through intermolecular charge-transfer states between donor and acceptor molecules in exciplex systems.

In the second part chapter 4.4.2, the underlying energy transfer process from exciplex host to phosphorescent dopants and the polarization memory of the transient dipoles was explored by using magneto-optical measurements, transient absorption spectroscopy, and PL anisotropy measurements. By using the magneto-optical measurements, we have shown that both Förster and Dexter energy transfer channels are very efficient in these exciplex:Ir-complex systems. Furthermore, we have identified the decay dynamics of singlet and triplet states in the pristine exciplex and the exciplex:Ir-complex systems through transient absorption measurements, which further confirms both the Förster and the Dexter energy transfer processes efficiently occur from exciplex to Ir-complexes. More importantly, by using the steady-state and time-resolved PL anisotropy measurements, we have discovered that the $Ir(ppy)_2(acac)$ exhibits much stronger polarization memory of the transient dipoles during the energy transfer process as compared with that of $Ir(ppy)_3$. The $Ir(ppy)_2(acac)$ molecule can effectively retain the preferred horizontally orientated dipoles in the exciplex, consequently leading to enhanced light out-coupling efficiency for high EQE.

4.3 Experimental Methods

4.3.1 Materials and Devices

The material preparation and device fabrication were conducted by Prof. Shun-Wei Liu's group in Ming Chi University of Technology and Prof. Ken-Tsung Wong's group in National Taiwan University.[82]

4.3.2 Device Characterizations

The current density-voltage-luminance (J-V-L) characteristics and emission spectrum of the proposed devices were measured by a HORIBA Fluorolog-3 spectrometer combined with a source meter (Keithley 2400). The integrated sphere system (SLM-6Z, Isuzu optics) was used to evaluate the EQE value of the OLEDs in ambient condition. The current density-voltage-luminance (J-V-

L), external quantum efficiency (EQE), PL quantum yield (QY), and PL/EL spectrum of the proposed devices were measured by the commercial LQ-100X system from Enli technology, which calibrated with a PR 655 spectrophotometer (Photo Research, USA). For PL QY measurement, all thin-films with 80 nm were deposited on the quartz glass, and then the samples were transferred to a 3.3" PTFE integrating sphere integrating a multi-channel-array spectrometer (Hamamatsu scientific CMOS sensor). The measurement system is calibrated by a NIST traceable standard lamp for the whole spectrum range. In addition, the standard reference sample was produced by the National Institute for Materials Science (NIMS, Japan) for confirming the system's PLQY accuracy. All measurements were carried out in the air. The device characterizations were performed by Prof. Shun-Wei Liu's group and Prof. Ken-Tsung Wong's group.

4.3.3 Optical and magnetic characterizations

The magneto-PL signals were measured by monitoring the PL intensity as a function of magnetic field at room temperature. The photoexcitation for the magneto-PL measurements was from the continuous-wave 375 nm laser beam with the intensity of 70 mW. The magneto-PL amplitude is defined as: $MFE = \frac{I_B - I_0}{I_0}$, where I_B and I_0 are the PL intensities with and without an external magnetic field. The Lorentzian function ($MFE = \alpha \frac{B^2}{B^2 + B_0^2}$) was used to fit the magneto-PL curves, where the B_0 represent the internal magnetic parameter. The PL intensities and spectra were measured by using HORIBA Fluorolog-3 spectrometer. PL decay curves were measured by using the Time Correlated Single Photon Counting System (TCSPC) in HORIBA Fluorolog-3 spectrometer with nanosecond pulsed light excitation from a nanoLED (375 nm). The fitting of PL decay curves was conducted by using the DAS6 fluorescence decay analysis software from HORIBA. The EPR measurements were performed on a Bruker EPR A300 machine (X band).

4.3.4 PL anisotropy

The PL anisotropy measurements were performed by using the Horiba Fluorolog-3 spectrometer with the anisotropy kits. Motor-driven polarizers were used to control the polarization of the excitation and emission light. In real measurements, anisotropy values were calculated using the following equation by taking account of the instrument *G* factor:

$$r = \frac{I_{VV} - G \times I_{VH}}{I_{VV} + 2G \times I_{VH}}$$

where the grating factor, or the G factor, $G = I_{HV}/I_{HH}$ is used to correct for the wavelength-response to polarization of the emission optics and detectors. I_{VV} and I_{VH} are the measured PL intensities with the excitation polarizer vertically oriented and the emission polarizer vertically and horizontally oriented, respectively. In steady-state anisotropy measurements, the 400 nm excitation light was generated by using the Xenon lamp. The NanoLED-405L of 401 nm with the pulse width of 200 ps was used as the excitation source for the time-resolved PL anisotropy measurements.

4.3.5 Picosecond transient absorption

The transient absorption spectra were collected by using a Helios fire spectrometer (Ultrafast Systems LLC). The pump pulses (343 nm) were generated through a harmonic generator (Ultrafast Systems LLC, third harmonic) pumped by one portion of the fundamental beam of a Pharos laser (Light Conversion, 1 kHz, 1030 nm, 290 fs). The other portion of the fundamental beam went through the delay line and then was focused into a sapphire to generate the white light probe. The size of the focused 343 nm pump beam was about 60×60 μm^2 and the pump average power is 10 μW.

4.4 Results and Discussion

4.4.1 Cooperative Relationship between Spin, Energy and Polarization Parameters in High-Efficiency Exciplex Light-Emitting Diodes

Here, we have designed two exciplexes, namely BCzPh:CN-T2T and BCzPh:B3PYMPM (structures shown in **Figure 4-1a**), where BCzPh [91] serves as an electron donor, CN-T2T [92] and B3PYMPM [93] serve as electron acceptors. The BCzPh:CN-T2T and BCzPh:B3PYMPM exciplexes have the similar energy level alignments as shown in **Figure 4-1b**. The characteristics of these two corresponding exciplex OLEDs with the same device structure of ITO/HATCN (10 nm)/TAPC (35 nm)/BCzPh (10 nm)/exciplex-layer (donor:acceptor =1:1; 25 nm)/CN-T2T (40 nm)/LiF (1 nm)/Al (100 nm) are examined. The electroluminescence (EL) spectra of these two devices based on BCzPh:CN-T2T and BCzPh:B3PYMPM exciplexes shown in **Figure 4-1c** indicate that there is no emission from either donor or acceptor. The device based on BCzPh:CN-

T2T exciplex demonstrates a low turn-on voltage of 2.4 V and a maximum luminance (L_{max}) of 10655 cd m^{-2} at 8 V (35.65 mA cm^{-2}) (**Figure 4-1d**). More importantly, the BCzPh:CN-T2T exciplex OLED exhibits the EQE_{max} reaching 21.05 % which still retains a large value of 16.85 % at high luminance of 1000 cd m^{-2} (**Figure 4-1e**). This is the one of the highest performances among all exciplex OLEDs. The high EQE implies that non-radiative triplets have been largely converted into radiative singlets in BCzPh:CN-T2T exciplex OLED. The power dependence of the emission shows slope value close to 1, indicating that the triplet-to-singlet conversion comes from TADF rather than triplet-triplet annihilation (**Figure 4-2**).[94] In sharp contrast, with the same device structure, the BCzPh:B3PYMPM exciplex-based device shows a low EQE_{max} of 4.89% with higher turn-on voltage of 2.5 V and lower L_{max} of 664 cd m^{-2} at 8 V (23.41 mA cm^{-2}). Furthermore, the PL quantum yields (PLQY) of BCzPh:CN-T2T and BCzPh:B3PYMPM blends are measured to be 63.7% and 30.2%, respectively. The PLQY are different by about a factor of 2 in BCzPh:CN-T2T and BCzPh:B3PYMPM exciplexes. But, the EQE values are different by a factor of 4. Therefore, it is obvious that the BCzPh:CN-T2T exciplex undergoes a stronger spin mixing to efficiently harvest the triplets in comparison with BCzPh:B3PYMPM exciplex. However, the underlying factors that lead to such considerable difference between these two blends with similar energy level alignments are unclear. Therefore, it becomes an urgent need to explore the detailed mechanism to operate delayed fluorescence in exciplex states by considering spin, energy and polarization parameters.

Previous studies have concluded that decreasing the ΔE_{ST} can facilitate the spin mixing to convert triplets to singlets. However, the effect of ΔE_{ST} on spin mixing can be validated only if spin flipping mechanism is existed. It is commonly recognized that the SOC can function as the primary mechanism to enable spin flipping towards spin mixing, as exampled in phosphorescent complex with heavy metal.[95, 96] Indeed, SOC as the spin flipping mechanism in D-A type TADF molecules has been recently admitted, [97] in contrast with the early results where HFI is considered as the spin flipping mechanism.[98] However, until now there is still in short of experimental evidence to directly prove the SOC effects in exciplex systems with efficient delayed fluorescence. Now, we use magneto-PL, as an *in-situ* method, to explore the underlying mechanism responsible for the spin mixing in exciplex OLEDs. In general, magneto-PL can occur

when an external magnetic field changes the intersystem crossing through spin flipping mechanism with the consequence of changing the populations on singlet and triplet states.[2] Essentially, an external magnetic field can compete with hyperfine interaction (HFI) or SOC to change the intersystem crossing between singlet and triplet states, leading to a magneto-PL occurring in low (< 10 mT, HFI) [59, 60] and high (> 10 mT, SOC) fields [61, 65], respectively. Therefore, magneto-PL can reveal two critical information in exciplexes: (i) whether spin flipping is occurred and (ii) whether the spin flipping is governed by HFI or SOC. As shown in **Figure 4-3a**, both BCzPh:CN-T2T and BCzPh:B3PYMPM exciplexes exhibit a magneto-PL at high field (> 10 mT). This high-field magneto-PL indicates that there surprisingly exists a SOC in both BCzPh:CN-T2T and BCzPh:B3PYMPM exciplex systems with higher and lower values as shown by the larger and smaller internal magnetic parameters (B_0 = 274 mT versus B_0 = 17 mT). Generally, it has been known that SOC requires a heavy element in organic materials. Because the exciplex systems do not have any heavy element, the SOC revealed by our magneto-PL indicates that there exists a new mechanism to generate an artificial SOC to realize the spin flipping towards harvesting the non-radiate triplets for developing high-efficiency OLEDs. Clearly, a stronger SOC provides a more effective spin flipping to harvest the non-radiative triplets into radiative singlets, providing the necessary condition to develop high-efficiency exciplex OLEDs.

To understand the origin of SOC in exciplexes, we consider that the donor and acceptor molecules become positively and negatively charged ions ($D^{+\square}$ and $A^{-\square}$) through intermolecular charge-transfer process in an exciplex system under photoexcitation, leading to an optically induced dipole $D^{+\square}\rightarrow A^{-\square}$. Before exciting molecules, the D and A molecules have negligible SOC due to isotropic orbital wavefunctions. When optically induced dipole $D^{+\square}\rightarrow A^{-\square}$ is formed with ionic polarization in an exciplex, the isotropic orbitals can be asymmetrically polarized due to Coulombic attraction between $D^{+\square}$and $A^{-\square}$, providing the necessary condition to form a SOC through the interaction between asymmetrically polarized orbitals and spins. Here, the polarization refers to the deformation of electron clouds on $D^{+\square}$ and $A^{-\square}$ within an exciplex in excited state. A larger deformation of electron clouds means a stronger polarization, leading to a higher SOC. Therefore, the photo-induced $D^{+\square}\rightarrow A^{-\square}$ dipoles function as the critical parameter responsible for generating an SOC in exciplexes. Here, the EPR is employed to indicate the charged ions with the

consequence of forming intermolecular charge-transfer states in exciplexes under photoexcitation. As shown in **Figure 4-3b**, both BCzPh:CN-T2T and BCzPh:B3PYMPM films demonstrate a strong EPR signal under photoexcitation, while the dark condition shows a negligible signal. This photoinduced EPR signals provide an evidence to show the formation of optically generated ions within exciplex systems. It is noted that the observation of optically generated ions in our exciplex systems is consistent with the recently observed photoinduced polarons by using transient infrared absorption in a donor:acceptor (CN-Cz2:PO-T2T) exciplex.[99] This result confirms that the charge-transfer between donor and acceptor indeed occurs and consequently leads to the formation of optically induced dipoles ($D^{+\square} \rightarrow A^{-\square}$) towards developing an artificial SOC in exciplex systems.

The SOC enabled by the optically induced dipoles decides whether the spin flipping can occur between singlet and triplet states in exciplexes. As exampled in fluorescent and phosphorescent molecules, the spin flipping becomes forbidden and allowed, regardless of singlet-triplet energy difference, when SOC is absent and present, respectively. In the absence of SOC, when the HFI initiates a low-degree spin flipping, the spin mixing between singlets and triplets can be increased by thermal energy in aromatic molecules.[100] When the SOC is established to allow the spin flipping, the spin mixing between singlets and triplets can be essentially controlled by the ΔE_{ST} to harvest non-radiative triplets into radiative singlets. Empirically, the spin mixing rate (λ) can be simply expressed as $\lambda = H_{SO}/\Delta E_{ST}$, where H_{SO} and ΔE_{ST} are the SOC constant and energy difference between S_1 and T_1 states.[101] Here, we explore the relationship between spin, energy, and polarization parameters by simultaneously changing SOC, ΔE_{ST}, and polarization through detecting the PL from short to long wavelength while monitoring the delayed fluorescence to show triplet-to-singlet conversion. Moving the PL detection from short to long wavelength corresponds to decreasing the donor:acceptor distance, consequently increasing the polarization with enhanced deformation of electron clouds on $D^{+\square}$ and $A^{-\square}$ due to Coulombic attraction. At shorter emitting wavelength (higher energy), the optically induced dipole ($D^{+\square} \rightarrow A^{-\square}$) has a longer separation distance (larger dipole moment), leading to a less deformation of electron clouds on $D^{+\square}$ and $A^{-\square}$ and a weaker SOC. In this situation, the ΔE_{ST} is also large. At a longer emitting wavelength (lower energy), the optically induced dipole ($D^{+\square} \rightarrow A^{-\square}$) has a shorter separation distance (smaller dipole

moment), generating more deformation of electron clouds on $D^{+\square}$ and $A^{-\square}$ and a stronger SOC. In this situation, the ΔE_{ST} becomes smaller. It has been observed that decreasing the donor:acceptor distance leads to a reduced ΔE_{ST} with increased formation of intermolecular charge-transfer states upon moving PL detection from short to long wavelength.[102, 103] Therefore, detecting the PL from short to long wavelength provides a vital method to explore the relationship between spin, energy, and polarization parameters towards harvesting non-radiative triplets into radiative singlets by simultaneously monitoring magneto-PL and time-resolved PL. **Figure 4-4a** shows the PL spectrum of the high-efficiency BCzPh:CN-T2T exciplex system under 375 nm continuous-wave (CW) laser excitation. It is obvious that the magneto-PL line-width for the high-efficiency BCzPh:CN-T2T exciplex system gradually increases as moving the PL detection from short to longer wavelength (**Figure 4-4b**), increasing the internal magnetic parameter B_0 from 214 mT (at shorter PL wavelength of 480 nm) to 312 mT (at longer PL wavelength of 520 nm). The low-efficiency exciplex BCzPh:B3PYMPM system shows a similar phenomenon: the B_0 value increases from 12 mT to 25 mT upon moving the PL detection from short (460 nm) to long (500 nm) wavelength (**Figure 4-4 c** and **d**). Clearly, we can see that decreasing the dipole ($D^{+\square} \rightarrow A^{-\square}$) distance corresponds to the enhanced Coulombic attraction between $D^{+\square}$ and $A^{-\square}$, consequently increasing SOC according to wavelength-dependent magneto-PL. Moreover, we can expect that moving the PL detection from short to long wavelength corresponds to the reduced ΔE_{ST}.[103] Simultaneously, moving the PL detection from short to long wavelength largely increases the delayed fluorescence, as shown in **Figure 4-5**. This serves as the first evidence to show the cooperative relationship between spin, energy, and polarization parameters to maximally harvest non-radiative triplets into radiative singlets towards developing high-efficiency OLEDs through intermolecular charge-transfer states in exciplex systems.

Now we discuss the enhanced horizontal orientation of transition dipoles occurring in exciplex systems. It is well known that, with enhanced horizontal orientation of optical transition dipoles, the light out-coupling can be more efficient to develop high EQEs in OLEDs.[104] Here, the angle-dependent PL measurements shown in **Figure 4-6a** and **b** indicate that the light-emitting states become more horizontally oriented in high-efficiency (BCzPh:CN-T2T) exciplex (Θ = 84%) as compared to low-efficiency (BCzPh:B3PYMPM) exciplex (Θ = 71%). Based on this observation,

we can speculate that stronger charge-transfer characteristics caused by larger difference in electronegativity between donor and acceptor molecules can lead to more horizontally oriented optical transition dipoles in exciplex systems. When co-evaporating D and A molecules on substrate, the D and A molecules can form aggregations to generate donor:acceptor exciplexes. The high Θ value in BCzPh:CN-T2T exciplex system suggests that aggregated D and A molecules can have asymmetric shapes: more preferably on horizontal direction and less preferably on vertical direction due to space-limited vertical aggregation within a thin film. As a consequence, the aggregated D and A molecules have higher probability to form exciplexes in horizontal direction relative to vertical direction in high-efficiency BCzPh:CN-T2T system. The enhanced horizontal orientation of light-emitting states in BCzPh:CN-T2T exciplex system due to stronger intermolecular donor:acceptor interaction can increase the EQE through increased light out-coupling efficiency.

4.4.2 Extended Anisotropy Memory in Exciplex System Doped with Iridium Complexes for high-efficiency light-emitting diodes

We have also designed exciplex host and Ir-complex dopant systems based on our well-established exciplex BCzPh:CN-T2T (**Figure 4-7a)**. The BCzPh:CN-T2T exciplex OLED has demonstrated the maximum EQE of 26.4%,[105] among the highest EQE values in all exciplex based OLEDs. $Ir(ppy)_2(acac)$ and its counterpart $Ir(ppy)_3$ molecules are selected as the phosphorescent dopants with the concentration of 5 %. Both exciplex:$Ir(ppy)_2(acac)$ and exciplex:$Ir(ppy)_3$ systems exhibit high PLQY of 95±2 %. The performances of these two corresponding OLEDs with the same device structure of ITO/HATCN (10 nm)/TAPC (35 nm)/BCzPh (10 nm)/light-emission layer/CN-T2T (40 nm)/LiF (1 nm)/Al (100 nm) were examined. The EL spectra of these two devices are shown in **Figure 4-7b**, indicating the emission comes from phosphorescent dopants. The exciplex:$Ir(ppy)_2(acac)$ based device demonstrates a low turn-on voltage of 2.3 V and a maximum luminance (L_{max}) of 45011 cd m^{-2} at 6 V (39.53 mA cm^{-2}) (**Figure 4-7c**). More importantly, the OLED exhibits the maximum EQE (EQE_{max}) reaching 39.6 % which still retains a large value of 36 % at high luminance of 10000 cd m^{-2} (**Figure 4-7d**). This is the one of the highest performances among all exciplex host doped with phosphorescent emitters OLEDs. In contrast, with the same device structure, the exciplex:$Ir(ppy)_3$ device shows a lower EQE_{max} of 27.9 %. The high EQE

values over 25 % in both the exciplex:Ir-complexes OLEDs indicate the non-radiative loss during the energy transfer from exciplex host to Ir-complex dopants is trivial.

Then the PL and magneto-PL measurements were performed to investigate the energy transfer process between exciplex host and Ir-complexes host. **Figure 4-8a** shows the normalized PL spectra of the pristine exciplex and exciplex:Ir-complex thin films. It can be seen that the PL spectra of the exciplex:Ir-complexes are significantly different from the exciplex host emission. The emissions from exciplex:Ir-complexes are identical with the Ir-complexes. Meanwhile, the PL lifetime of the pristine BCzPh:CN-T2T exciplex shows the typical two exponential decay with prompt and delayed fluorescence components (**Figure 4-8b**). In the phosphorescent emitter doping systems, only one exponential decay can be observed, indicating the light emission comes from the triplets in the phosphorescent dopants. Then we used the magneto-PL to investigate the detailed energy transfer process from exciplex to Ir-complexes. As shown in **Figure 4-8c**, positive magneto-PL can be observed in pristine exciplex thin film samples. Generally, magneto-PL can occur in exciplexes with loosely bounded CT states when an external magnetic field introduces an intersystem crossing through spin flipping mechanism, consequently changing the populations between singlet and triplet states.[2] However, negligible magneto-PL can be observed in phosphorescent emitters due to the strong SOC. Here in exciplex:Ir-complexes systems, magneto-PL becomes absent under the same measurement condition. This indicates that both Foster and Dexter energy transfer process can effectively occur from exciplex to Ir-complexes. If only one energy transfer channel is efficient, appreciable magneto-PL signals should be observed in exciplex:Ir-complexes systems because the magnetic field is able to tune the populations of singlets and triplets in exciplex host, consequently leading to the change on the emission from the phosphorescent dopants through one type of energy transfer. Only when both the energy transfer channels are efficient does the magnetic field dependent spin-mixing in exciplex host have no influence on the PL from the Ir-complexes.

To confirm the energy transfer process, we investigated the dynamics of the excited state in the exciplex and the exciplex:Ir-complex systems through the pump-probe transient absorption. Transient absorption can provide direct observation of both the singlet and triplet excited states to

clarify the detailed behaviors and dynamics in TADF systems.[54, 106] **Figure 4-9 a, b, and c** show the time-resolved transient absorption spectra in the time window up to 6 ns for the pristine exciplex, exciplex:$Ir(ppy)_2(acac)$, and exciplex:$Ir(ppy)_3$ system, respectively, under the same measurement condition. All these three systems display two broad photoinduced absorptions centered at 538 nm and 700 nm after 10 ps upon photoexcitation from the pump beam of 343 nm. Thus, such features are naturally expected to represent the excited states of the exciplex host. Meanwhile, the magnitudes of these two photoinduced absorptions are largely reduced in the exciplex:$Ir(ppy)_2(acac)$ and exciplex:$Ir(ppy)_3$ systems. Moreover, the time profiles at 538 nm show the decreasing trend while the dynamics at 700 nm increase within the 6 ns time window (**Figure 4-9 d** and **4-9e**). The increasing trend of the transient absorption signal time profiles right after time zero is consistent with the time-dependent population of triplets in TADF systems with the efficient intersystem crossing.[107] Therefore, we can attribute the photoinduced absorption features at 538 nm and 700 nm to the singlet and triplet states of the exciplex host, respectively. We can see that the populations of both singlet and triplet states of exciplex drop significantly upon Ir-complexes doping. This confirms the efficient Förster and Dexter energy transfer processes from exciplex host to Ir-complex dopants in the exciplex:Ir-complex systems.

Since both exciplex:Ir-complex systems show efficient energy transfer and similar PLQY, the high EQE of 34.01% obtained from the device with exciplex:$Ir(ppy)_2(acac)$ system indicates that it must exhibit the higher light out-coupling efficiency as compared with that of exciplex:$Ir(ppy)_3$ system. Typically, OLEDs with horizontally aligned transition dipoles have the potential to achieve high EQE without additional out-coupling enhancement layers.[108] Recently, the preferred horizontal dipoles responsible for the enhanced EQEs have been reported in both TADF molecules and exciplex systems. Moreover, the $Ir(ppy)_2(acac)$ molecule was found to exhibit more horizontally oriented dipoles while $Ir(ppy)_3$ molecule is nearly isotropic in thin films.[104, 109, 110] However, in an exciplex-based host:dopant system, the excited states are primarily formed on the exciplex host and then energy transferred to the dopant. The investigations on the polarization dynamics of transient dipoles during the energy transfer process in host:dopant systems are still inadequate. To address this issue, the steady-state and time-resolved PL anisotropy measurements were used in this work to investigate the polarization of transient dipoles during the energy transfer from

exciplex to Ir-complexes. The principle of the PL anisotropy measurements is illustrated in **Figure 4-10**. The thin film sample is excited with the vertically polarized light. The intensity of the emission is measured through a motor-driven polarizer which can control the polarized detection of the emission to be parallel (I_{VV}) or perpendicular (I_{VH}) relative to the excitation light. The PL anisotropy is defined as (see the Methods for details) [81, 111]:

$$r = \frac{I_{VV} - I_{VH}}{I_{VV} + 2I_{VH}}$$

When a population of fluorophores is illuminated by a linearly polarized incident light, those whose transition dipole moments are oriented in a direction close to that of the electric vector of the incident light are preferentially excited, namely, the photoselection effect. Any change in direction of the transition dipole moment during the lifetime of the excited state will decrease the anisotropy of the emission through the depolarization processes such as energy transfer and non-parallel absorption & emission.[112] **Figure 4-11a** shows the steady-state PL anisotropy spectra for the pristine exciplex, exciplex:$Ir(ppy)_2(acac)$, and exciplex:$Ir(ppy)_3$ films under 400 nm photoexcitation. Apparently, the exciplex and exciplex:$Ir(ppy)_3$ films exhibit small PL anisotropy with the anisotropy value of 0.01 at 520 nm around the PL peak position , while the exciplex:$Ir(ppy)_2(acac)$ shows a larger anisotropy value over 0.04. The small anisotropy value of the exciplex indicates that the light-emitting transition dipoles from exciplex are easily depolarized upon polarized photoexcitation at 400 nm. Therefore, it is critically important to keep the polarization of these horizontally oriented transient dipoles during the energy transfer process in the host:dopant systems. Surprisingly, the much higher anisotropy value found in exciplex:$Ir(ppy)_2(acac)$ film indicates that the $Ir(ppy)_2(acac)$ molecules exhibit strong polarization memory, which can largely maintain the polarization of the transient dipoles in exciplex during the energy transfer process. In contrast, the $Ir(ppy)_3$ molecules show weak polarization memory as indicated by the much smaller anisotropy value around 0.01. Note that the polarization memory measurement is independent with the detection angle of the films with different in-plane/out-of-plane transient dipole ratio (**Figure 4-12**). Moreover, the excitation anisotropy spectra shown in **Figure 4-11b** indicate that the PL anisotropy value largely increases when the excitation wavelength is close to the emission wavelength. This indicates that the polarization of the transient dipoles can be depolarized during the hot exciton relaxation process. More importantly, the

exciplex:Ir(ppy)$_2$(acac) system exhibits much larger anisotropy value than the pristine exciplex system with the excitation wavelengths from 360 nm to 450 nm due to the strong polarization memory. This indicates that Ir(ppy)$_2$(acac) can maintain the polarization of the transient dipoles from the exciplex, especially the high energy lying states, through energy transfer. In contrast, the excitation wavelength dependent anisotropy of exciplex:Ir(ppy)$_3$ is overall lower than the pristine exciplex system.

Furthermore, the time-resolved PL anisotropy measurements are used to probe the dynamics of the depolarization process after polarized excitation. The pristine exciplex film shows a rapid anisotropy decay with the lifetime of 27.7 ns and the initial anisotropy value of 0.094 (**Figure 4-11c**). The residual PL anisotropy with the value of 0.022 can be attributed to the preferred horizontally oriented dipole in pristine BCzPh:CN-T2T exciplex. Instead, the exciplex:Ir(ppy)$_2$(acac) sample exhibits much slower anisotropy decay with the average lifetime of 360.4 ns with the much larger initial anisotropy value of 0.162, consistent with the steady-state measurement results (**Figure 4-11d**). On the contrary, the exciplex:Ir(ppy)$_3$ sample shows weaker anisotropy values in dynamic regime with the initial anisotropy value of 0.014 as compared with both pristine exciplex and exciplex:Ir(ppy)$_2$(acac) samples. Clearly, the Ir(ppy)$_2$(acac) molecules can efficiently maintain the polarization of the in-plane transient dipoles in exciplex during the energy transfer as compared with the counterpart molecule Ir(ppy)$_3$. Meanwhile, Ir(ppy)$_2$(acac) molecules have also demonstrated stronger polarization memory than Ir(ppy)$_3$ molecules in CBP host systems, similar with the exciplex host results (**Figure 4-13**). The strong polarization memory observed in Ir(ppy)$_2$(acac) molecules might be due to dipole-dipole interaction from the preferred horizontally orientated molecular packing of Ir(ppy)$_2$(acac), which can reduce the scattering of transient dipoles to cause depolarization. Consequently, the exciplex:Ir(ppy)$_2$(acac) system can take the advantage of both the high horizontally oriented dipole ratio of BCzPh:CN-T2T exciplex and the high PLQY of Ir(ppy)$_2$(acac), leading to the enhanced EQE through the effective light-out coupling in exciplex:Ir(ppy)$_2$(acac)-based OLEDs.

4.5 Conclusion

In summary, our studies firstly revealed the cooperative relationship between spin, energy and polarization parameters to harvest non-radiative triplets into radiative singlets towards developing high-efficiency OLEDs based on two selected exciplex systems (BCzPh:CN-T2T and BCzPh:B3PYMPM). The magneto-PL signal in high field (> 10 mT) provides the direct evidence that high-efficiency BCzPh:CN-T2T and low-efficiency BCzPh:B3PYMPM exciplex systems are formed with high and low SOC values, reflected by largely different internal magnetic parameters (B_0 ~ 274 mT versus B_0 ~ 17 mT). The EPR results indicate that the photoinduced charge-transfer leads to optically generated ions ($D^{+\square}$ and $A^{-\square}$) to form charge-transfer dipoles ($D^{+\square}\rightarrow A^{-\square}$), thus providing the necessary condition to generate a SOC by asymmetrically polarizing orbital wavefunctions in exciplex states. By moving the PL detection from short to long wavelength to probe the charge-transfer dipoles ($D^{+\square}\rightarrow A^{-\square}$) with long and short separation distance, we found that the SOC is increased while the ΔE_{ST} is decreased with the consequence of boosting the delayed fluorescence in exciplex systems. This presents a cooperative relationship between spin, energy and polarization parameters through intermolecular charge-transfer states to operate the triplet-to-singlet conversion towards enhancing delayed fluorescence in exciplex systems. Furthermore, we observed that light-emitting states in high-efficiency BCzPh:CN-T2T exciplex OLED are more horizontally orientated in film plane, increasing light out-coupling efficiency towards high EQE. This indicates that using donor:acceptor exciplex design provides an important approach to increase the horizontal orientation ratio of transition dipoles through space-limited aggregation of donor and acceptor molecules in vertical direction during thin-film formation. The preferred horizontal orientation of transient dipoles can increase the light extraction in exciplex OLEDs. Therefore, our studies show that spin, energy and polarization parameters cooperatively operate the triplet-to-singlet conversion with more horizontally oriented transition dipoles towards increasing delayed fluorescence and EQE, providing a critical guideline to further advance the developments of OLEDs.

By using the well-developed BCzPh:CN-T2T exciplex as the host, we further revealed the detailed excited state behaviors in exciplex hosted Ir-complex systems for efficient OLEDs. The transient absorption spectroscopy provides evidence to indicate the efficient Förster and Dexter energy

transfer channels by directly monitoring the dynamics of the singlet and triplet states in the pristine exciplex and the exciplex:Ir-complex systems. Upon the doping of Ir-complexes, the positive magneto-optical signals observed in pristine exciplex became negligible under the same measurement conditions. This further supports the magnetic field-dependent populations of singlet and triplet in exciplex cannot influence the light emission from Ir-complexes due to the simultaneously efficient Förster and Dexter energy transfer channels. Therefore, the doping of $Ir(ppy)_2(acac)$ and $Ir(ppy)_3$ molecules in BCzPh:CN-T2T exciplex host have demonstrated to achieve the high EQE_{max} values of 34.01% and 27.65%, respectively, with the same device structure and PLQY. More importantly, by using the PL anisotropy measurements, we have found that the $Ir(ppy)_2(acac)$ molecules exhibit much stronger polarization memory as compared with the $Ir(ppy)_3$ molecules, which can maintain the preferred horizontally orientated dipoles (Θ = 84 %) of BCzPh:CN-T2T exciplex host during the energy transfer process. Thus, the BCzPh:CN-T2T exciplex doped with $Ir(ppy)_2(acac)$ system can perfectly take the advantage of both the high ratio of the horizontally orientated dipoles in BCzPh:CN-T2T exciplex and the high PLQY in $Ir(ppy)_2(acac)$ molecules, leading to largely enhanced EQE as compared with exciplex:$Ir(ppy)_3$ system. Clearly, our studies reveal the underlying energy transfer process from exciplex host to phosphorescent dopants as well as the polarization memory of the transient dipoles, providing a critical guideline to further advance the developments of OLEDs.

Appendix

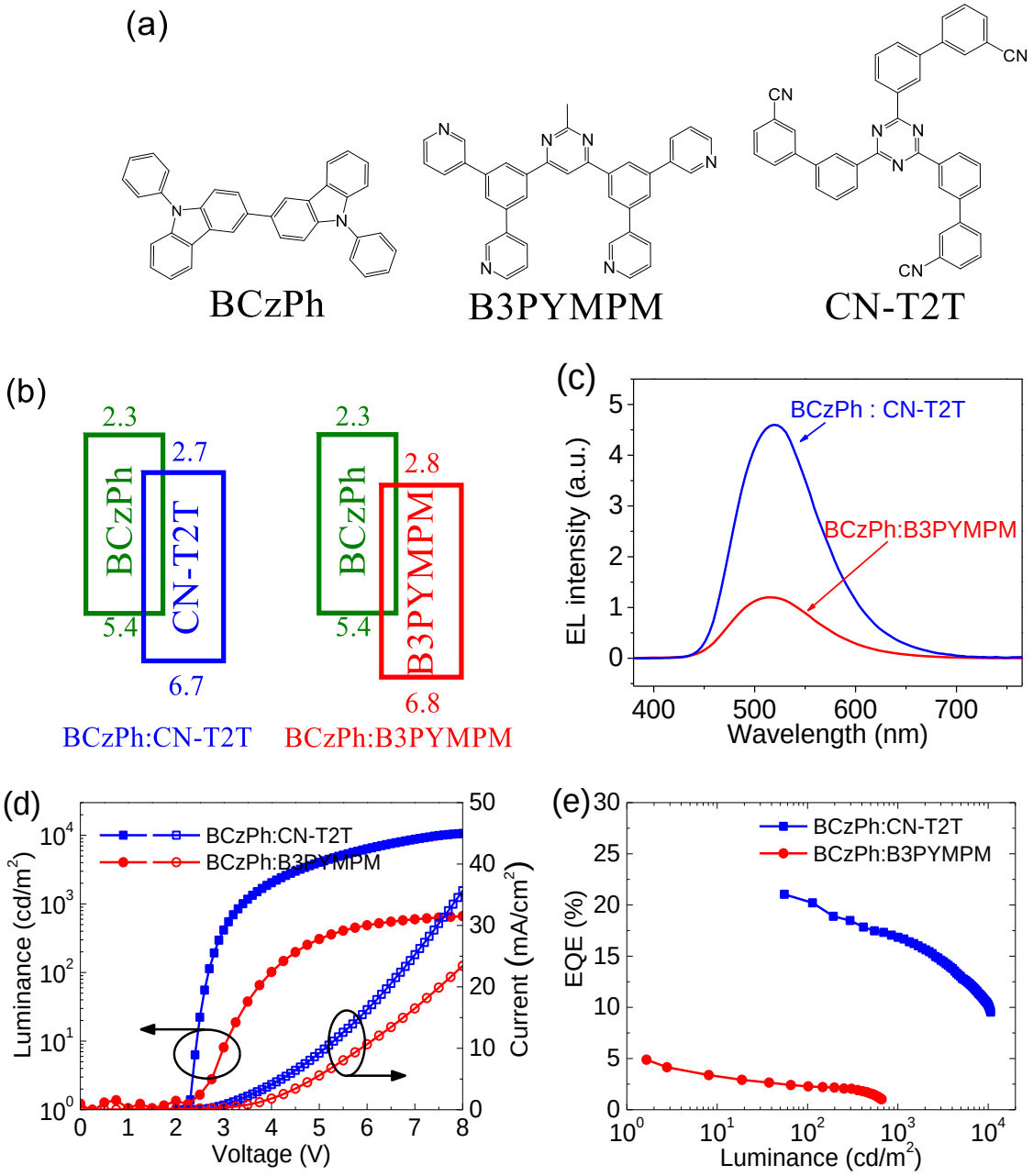

Figure 4-1 Device characterization for BCzPh:CN-T2T and BCzPh:B3PYMPM exciplex OLEDs. (a) Molecular structures of BCzPh, B3PYMPM and CN-T2T; (b) Energy diagram of the exciplexes; (c) EL spectra of the two exciplex OLEDs with the same device structure: ITO/HATCN (10 nm)/TAPC (35 nm)/BCzPh (10 nm)/exciplex layer/ CN-T2T (40 nm)/LiF (1 nm)/Al (100 nm) at 3.5 V bias; (d) Current-Voltage-Luminance characteristics; (e) EQE as the function of luminance.

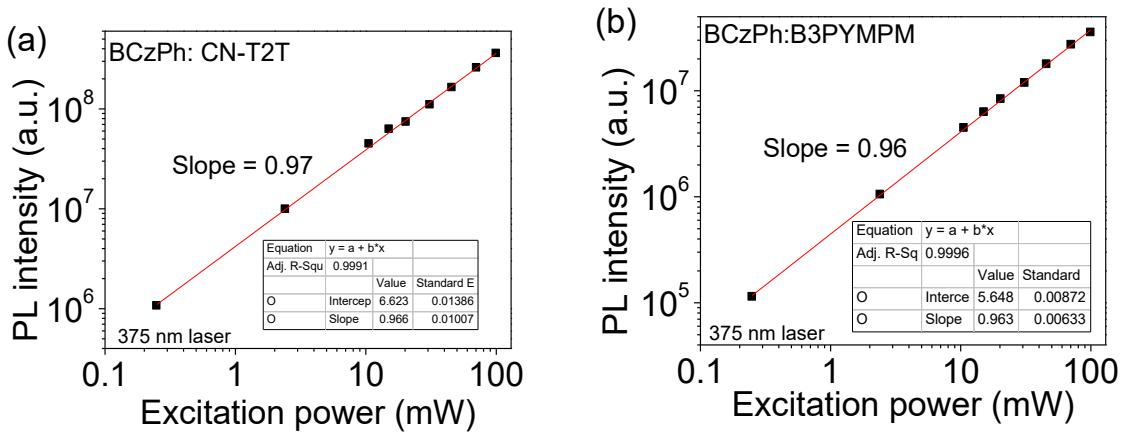

Figure 4-2 PL intensity as the function of excitation intensity for BCzPh:CN-T2T and BCzPh:B3PYMPM exciplex thin films. The slope value close to 1 indicates the TADF behavior rather than triplet-triplet annihilation.

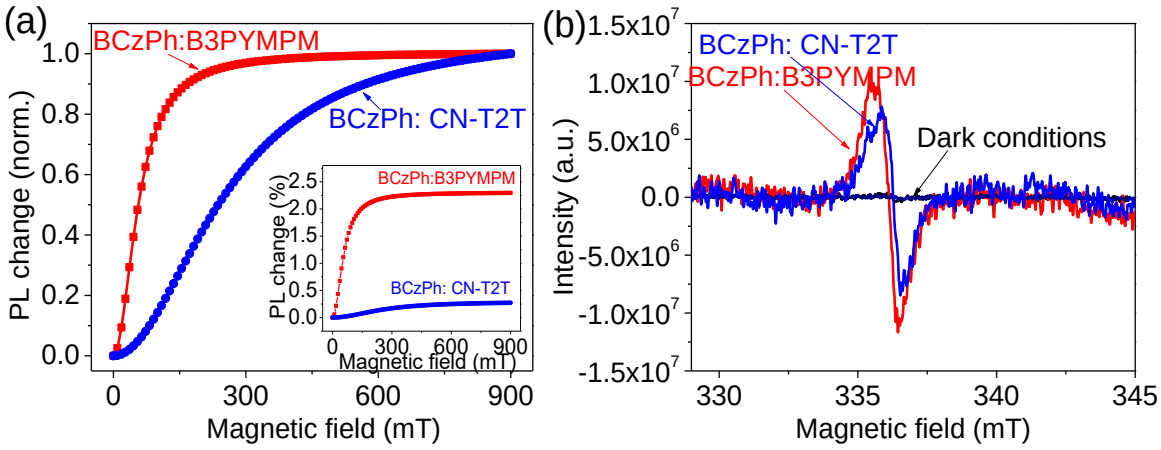

Figure 4-3 (a) Normalized magneto-PL for BCzPh:CN-T2T and BCzPh:B3PYMPM exciplex thin films; The inset shows the original magneto-PL signals. (b) EPR signals for BCzPh:CN-T2T and BCzPh:B3PYMPM exciplex thin films under dark and 405 nm photoexcitation conditions.

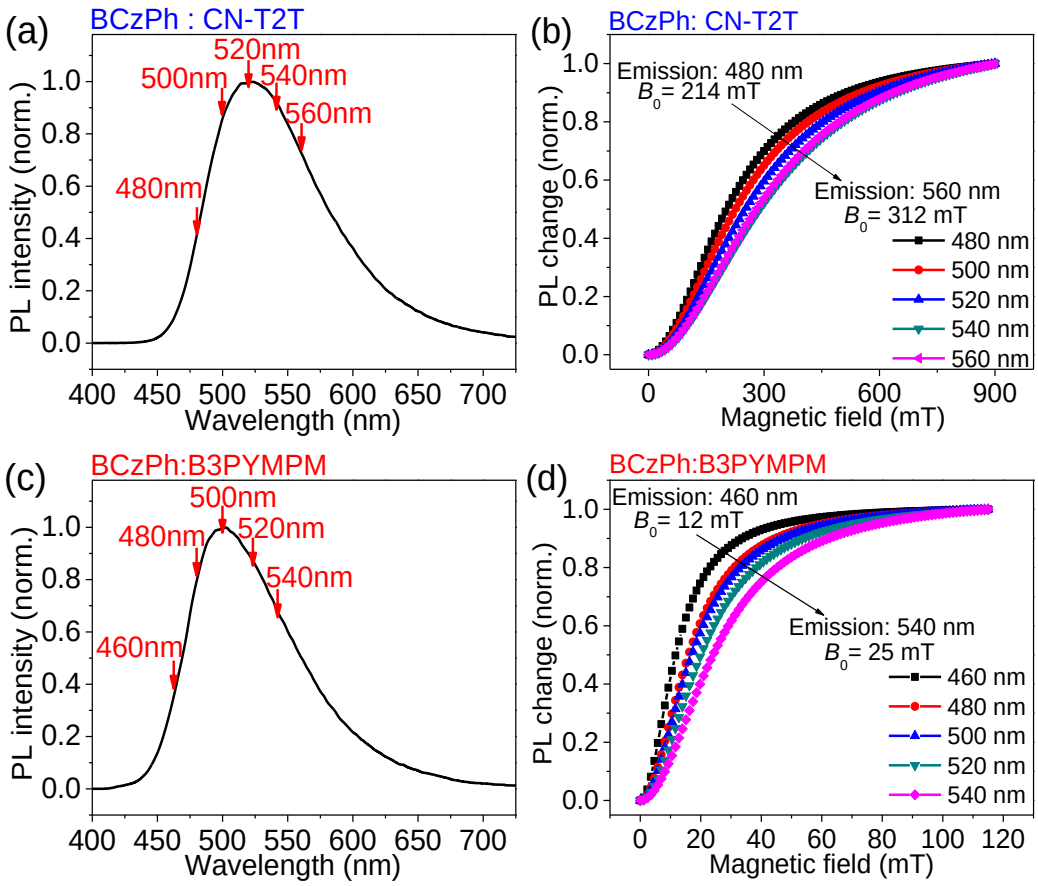

Figure 4-4 PL spectra and emission wavelength dependent magneto-PL. (a) PL spectrum of BCzPh:CN-T2T exciplex; (b) Wavelength dependent magneto-PL of BCzPh:CN-T2T exciplex; (c) PL spectrum of BCzPh:B3PYMPM exciplex; (d) Wavelength dependent magneto-PL of BCzPh:B3PYMPM exciplex.

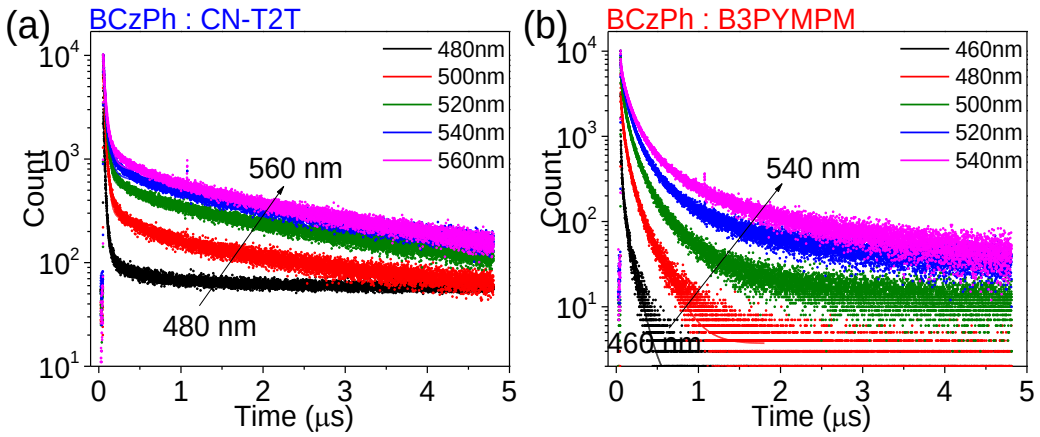

Figure 4-5 Emission wavelength dependent PL decay curves of (a) BCzPh:CN-T2T and (b) BCzPh:B3PYMPM exciplex thin films.

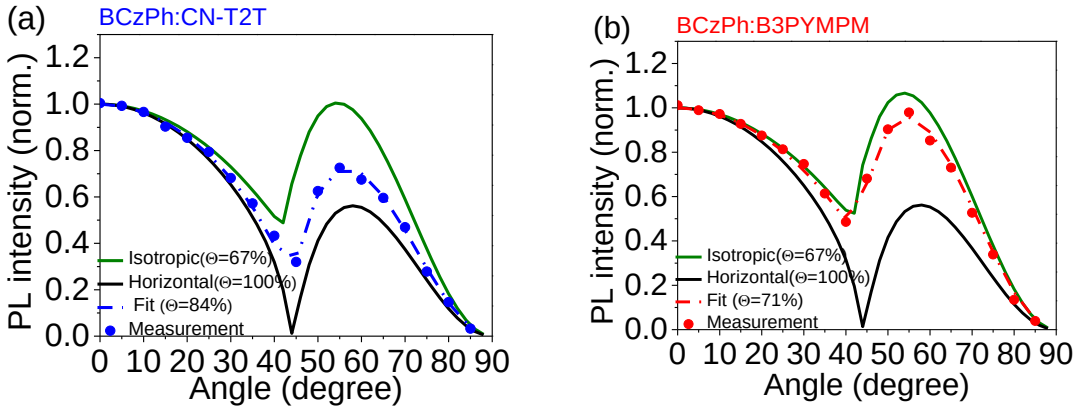

Figure 4-6 Transient dipole direction measurements. The *p*-polarized PL intensity (at PL peak wavelength) of different emitting layers as a function of the emission angle for (a) BCzPh:CN-T2T and (b) BCzPh:B3PYMPM exciplex thin films. The measured curves are compared to simulated curves with different horizontal dipole ratios Θ to extract the horizontal emitting dipole ratios of different emitting layers.

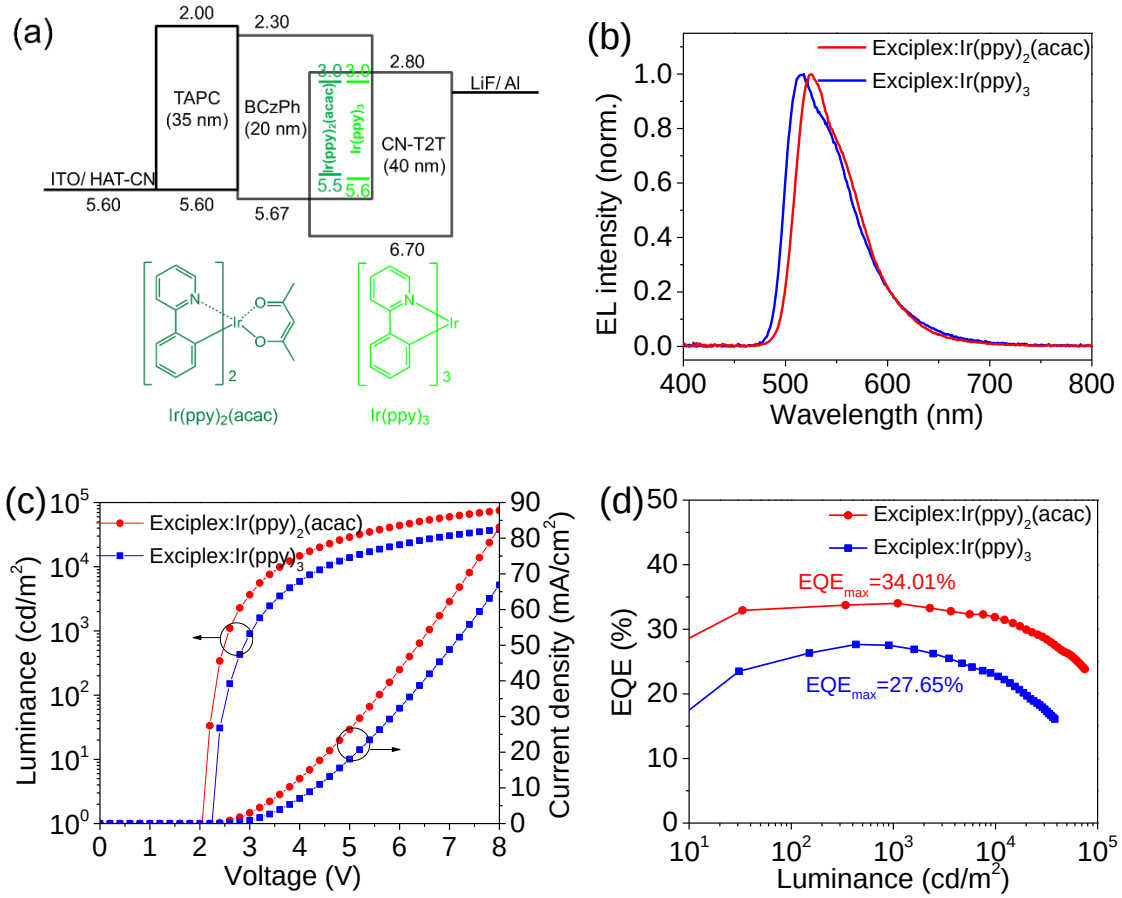

Figure 4-7 Device performance characterizations. (a) the device structure of OLEDs based on the BCzPh:CN-T2T exciplex host doped with Ir-complexes $Ir(ppy)_2(acac)$ and $Ir(ppy)_3$. The molecular structure of the $Ir(ppy)_2(acac)$ and $Ir(ppy)_3$ are also shown. (b) normalized EL spectra of the exciplex:$Ir(ppy)_2(acac)$ and the exciplex: $Ir(ppy)_3$ OLEDs at the luminescence of 1000 cd/m^2; (c) Current-Voltage-Luminance characteristics with the applied voltage up to 8 V; (d) EQE as the function of luminance.

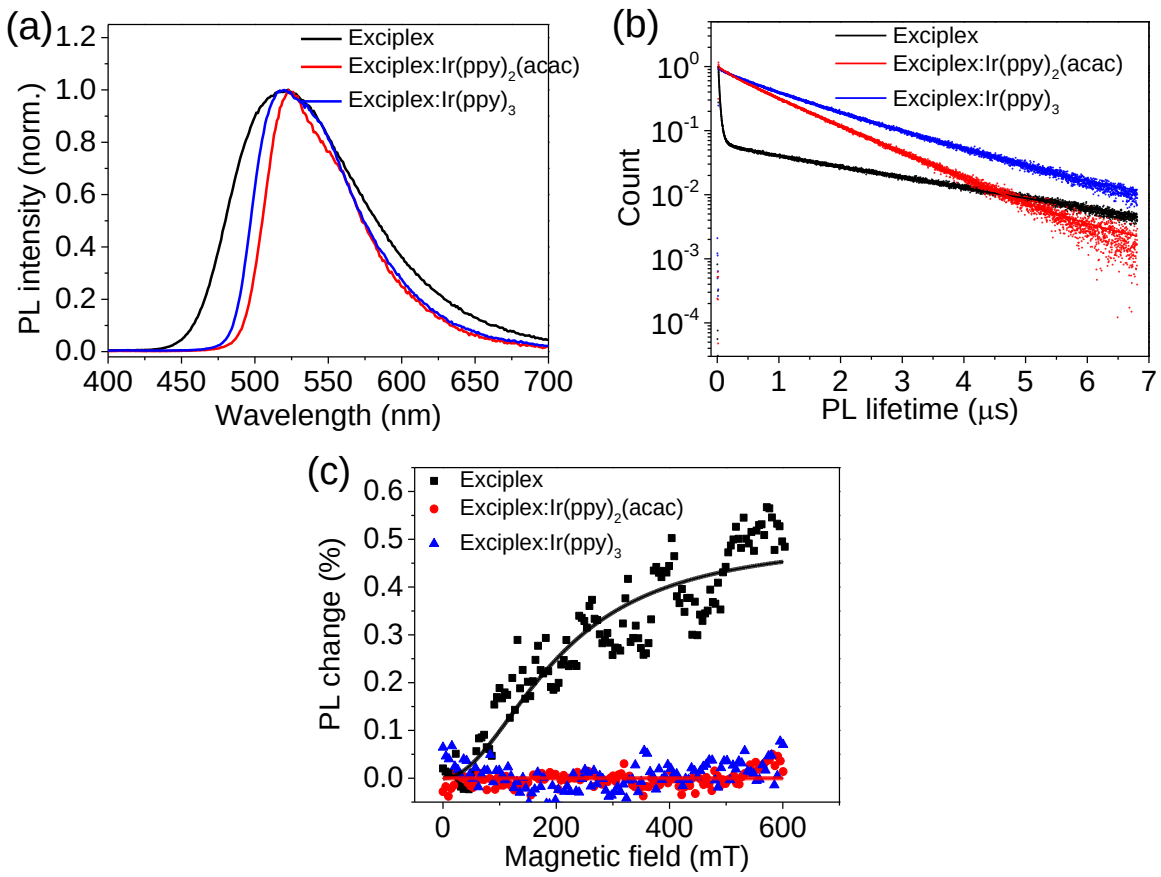

Figure 4-8 (a) PL spectra, (b) PL decay curves, and (c) magneto-PL signals of pristine exciplex and exciplex:Ir-complexes thin film samples.

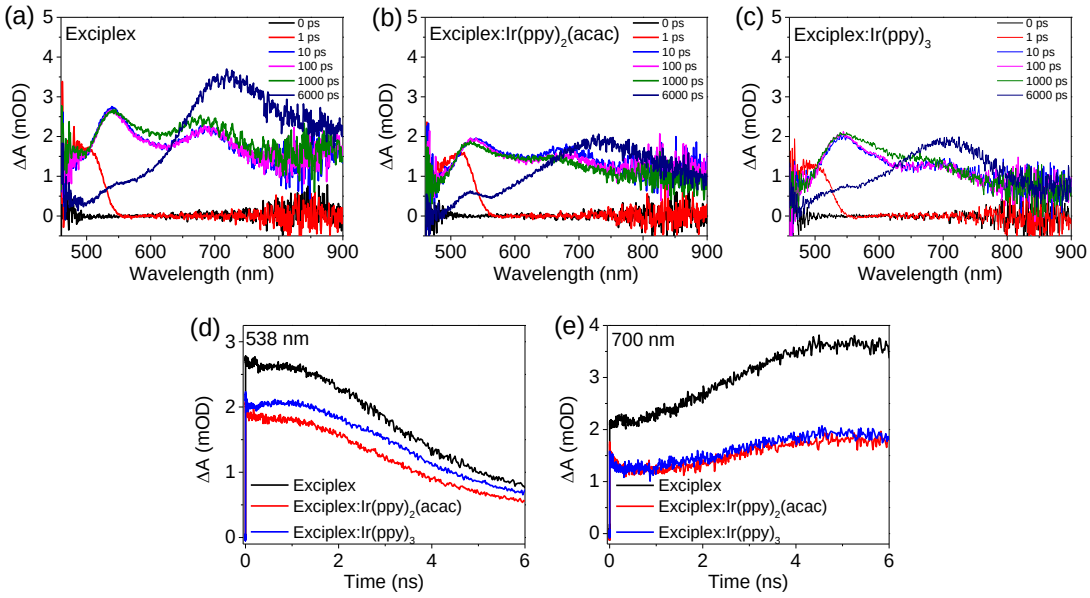

Figure 4-9 Transient absorption measurements. The transient absorption spectra of the (a) pristine exciplex, (b) exciplex:$Ir(ppy)_2(acac)$, and (c) exciplex:$Ir(ppy)_3$ systems with the pump-probe delay time from 0 to 6 ns. The dynamics of the transient absorption signals at (d) 538 nm and (e) 700 nm, corresponding to the singlets and triplets from the exciplex, of the pristine exciplex and exciplex:Ir-complex samples.

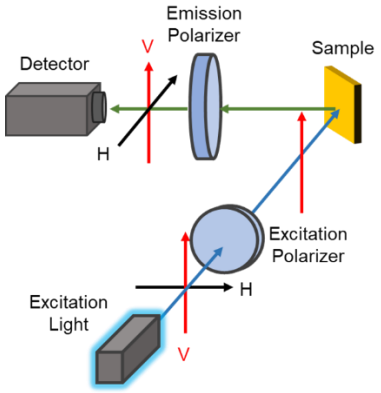

PL anisotropy:

$$r = \frac{I_{VV} - G \times I_{VH}}{I_{VV} + 2G \times I_{VH}}$$

Instrument G factor:

$$G = \frac{I_{HV}}{I_{HH}}$$

Figure 4-10. diagram of the PL anisotropy measurement;

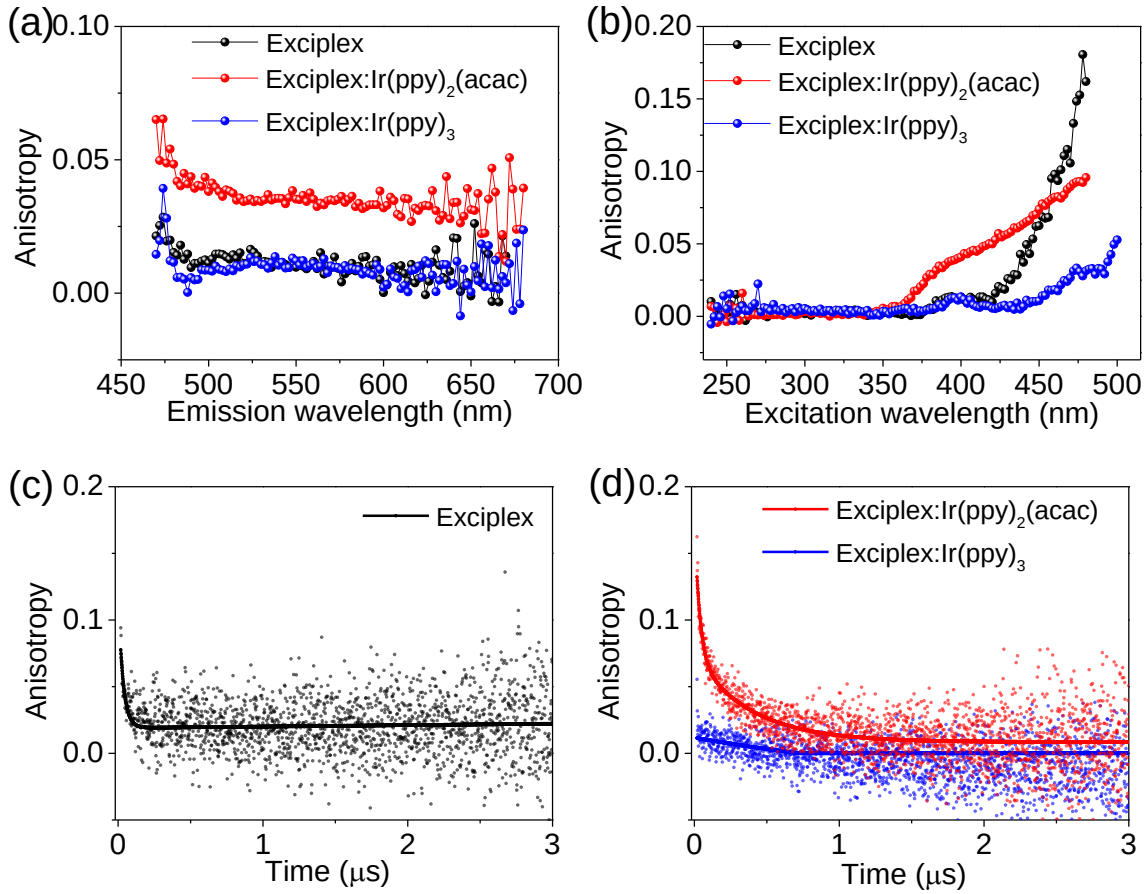

Figure 4-10 Steady state and time-resolved PL anisotropy measurements. (a) steady-state PL anisotropy spectra under the excitation at 400 nm; (b) steady-state PL excitation anisotropy spectra monitored at the PL peak wavelength; (c) time-resolved PL anisotropy of pristine exciplex; (d) time-resolved PL anisotropy of exciplex:$Ir(ppy)_2(acac)$ and exciplex:$Ir(ppy)_3$.

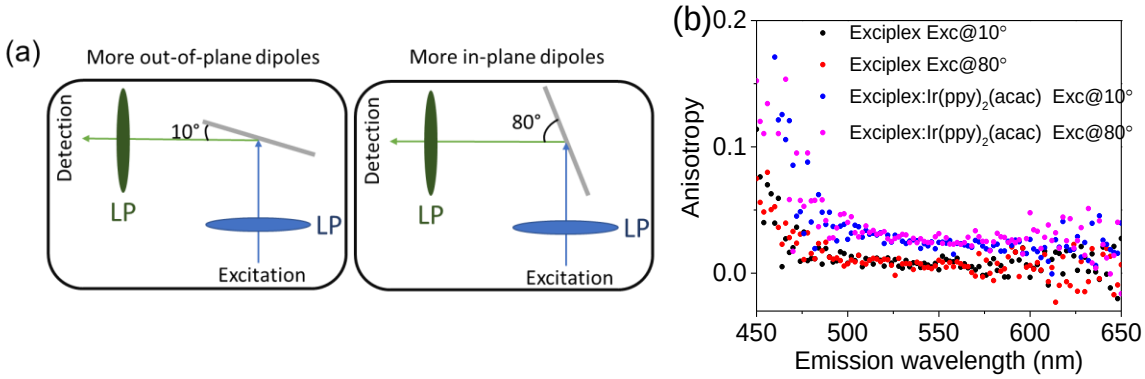

Figure 4-11 Excitation angle dependent PL anisotropy. In the first case (Exc@10°) more out-of-plane dipole can be detected during the PL anisotropy measurements, while in the second case (Exc@80°) more in-plane dipole can detected. It is can be seen that these two measurement conditions show no difference in PL anisotropy for both pristine exciplex and exciplex:$Ir(ppy)_2(acac)$ samples. This indicates that the PL anisotropy measurements here can accurately reflect the polarization memory in PL process.

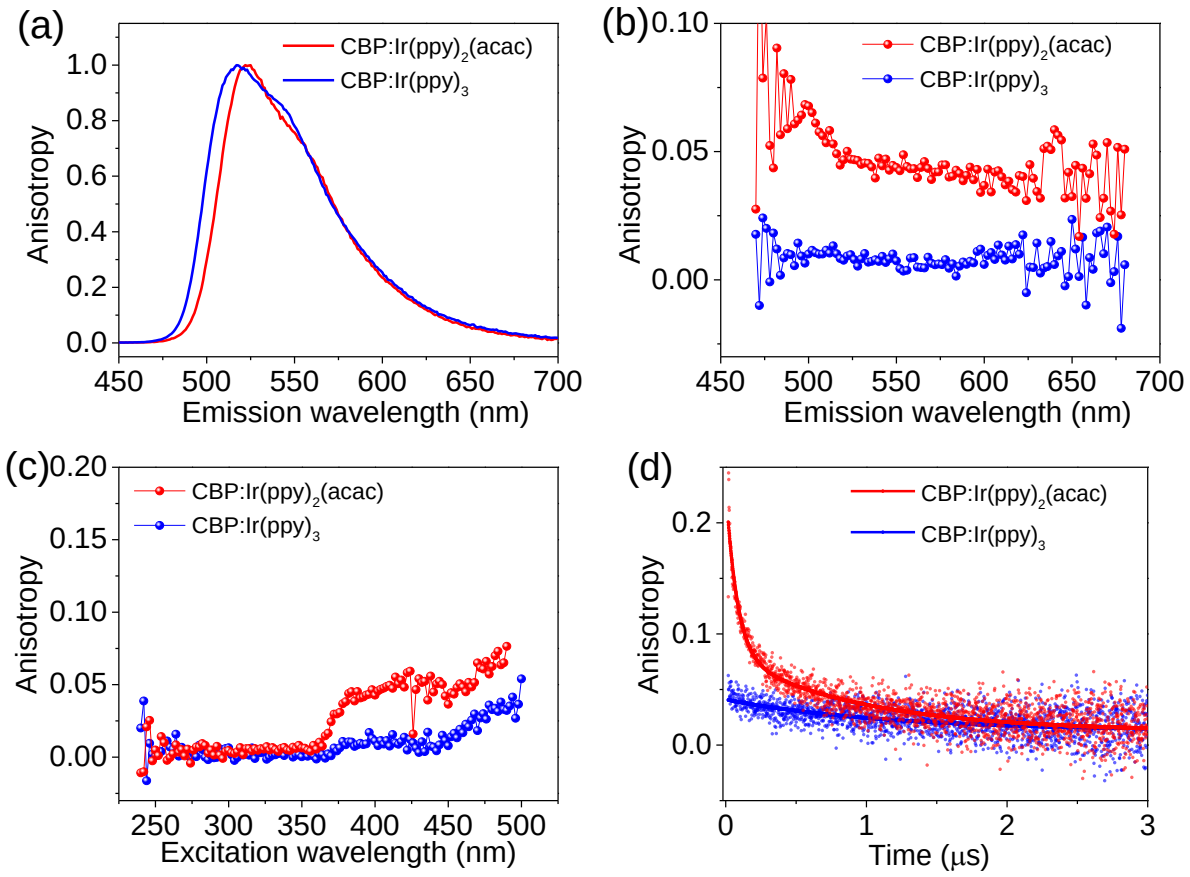

Figure 4-12 (a) PL spectra of the CBP: $Ir(ppy)_2(acac)$ and CBP:$Ir(ppy)_3$ thin film samples; (b) steady-state PL anisotropy spectra under the excitation at 400 nm; (c) steady-state PL excitation anisotropy spectra monitored at the PL peak wavelength; (d) time-resolved PL anisotropy of the CBP: $Ir(ppy)_2(acac)$ and CBP:$Ir(ppy)_3$ systems.

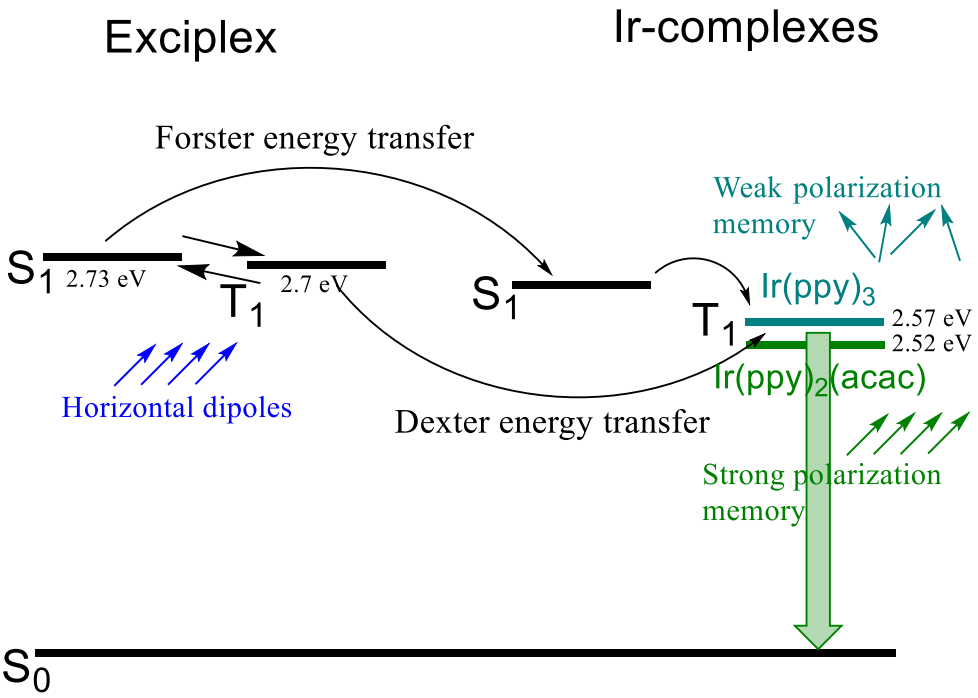

Figure 4-13 Diagram to show the working principle of efficient Dexter and Foster energy transfer from exciplex to Ir-complexes. The $Ir(ppy)_2(acac)$ exhibit strong polarization memory to largely keep the preferred horizontal dipoles in exciplex while the transient dipoles become random in $Ir(ppy)_3$ due to the weak polarization memory.

Chapter 5 Optically induced Magnetization through Photoexcited Spin States at perovskite/ferromagnet interface

5.1 Abstract

Understanding the feasibility to couple semiconducting and magnetic properties in metal halide perovskites through interface design opens new opportunities for creating the next generation spin-related optoelectronics. In this work, we discovered a fundamentally new phenomenon of optically induced magnetization achieved by the coupling of photoexcited orbital magnetic dipoles with magnetic spins at perovskite/ferromagnetic interface. The depth-sensitive polarized neutron reflectometry combined with *in situ* photoexcitation setup, constitutes key evidence of this novel effect. It is demonstrated that a circularly polarized photoexcitation induces a stable magnetization signal within depths up to 7.5 nm into the surface of high-quality perovskite ($MAPbBr_3$) film underneath a ferromagnetic cobalt layer at room temperature. In contrast, a linearly polarized light does not induce any detectable magnetization in the $MAPbBr_3$. The observation reveals that photoexcited orbital magnetic dipoles at the surface of perovskite are coupled with magnetic spins of the ferromagnetic atoms at the interface, leading to an optically induced magnetization within the perovskite's surface. Our finding demonstrates that perovskite semiconductors can be bridged with magnetism through an optically controllable method at room temperature in this heterojunction design, which provides the new concept of utilizing spin and orbital degrees of freedom in new-generation spin-related optoelectronic devices.

5.2 Introduction

The organic-inorganic hybrid perovskites have attracted intense research efforts for developing solution-processed thin-film photovoltaic and light-emitting devices.[113, 114] Recently, the hybrid metal halide perovskites have demonstrated three intriguing phenomena: spin injection,[115-117] electric-magnetic coupling,[66] and optically generated spin states.[25, 118] The success of spin injection provides a precondition to realize the spin-dependent charge transport and excited states in hybrid perovskites by using externally introduced spins even with the presence of strong SOC. Moreover, the observed electric-magnetic coupling at the perovskite/Co interface in dark condition presents fundamental feasibility to couple semiconducting and

magnetic properties through interface design. The optically generated spin states were observed in a variety of hybrid perovskites at room temperature. This shows that when circularly polarized photoexcitation is used to generate excitons with the same-directional orbital magnetic dipoles, the interaction between orbital magnetic dipoles can be established between excitons at the condition that spin polarizations are conserved within exciton lifetime. These phenomena present a fundamental question: do optically photoexcited spin states have sufficiently long lifetime to interact with ferromagnetic surface spin states to generate optically induced magnetization? Photoinduced magnetization was demonstrated in plasmonic nanoparticles via inverse Faraday effect by transferring the angular momentum from the optical field to the electron gas.[119] However, static photoinduced magnetization is generally difficult to realize in conventional semiconductors due to the short spin lifetime as compared with the long carrier lifetime.[120] Recently, a long spin relaxation time of up to ~190 ps was observed in $MAPbBr_3$ at room temperature, and was attributed to the presence of surface Rashba state.[121] Meanwhile, we observed that switching the photoexcitation between linear and circular polarization leads to a change in photoluminescence (PL) intensity, generating a ΔPL phenomenon in perovskites at room temperature.[122] This observation indicates that the orbit–orbit interaction between excitons occurs in the time window of the PL lifetime, thus providing a promising opportunity for developing optically induced magnetization using optically generated spin states that interact with the ferromagnetic surface.

In this chapter, we present experimental evidence of this new phenomenon: the capability to optically induce magnetization by combining photoexcited spin states on the surface of perovskite film and the magnetic dipoles on the ferromagnetic Co interface with perovskite layer. The well-defined $MAPbBr_3$/Co interface was prepared by thermally depositing a Co layer on the surface of the ultra-smooth perovskite layer spin-casted on a Si wafer. The magneto-dielectric measurements demonstrate that the $MAPbBr_3$/Co interface exhibits an electric-magnetic interaction. Notably, by using the depth-sensitive polarized neutron reflectometry (PNR) combined with an *in situ* circularly polarized laser beam (488 nm) excitation, a clear magnetization with a thickness of several nanometers was observed in the $MAPbBr_3$ layer near the $MAPbBr_3$/Co interface. This circularly polarized photoexcitation-induced magnetization disappears under both linearly

polarized photoexcitation, similar to dark condition. Our study demonstrates that circularly polarized orbital magnetic dipoles in hybrid perovskites can be magnetically aligned by the spin dipoles of ferromagnetic Co surface through the hybrid perovskite/ferromagnet interface, functioning as optically induced ferromagnetic states within the hybrid perovskite surface. Thus, in this heterojunction design, perovskite semiconductor can be bridged with magnetism through optically controllable method at room temperature, which provides the new concept of utilizing spin and orbital degrees of freedom in new-generation semiconductor devices, including spin field-effect transistor, ultra-dense non-volatile semiconductor memory, and spin LEDs.[123]

5.3 Experimental Methods

5.3.1 Materials preparation

The perovskite precursor solution was prepared by mixing the Br-based solution and Ac-based solution with the volume ratio of 1:9. The Br-based solution was prepared by dissolving lead(II) bromide ($PbBr_2$, 99.999%, metals basis, Alfa Aesar, 281 mg**)** and methylammonium bromide **(**MABr, 99.999%, 1-Materials, 90 mg**)** into N,N-Dimethylformamide solvent (DMF, anhydrous, 99.8%, Sigma Aldrich, 1 mL). The Ac-based solution was prepared by dissolving MABr (235 mg) and lead (II) acetate trihydrate ($PbAc_2{\cdot}3H_2O$, 99.999%, trace metals basis, Sigma Aldrich, 178 mg) into DMF (1 mL). Both solutions need to be freshly prepared before use. After mixing the two solutions, the obtained perovskite precursor solution was coated onto a precleaned Si wafer substrate (2 cm × 2 cm) via a consecutive two-step spin-casting process at 500 rpm (250 rpm/s) and 8000 rpm (4000 rpm/s) for 7 and 60 s, respectively. The resulting films were then put in a petri dish for 5 min and annealed at 60 °C for 25 min to produce a $MAPbBr_3$ thin film with good crystallization and an ultra-smooth surface over the entire substrate. Next, a 20 nm Co layer and 15 nm Au layer were thermally deposited under a vacuum of 5×10^{-7} Torr with deposition speed of 0.2 Å/s.

5.3.2 Polarized neutron reflectometry

PNR experiments were performed on the Magnetism Reflectometer at the Spallation Neutron Source at Oak Ridge National Laboratory.[124] A neutron beam with a wavelength band of 2.6–8.6 Å with a high polarization of 99 % to 98.5 % was used. Measurements were performed at room temperature with an applied external magnetic field using a Bruker electromagnet with a maximum

magnetic field of 1 T. Using the time-of-flight method, a collimated polychromatic beam of polarized neutrons with the wavelength band $\Delta\lambda$ impinges on the film at a grazing incidence angle θ, where it interacts with atomic nuclei and the spins of unpaired electrons. The reflected intensity is measured as a function of wave vector transfer, $Q = 4\pi\sin(\theta)/\lambda$, for two neutron polarizations $R+$ and $R-$, with the neutron spin parallel (+) or antiparallel (−) to the direction of the external field, H_{ext}. To separate the nuclear from the magnetic scattering, the data are presented as the spin–asymmetry ratio SA = $(R+ - R-)/(R+ + R-)$. A value of SA = 0 designates no magnetic moment in the system. Being electrically neutral, spin-polarized neutrons penetrate the entire multilayer structures and probe magnetic and structural composition of the film through the buried interfaces down to the substrate. A 488 nm continuous-wave semiconductor laser was combined with a linear polarizer (GL10, Thorlabs) and quarter waveplate (AQWP05M-600, Thorlabs) to generate switchable linearly and circularly polarized laser beam excitation with identical intensity of 14 mW/cm^2.

5.3.3 X-ray spectroscopy

X-ray diffraction measurements were conducted on a Panalytical X'pert MPD Pro equipped with an X'Celerator solid-state detector. For the X-ray diffraction measurements, X-rays were generated at 45 kV/40 mA, and the X-ray beam wavelength was λ =1.5418 Å (Cu Kα radiation). XRR data were measured using Panalytical X'pert MRD Pro instrument with a Xe proportional counter. The voltage and current for both X-ray generation were 45 kV and 40 mA, respectively. The measured reflectivity (R) vs. θ curves were converted to R vs. Q, where Q is equivalent to $4\pi\sin(\theta)/\lambda$ with θ being the incidence angle. λ was 1.5406 Å (Cu Kα_1 radiation).

5.3.4 Optical and magnetic characterizations

Absorption spectra were recorded by ultraviolet-visible spectrometer (Lambda 35, from Perkin Elmer). The PL spectra were measured by a fluorescence spectrometer (Horiba Fluorolog-3) under the photoexcitation of 488 nm continuous-wave laser. The magneto-dielectric signals were measured by monitoring the capacitance as a function of the magnetic field strength. The capacitance was recorded by using an Agilent E4980A LCR meter under an alternating electric field with a frequency of 1 kHz. The magneto-dielectric effect is defined as $\mathrm{MFC} = \frac{C_B - C_0}{C_0}$, where C_B and C_0 are the capacitance values in the situation with and without the magnetic field,

respectively. Magnetic hysteresis loop was taken by the Superconducting Quantum Interference Device (SQUID) measurement at room temperature.

5.4 Results and Discussion

5.4.1 Orbital magnetic dipoles photoexcited by circularly polarized light in $MAPbBr_3$ thin films

The polycrystalline $MAPbBr_3$ thin films were prepared using the solution spin-casting method. The absorption and PL spectra are shown in **Figure 5-1a**. A sharp absorption onset is observed at 543 nm and the PL emission peak is located at 537 nm with the full width at half maximum of 21 nm, which represents the typical semiconducting properties of $MAPbBr_3$ thin films. The out-of-plane X-ray diffraction pattern showing sharp (001) and (002) peaks confirms well-ordered crystals of cubic $MAPbBr_3$ with (001) orientation (**Figure 5-1b**). The photoexcited orbital magnetic dipoles were identified in the $MAPbBr_3$ thin film by monitoring PL intensity while switching the photoexcitation between linear and circular polarizations. A circularly polarized photoexcitation generates same-direction orbital magnetic dipoles in excited states before spin relaxation occurs (**Figure 5-2a**). In contrast, a linearly polarized photoexcitation leads to opposite-direction orbital magnetic dipoles. The orbital magnetic dipoles generated by circularly polarized photoexcitation on the hybrid perovskite surface provide the necessary conditions for interaction with magnetic spins on the ferromagnetic surface. **Figure 5-2b** shows the PL intensities measured with linearly and circularly polarized photoexcitations at the same intensity. We see that circular and linear photoexcitations generate lower and higher PL intensities respectively, leading to a ΔPL phenomenon. Here, we should emphasize that, when orbit-orbit interaction occurs before spin relaxation, the same-direction and opposite-direction orbital magnetic dipoles generate stronger and weaker SOC between excited states, leading to increased and reduced efficiency of intersystem crossing from optically generated bright states to dark states with higher and lower PL intensities, respectively. This causes a ΔPL phenomenon upon switching photoexcitation between linear and circular polarizations when photoexcited orbital magnetic dipoles establish a mutual interaction within PL lifetime. Therefore, the ΔPL phenomenon provides a convenient method to identify whether orbital magnetic dipoles can develop a mutual interaction before spin relaxation in hybrid perovskites.

5.4.2 Perovskite/ferromagnetic interfacial coupling towards optically induced magnetization

To investigate the perovskite/ferromagnetic interface, we engineered a double-layered heterostructure by depositing a 20 nm Co layer on top of the $MAPbBr_3$ perovskite layer using the thermal evaporation method. Then the 15 nm Au layer was subsequently grown to protect the Co layer from oxidation. The 20 nm Co layer forms a continuous polycrystalline film with typical ferromagnetic properties. The $MAPbBr_3$/Co/Au sample shows a clear magnetic hysteresis loop in the in-plane direction, as shown in **Figure 5-2c**. Here, we used the magneto-dielectric measurement to investigate the $MAPbBr_3$/Co interface. **Figure 5-2d** illustrates that the capacitance signal measured at a frequency of 1 kHz gradually decreases with the increased applied magnetic field, leading to a magneto-dielectric signal from the $MAPbBr_3$/Co interface. In contrast, when the Co layer is absent ($MAPbBr_3$–only device), the negligible magneto-dielectric signal was detected. The observed magneto-dielectric signal in the $MAPbBr_3$/Co sample originates from the electric-magnetic coupling between the spins of the ferromagnetic Co atoms and electric polarization at the perovskite surface.[66]

The electric-magnetic coupling at the $MAPbBr_3$/Co interface raises an important question about whether the ferromagnetic Co layer can magnetically interact with photoexcited orbital magnetic dipoles in the perovskite layer, introducing optically induced magnetization on the $MAPbBr_3$ surface. To explore optically induced magnetism at the $MAPbBr_3$/Co interface, we used the PNR technique combined the experimental setup for *in situ* photoexcitation. The X-ray reflectivity (XRR) curve of the $MAPbBr_3$/Co/Au sample indicates the well-controlled interfacial roughness around 1 nm over the whole sample (2 cm × 2 cm), which is suitable for reflectometry measurements (**Figure 5-3**). The fit parameters are shown in **Table 5-1**. PNR is a highly penetrating depth-sensitive technique to probe the chemical and magnetic depth profiles with a resolution of 0.5 nm. The depth profiles of the nuclear and magnetic scattering length densities (NSLD and MSLD) correspond to the depth profile of the chemical and in-plane magnetization vector distributions on the atomic scale, respectively.[125-127] Based on these neutron scattering merits, PNR serves as the powerful technique to simultaneously and nondestructively characterize chemical and magnetic nature of buried interfaces.[128] Magnetism arises from the strong short-range correlation between electronic spin and orbital degree of freedom, which can be inherently

altered at interfaces, particularly in the presence of strong SOC and external stimuli.[129] Upon *in situ* photoexcitation during the PNR measurements (**Figure 5-4a**), the change of magnetization properties at $MAPbBr_3$/Co interface can be detected by monitoring the MSLD depth profile. Here, the PNR measurements were completed first on the Si/$MAPbBr_3$/Co/Au sample (N1) at room temperature, and in-plane applied magnetic field of 1 T. The neutron reflectivity plots of R^+ and R^-, where the superscript plus (or minus) signs indicate neutrons with spin parallel (or antiparallel) to the direction of the applied magnetic field, are shown in **Figure 5-4b** as a function of the wave vector transfer $Q = 4\pi\sin(\theta_i/\lambda)$, where θ_i is the incident angle and λ is the neutron wavelength. The chemical profile (NSLD) and the magnetic profile (MSLD) are obtained from a simultaneous fit of the PNR data (**Figure 5-4c**) and are plotted as functions of the distance from the sample surface. By closely comparing the $MSLD_{dark}$ with the NSLD in **Figure 5-4c**, we can see that in dark condition, the magnetism is concentrated solely in the ferromagnetic Co layer. However, when under circularly polarized 488 nm continuous-wave laser beam photoexcites orbital magnetic dipoles to generate spin-polarized excited states, the difference between R^+ and R^- curves becomes larger in the high Q range from 0. 8 to 1.2 nm^{-1}, compared to dark condition measurements, indicating the appearance of interfacial magnetization induced by circularly polarized photoexcitation within the perovskite layer near the perovskite/ferromagnetic interface. The corresponding spin asymmetry of the circularly polarized photoexcitation condition also shows a larger value in the high Q range compared to the dark condition, representing the enhanced magnetization within the perovskite interface (**Figure 5-4d**). Indeed, the corresponding $MSLD_{circular}$ depth profile shows that the magnetization reaches into the perovskite layer approximately 5 nm at the $MAPbBr_3$/Co interface under circularly polarized laser excitation. Note, this additional magnetization does not come from the Co atoms because the NSLD profile indicates the pristine $MAPbBr_3$ component in the same depth regime, which was confirmed using XRR.

To confirm the observed photoinduced magnetization at the $MAPbBr_3$/Co interface, we performed a detailed study on a second Si/$MAPbBr_3$/Co/Au sample (N2) with a similar structure to explore magnetization under dark, circularly and linearly polarized photoexcitation (**Figure 5-5a**). **Figure 5-5b** depicts the chemical (NSLD) and magnetization (MSLD) profiles for dark, linear, and circular laser polarizations at the perovskite/Co interfacial region. It can be seen that no

magnetization was detected in the $MAPbBr_3$ layer at the $MAPbBr_3$/Co interface in dark condition. However, when the circularly polarized 488 nm laser beam excited the $MAPbBr_3$, we observed that magnetization formed in $MAPbBr_3$ layer with the thickness of 7.5 nm at $MAPbBr_3$/Co interface. This is consistent with the experimental results observed in sample N1. In contrast, when switching the photoexcitation to a linearly polarized laser beam, the interfacial magnetization is significantly reduced to a negligible value within the sensitivity of the method. These results suggest that the observed interface magnetization is not merely an excited state effect. The orbital magnetic dipoles in spin-polarized states generated by circular photoexcitation are likely the origin of the observed photoinduced interface magnetization. The spin asymmetry plots in **Figure 5-5c** show that the circularly polarized photoexcitation condition yields a larger spin asymmetry value in the region of wavevector transfer ($0.8\ nm^{-1} < Q < 1.2\ nm^{-1}$), which corresponds to the length scale of about 6–8 nm, and the fit to the data shows that it comes from the interface magnetization. From the fit to the data, we obtained detailed quantitative information on the magnetization induced in the perovskite interfacial layer. The next to Co perovskite layer (sublayer 1) is 6.8 +/- 0.5 nm wide with an MSLD = 3.4 +/- 1 $x10^{-5}$ nm^{-2}, which corresponds to 117 +/- 30 emu/cc. The next layer, sublayer 2, is about 0.7 +/- 0.5 nm wide with an MSLD = 1.5 +/- 1 $x10^{-5}$ nm^{-2}, which corresponds to 51.7 +/- 30 emu/cc. The magnetization of the Co layer has a maximum MSLD Co =3.34 +/- 0.1 $x10^{-4}$ nm^{-2}, corresponding to 1151.7 +/- 30 emu/cc.

Clearly, circularly polarized photoexcitation can introduce a magnetization at the $MAPbBr_3$/Co interface, representing a promising method to realize magnetized excited states through the coupling between the orbital magnetic dipoles of perovskite and the spin dipoles of ferromagnetic surface. The observed ΔPL phenomenon provides evidence that the orbital magnetic dipoles can conserve their spin polarizations within the lifetime of excited states, providing the necessary condition to interact with the spin dipoles of ferromagnetic surface toward developing optically induced magnetization. **Figure 5-6a** illustrates the principle of optically induced magnetization by directly coupling the orbital magnetic dipoles of circularly polarized excited states on a hybrid perovskite surface with the magnetic spins on the ferromagnetic Co surface. The coupling between orbital magnetic dipoles of excited states generated by circular photoexcitation and magnetic spins of Co is an underlying mechanism behind of an optically induced magnetization through the

perovskite/ferromagnetic interface. To further confirm the mechanism, we measured the off-specular scattering with polarized neutrons under the same experimental conditions with *in situ* circularly polarized, linearly polarized photoexcitations, and under dark conditions. The magnetic off-specular scattering has a spin-flip origin [130] and is sensitive to the lateral fluctuations of the magnetic moments.[131, 132] If the orbital magnetic dipoles of excited states generated by polarized photoexcitation are coupled with the magnetic spins at perovskite/ferromagnetic interfaces as shown in the scheme in **Figure 5-6a**, then the neutron spins can undergo spin-flip scattering on the in-plane component of the magnetic dipoles perpendicular to the neutron spin, [133, 134] and this scattering can appear as an additional intensity in the two-dimensional (2D) intensity maps. The results of off-specular scattering measurement for the three experimental conditions with circularly polarized, linearly polarized photoexcitation, and dark conditions are presented in **Figure 5-6b** as a 2D intensity map in the coordinates $p_i - p_f$ and $p_i + p_f$ (p_i and p_f are shown in the inset and are the components of the neutron wavevectors perpendicular to the sample surface). The $Q = p_i + p_f$ is the wave vector transfer perpendicular to the surface, so the structure of the multilayer along this direction is probed. The intensity of the specular line as a function of $p_i + p_f$ at $p_i - p_f = 0$ reflects the features described in the following. The total reflection region at low momentum transfer $p_i + p_f$ is followed by thickness oscillations originating from the layered structure of the sample. The off-specular scattering in **Figure 5-6b** appears as intensity bands perpendicular to the reflectivity line and crossing it at the thickness oscillation positions. The off-specular scattering measured in the sample in circular polarization conditions show a strong scattering at $0.8\ nm^{-1} < Q < 1.2\ nm^{-1}$ (marked with the dashed box), which is absent in two other 2D maps measured in linear polarization and dark conditions. This intensity originates from the spin-flip scattering of neutron spins on magnetic dipoles shown schematically in **Figure 5-6a**.

5.5 Conclusion

In conclusion, we have presented experimental evidence of optically induced magnetization at perovskite/ferromagnet ($MAPbBr_3$/Co) interface under photoexcitation by using the depth-sensitive PNR method at room temperature. We found that an optically induced magnetization can be observed with thicknesses up to ~7.5 nm into $MAPbBr_3$ layer in the presence of ferromagnetic Co when orbital magnetic dipoles are generated in the same direction under a circularly polarized

photoexcitation. In contrast, no optically induced magnetization can be detected within the perovskite surface in the $MAPbBr_3$/Co sample when the orbital magnetic dipoles are generated with opposite directions under a linearly polarized photoexcitation. This indicates that circularly polarized light-generated spin states in the perovskite layer can directly interact with ferromagnet Co through electric-magnetic coupling, leading to an optically induced magnetization. These studies represent an exciting discovery of the photoinduced room-temperature ferromagnetism in metal halide perovskite in heterostructure design and have far-reaching consequences, as it paves the way for the realization of new ferromagnetically tunable semiconductor materials through optical method for next-generation spin-related optoelectronics.

Appendix

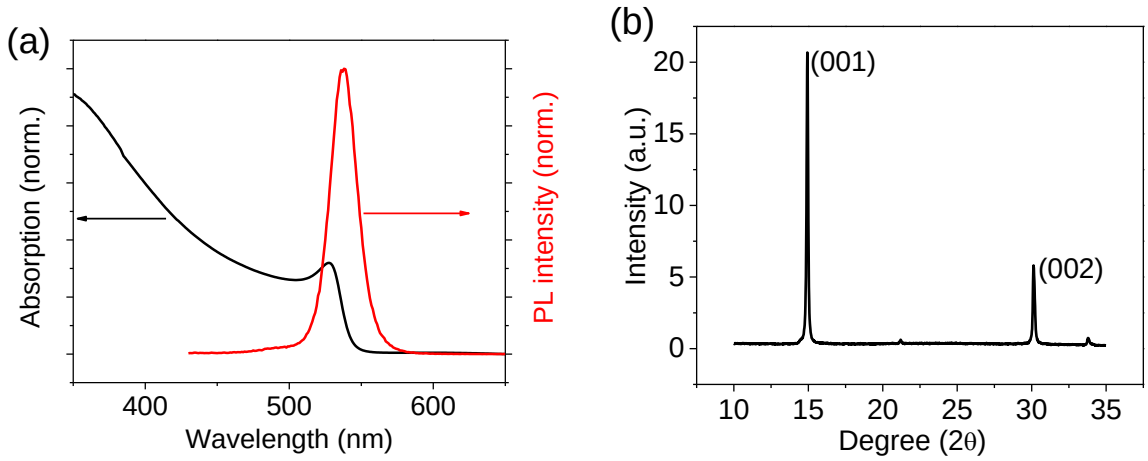

Figure 5-1 (a), Absorption and PL spectra of the $MAPbBr_3$ thin film. (b), Out-of-plane θ-2θ X-ray diffraction scan for $MAPbBr_3$ thin film.

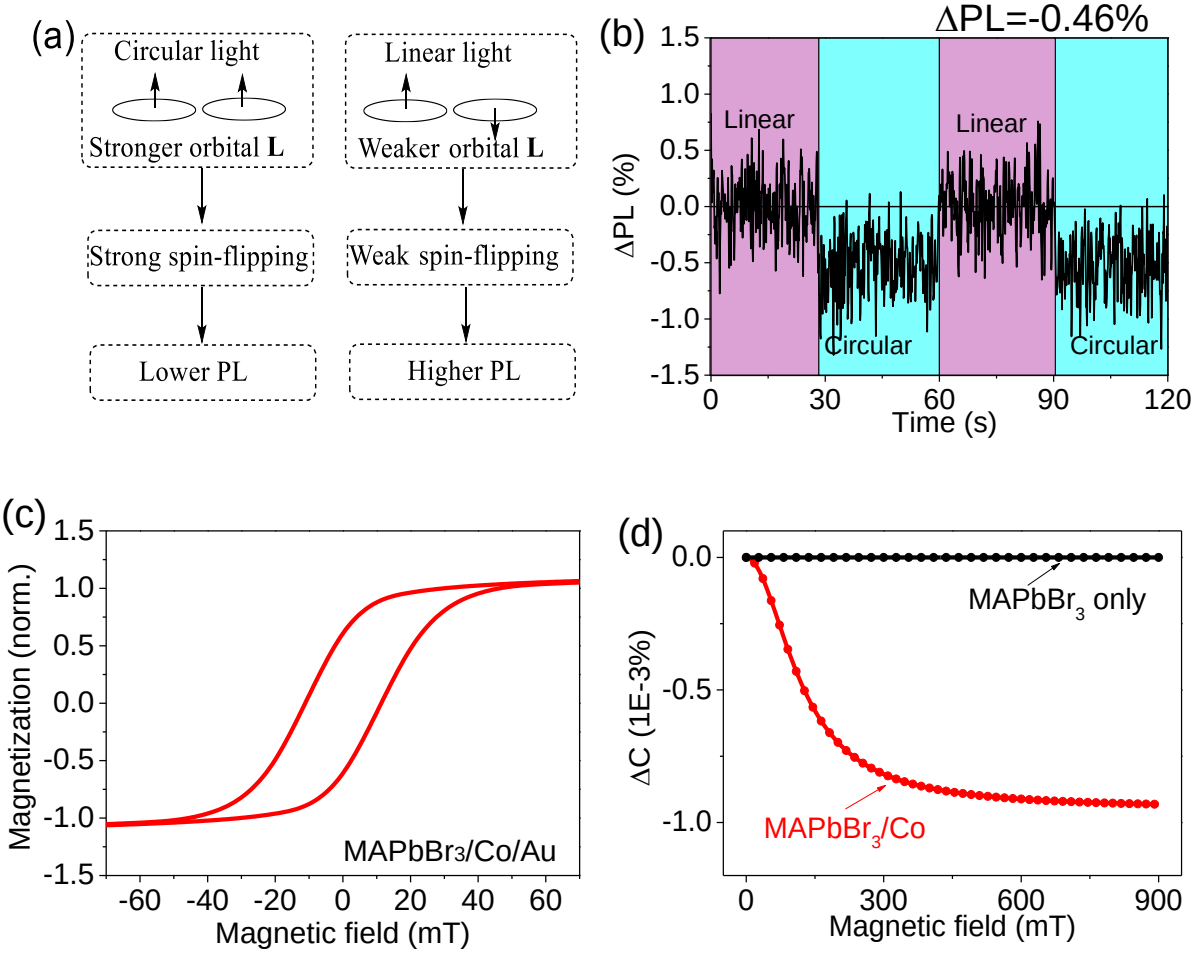

Figure 5-2 Photoluminescence and magnetic properties. (a), Schematic diagram representing the generation of polarization-modulated photoluminescence in hybrid perovskites by switching photoexcitation polarization between circular and linear polarization. (b), PL change caused by switching the photoexcitation from linear to circular. The orbital magnetic dipoles are formed in spin-polarized excited states under circularly polarized photoexcitation. (c), Magnetic hysteresis loop of the $MAPbBr_3$/Co/Au sample. (d), Magneto-dielectric effects from the two different device configurations: ITO/PMMA/$MAPbBr_3$/Co/PMMA/Ag; ITO/PMMA/$MAPbBr_3$/PMMA/Ag with the frequency of 1 kHz at dark condition.

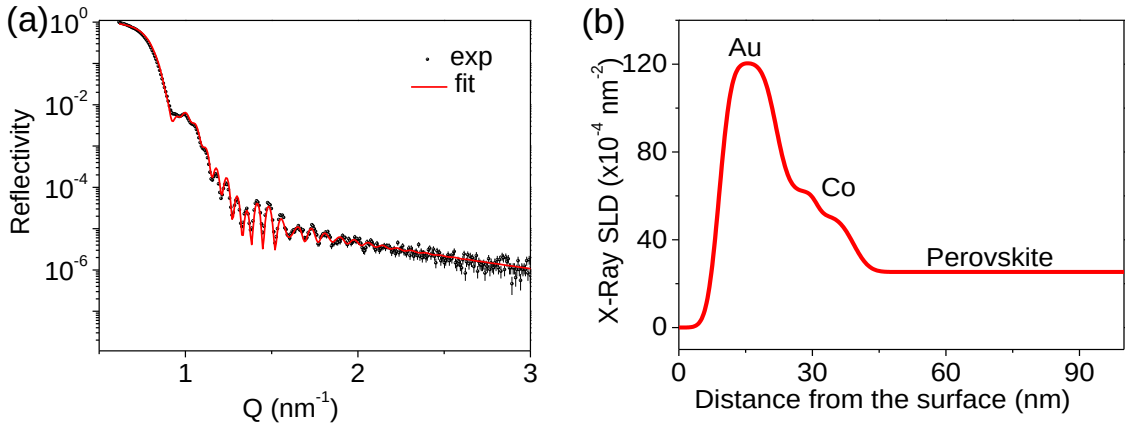

Figure 5-3 (a), X-ray reflectivity (XRR) data for the Si/MAPbBr$_3$/Co/Au sample. The black open circles show the experimental data, and the fit to the data is shown in red. (b), Chemical depth profile for the Si/MAPbBr$_3$/Co/Au sample obtained after the fit to the XRR data. The fit to the data showed that the density of the Co layer is not uniform. Instead, it forms two sublayers, Co_1 and Co_2, which exhibit lower and higher SLD values. This might be caused by the density difference during the deposition process of the Co layer on the surface of the perovskite.

Table 5-1 Fit parameters of the XRR data for Si/$MAPbBr_3$/Co/Au sample

Layers	Thickness, nm	SLD, $\times 10^{-4}$ nm^{-2}	Roughness, nm
Si	inf	20.1	2.14
SiO_2	1.375	18.9	2.33
Perovskite	65.86	25.3	1.29
Co_1	8.28	51.1	2.75
Co_2	9.09	61.9	0.02
Au	12.79	120.7	0.02

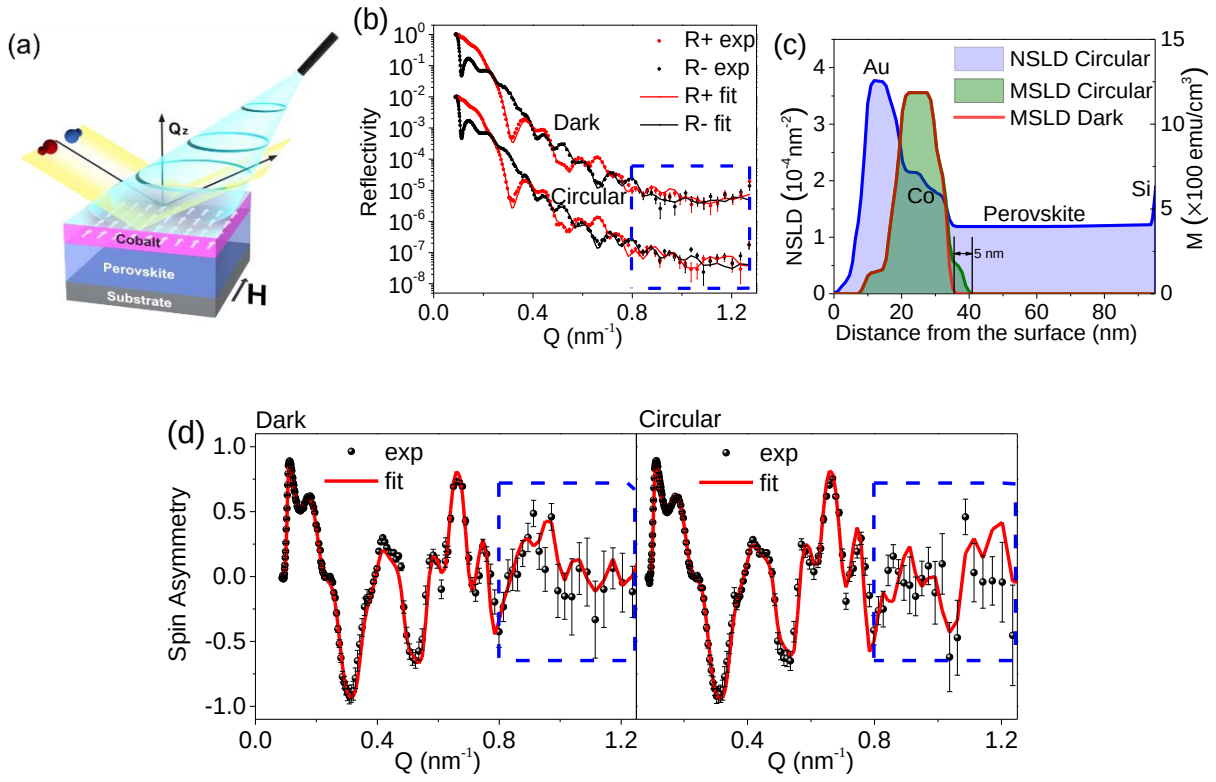

Figure 5-4 Results from probing the interface magnetism using PNR experiment with *in situ* photoexcitation. (a), Schematic of the experiment on a $MAPbBr_3$ perovskite/Co structure. The external magnetic field *H* is applied in-plane to the sample. The polarized neutron beam with neutrons spins parallel (blue arrow) or opposite (red arrow) impinging under the grazing angle at the sample. The 488 nm laser beam illuminates the entire surface of the sample. The neutron beam probes the sample in dark and under circularly polarized photoexcitation conditions. (b), Polarized neutron reflectivity plots of the first sample (N1), as a function of scattering vector magnitude Q, for a film measured in dark (top) and under circularly polarized photoexcitation (bottom). The experimental data are shown as black points with fits shown as overlying lines. (c), The full neutron nuclear and magnetic scattering length density profiles (NSLD and MSLD) obtained from the fit to the reflectivity. Overall, the magnetization in a 5 nm $MAPbBr_3$ perovskite layer (black lines) is observed under the circularly polarized laser beam excitation (green). In contrast, this magnetization effect is absent under dark condition (red solid line). The chemical composition of the interface (NSLD), shown in light purple, confirms that no Co atoms are present in the perovskite. The interfacial roughness determined from the PNR experiment is 0.5 nm. (d), The spin asymmetry ratio, SA = $(R+ - R-)/(R+ + R-)$, obtained from the experimental and fitted reflectivities, is shown for measurements performed under dark condition (left) and circularly polarized laser beam excitation (right). The blue dashed box highlights the difference in SA between the dark and circularly polarized laser beam excitation conditions in the high-Q range, due to differences in magnetization profile at the perovskite/Co interface. The error bars represent one standard deviation.

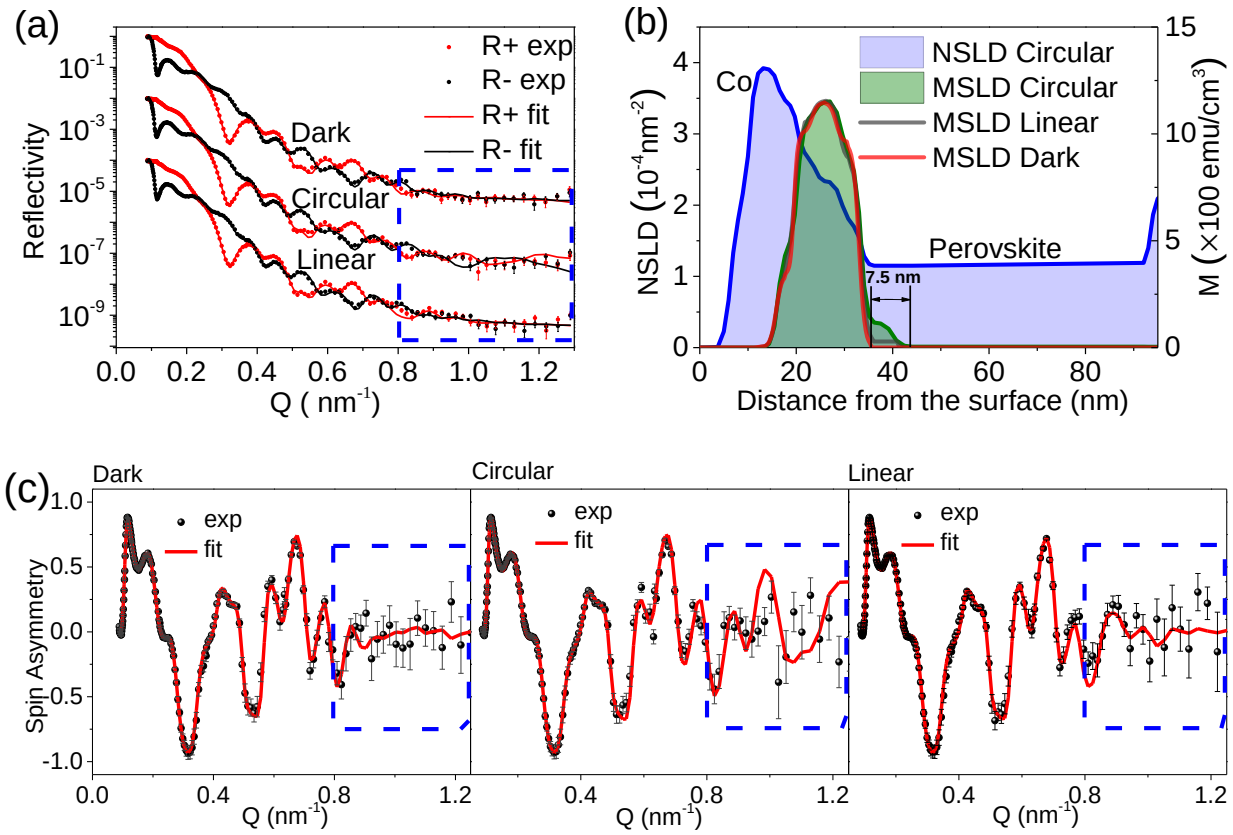

Figure 5-5 PNR experiments under dark, circularly and linearly polarized photoexcitation. (a), Polarized neutron reflectivity plots for the second $MAPbBr_3$ perovskite/Co sample (N2) measured in the dark (top), under circularly polarized photoexcitation, and linearly polarized photoexcitation (bottom). The blue dashed box highlights the difference between dark, circularly, and linearly polarized laser beam excitation conditions in high-Q range. (b), The full chemical (NSLD) and magnetization (MSLD) profiles in these three measurement conditions obtained from the fit to the reflectivity curves with the focus on the perovskite/Co interface region. (c), Spin asymmetry plots under dark (left), circularly (middle) and linearly (right) polarized laser beam excitation. The blue dashed box highlights the difference between dark, circularly, and linearly polarized laser beam excitation conditions in the high-Q range.

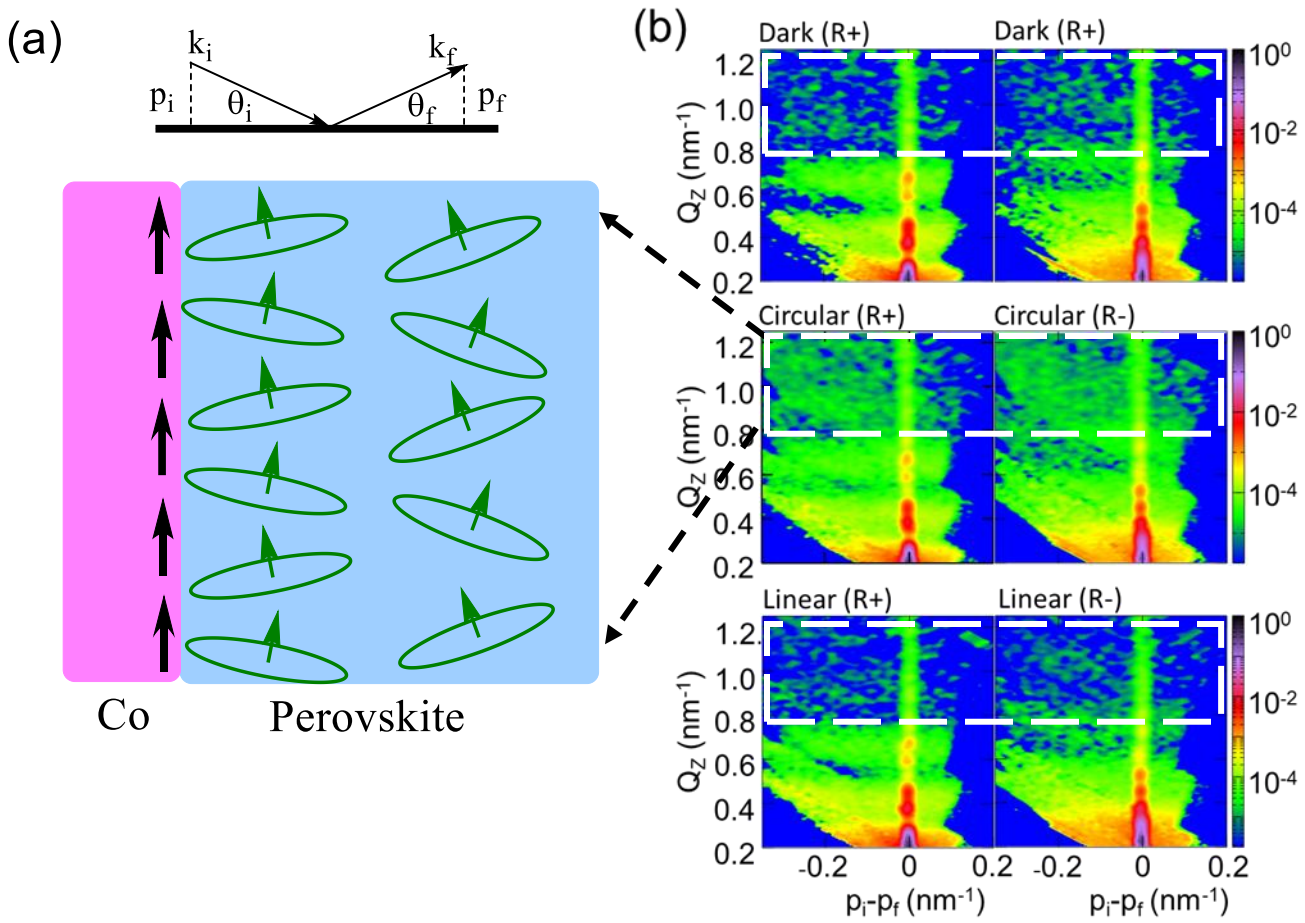

Figure 5-6 Diagram demonstrating optically induced magnetization. (a), The orbital magnetic dipoles are coupled with circularly polarized photoexcitation generated excited states with magnetic spins at $MAPbBr_3$/Co interfaces. (b), R+ and R- experimental 2D maps of the intensity scattered from the $MAPbBr_3$/Co sample as a function of $p_i - p_f$ and $Qz = p_i + p_f$, where p_i and p_f are perpendicular to the sample surface components of the incoming and the outgoing wave vectors, respectively (see inset in Figure 5-6a). The logarithmic intensity color scale is shown on the side. The strong intensity along the vertical lines at $p_i - p_f = 0$ corresponds to the specular reflectivity, which have been extracted and analyzed in Figure 5-5a. The 2D map in the middle of the panel (Figure 5-6b) was measured under circular polarization condition. The orbital magnetic dipoles result in additional magnetic scattering for $Q > 0.8$ nm^{-1}, which is absent in the top (no laser) and bottom (linear polarization) panels and marked with a white dashed rectangle.

Chapter 6. Spin dynamics in low dimensional hybrid perovskites

6.1 Abstract

This chapter investigates the spin dynamics of the 2D hybrid perovskites. We report an extremely long spin relaxation time of optically polarized light-emitting states at room temperature in quasi-2D perovskites [$(PEA)_2(MA)_4Pb_5Br_{16}$ with n = 5], when the long-range orbit-orbit interaction between excited states is developed through orbital polarization. Our studies found that, the quasi-2D perovskite [$(PEA)_2(MA)_4Pb_5Br_{16}$ with n = 5] demonstrates a long-range orbit-orbit interaction between excited states to conserve the spins of optically polarized light-emitting states, identified by the positive change on photoluminescence intensity (+ΔPL) in steady-state upon switching the photoexcitation from linear to circular polarization. Meanwhile, the PL circular polarization ($\sigma^+\sigma^+$ - $\sigma^+\sigma^-$) can maintain in nanosecond under fixed photoexcitation (σ^+). In contrast, the 2D/3D mixed perovskite (n > 5) shows a short-range orbit-orbit interaction between excited states through orbital magnetic dipoles, identified by the -ΔPL by switching from linear to circular photoexcitation. At the same time, the spin lifetime of light-emitting states becomes non-detectable. This part is revised based on the published article [M. Wang, H. Zou, J. Zhang, T. Wu, H. Xu, S. Haacke, B. Hu, J. Phys. Chem. Lett. 2020, 11, 3647.]. [135]

6.2 Introduction

Organic-inorganic hybrid perovskites possess strong orbital momentums towards forming spin-orbital coupling (SOC). The combination of high SOC and asymmetric structures provides a framework to realize the Rashba effect.[136, 137] The Rashba effect provides vital possibilities to manipulate the spin parameter in excited states by using electrical polarization in strong SOC materials. Experimentally, it was found that introducing a spin on the surface of the perovskite ($MAPbI_3$) layer through the ferromagnet/perovskite interface can generate an electric-magnetic coupling phenomenon at room temperature.[66] This phenomenon provides further evidence that the spin parameters can be conveniently tuned by electrical parameters through SOC in halide perovskites. On the other hand, magneto-PL and magneto-photocurrent have been observed at the ambient condition in such hybrid perovskites.[29, 32] This implies that the spin parameter can be conserved with the time constant comparable to exciton recombination and dissociation, providing

the experimental argument of developing spin-polarized excited states. Therefore, the hybrid perovskites hold potential promises for spin generation and manipulation towards the applications in spintronics and quantum materials.[117] Towards revealing spin parameters in such strong SOC materials, the spin-polarized carriers were successfully observed with the electron and hole spin lifetimes of 7 ps and 1 ps in halide perovskites ($MAPbI_3$) at 77 K with time-resolved Faraday rotation measurements.[25] Furthermore, by using chlorine doping, the long spin lifetime exceeding 1 ns in spin-polarized exciting states was observed at 4 K in orthorhombic phase $MAPbCl_xI_{3-x}$ films.[26] More recently, a long spin lifetime of 189 ps at room temperature has been obtained in $MAPbBr_3$ based on the spin pumping technique.[121] These interesting results provide experimental opportunities for using organic-inorganic hybrid perovskites in spintronics and quantum materials. It is noted that the organic-inorganic halide perovskites can be prepared with two-dimensional (2D) structures, leading to Ruddlesden−Popper perovskites such as $PEA_2PbI_4{\cdot}(MAPbI_3)_{n-1}$ (PEA, phenethylammonium; MA, methylammonium; n = 1, 2, 3, 4, 5) with greater property tunability and stability.[138] Therefore, 2D perovskites have become strong candidates for developing high-performance optoelectronic devices. Recently, by using circularly polarized pump-probe transient absorption, it was found that the 2D perovskites ($PEA_2PbI_4{\cdot}\ (MAPbI_3)_3$; n = 4) can demonstrate the spin lifetime of ~ 7 ps in excited states at room temperature.[139] This presents a practical method to tune the spin lifetime in 2D perovskites by using nanoplate thickness.

In this chapter, we select the quasi-2D and the 2D/3D perovskites (with n = 5 and n > 5, respectively) with long-range and short-range orbit-orbit interactions between excited states to investigate the spin lifetime of optically polarized light-emitting states by using the circularly polarized time-resolved PL measurements. We have found that, when the long-range orbit-orbit interaction is established in the quasi-2D perovskites, an extremely long spin lifetime of nanoseconds in optically polarized light-emitting states can be observed at room temperature.

6.3 Experimental methods

6.3.1 Materials preparation

Quasi-2D perovskites $PEA_2(MA)_4Pb_5Br_{16}$ (n=5) precursor was prepared by dissolving $PbBr_2$, MABr, and PEABr with mole ratio of 5:4:2 in DMSO and DMF mixed solvent (volume ratio of 3:7). The concentrations for perovskites were 0.18 M of Pb^{2+}. The precursor solution of 2D/3D perovskite was prepared by mixing the 2D (n=5) perovskite precursor solution with the 3D $MAPbBr_3$ precursor solution (volume ratio of 20:7). Then the precursor solutions were coated onto the substrate via a consecutive two-step spin coating process at 1000 (500 rpm/s) and 4000 (2000 rpm/s) rpm for 10 and 40 s, respectively. During the second spin step, 60 μL of toluene was deposited onto the substrate at 8th second. The resulting film was then annealed at 95 °C for 10 min for better crystallization.

6.3.2 The polarization- & time-resolved photoluminescence measurements

The polarization- & time-resolved photoluminescence measurements used in this work combines a Streak camera with circularly polarized photoexcitation and detection system (time resolution: 0.5% of the selected time window). The diagram of optical setup is shown in **Figure 6-1**. The samples were excited by a 405 nm pulse laser from a home-built optical parametric amplifier (OPA), seeded by the second harmonic of a Yb-doped fiber laser (TANGERINE, Amplitude System) with 50 kHz repetition rate and the pulse width of 300 fs. The focused beam size is ~ 60×60 μm^2. The pulsed laser is converted from horizontal linear polarization to circular polarization (e.g. right-hand, σ+) through a quarter-wave plate (Thorlabs, WPQ10M-405, the fast axis is set at 45° compared with the horizontal axis), while the fluorescence was counted by Streak camera (HAMAMATSU C10627) with a broad-band achromatic quarter-wave plate (B.Halle RAC 3.4.10, 460nm~680nm) in front to control the right-hand/left-hand (σ+/σ-, the fast axis is set at 45°/-45° compared with horizontal axis) detection. A vertical linear polarizer is placed in front of the spectrometer. All angles were adjusted with respect to the linearly polarized pump. To avoid the variation of PL decay dynamics caused by morphological inhomogeneity of the samples, each set of data was taken from the same sample spot.

Consider a photoluminescence process that displays N decay time (τ_1, τ_2, ..., τ_N), the intensity decay is given by

$$I(t) = \sum_{n=1}^{N} I_1 e^{-t/\tau_n} \quad (1)$$

where I_1 is the initial intensity (t=0). In our situation, the decay curve is a convolution between fluorescence emission and system instrument response (IRF), assumed to be a Gaussian of standard deviation σ, and integral 1. Therefore, a low resolution will not be able to capture decay times or processes faster than the IRF. These will give rise to a Gaussian signal pulse of width proportional to σ. Thus, the equation should be defined as

$$I(t) = Offset + \frac{A_\tau}{\sigma\sqrt{2\pi}} e^{-\frac{(t-t_0-t_{0G})^2}{2\sigma^2}} + \sum_{n=1}^{N} \frac{A_n}{2} e^{-\frac{t-t_0}{\tau_n}} \bullet (1 + erf(\frac{t - t_0 - \frac{\sigma^2}{\tau_n}}{\sigma\sqrt{2}})) e^{\frac{\sigma^2}{2\tau_n^2}} \quad (2)$$

where the offset is a constant caused by background noise. The resolution is defined as σ and

$$\frac{A_\tau}{\sigma\sqrt{2\pi}} e^{-\frac{(t-t_0-t_{0G})^2}{2\sigma^2}} \quad (3)$$

accounts for processes faster than the IRF. Also, there is a time shift defined as t_0. In our situation, t_0 should be close to zero. Then,

$$A_n e^{-\frac{t-t_0}{\tau_n}} \quad (4)$$

is the same as equation (1). Finally,

$$\frac{1}{2}(1 + erf(\frac{t - t_0 - \frac{\sigma^2}{\tau_n}}{\sigma\sqrt{2}})) e^{\frac{\sigma^2}{2\tau_n^2}} \quad (5)$$

means the convolution between fluorescence emission and IRF, where erf is Gauss error function.

In our fitting process, the σ+σ+ and σ+σ- curves are firstly fitted separately by using equation (2) to get the fitting curves as $I_{\sigma^+}^{Fit}$ and $I_{\sigma^-}^{Fit}$. After that, the degree of spin polarization was calculated by

$$\rho_c = \frac{I_{\sigma^+}^{Fit} - I_{\sigma^-}^{Fit}}{I_{\sigma^+}^{\mathrm{Fit}} + I_{\sigma^+}^{Fit}} \quad (6)$$

Then the degree of spin polarization was fitted by

$$\rho_c = r_o e^{-\frac{t}{\theta}} \quad (7)$$

to give the spin lifetime θ as well as the error bars.

For the photoexcitation polarization-dependent ΔPL measurements, a 405 nm continuous-wave (CW) semiconductor laser was combined with a linear polarizer and quarter-wave plate to generate switchable linearly and circularly polarized photoexcitations with identical intensity. The magneto-PL measurements were performed by using Horiba Fluorolog-3 spectrometer combined with an electrically controllable magnet. The photoexcitation was provided by a 405 nm CW laser.

6.4 Results and discussion

6.4.1 Long Spin Lifetime of Light-Emitting States in Quasi-2D Perovskites through Orbit–Orbit Interaction

As compared to the 3D perovskite counterparts, quasi-2D perovskites are expected to have greater tunability and enriched photophysics due to the quantum confinement,[140] breaking of structural inversion symmetry,[141, 142] and strong exciton-photon coupling.[143] Here, quasi-2D $(PEA)_2(MA)_4Pb_5Br_{16}$ (n = 5) and the 2D/3D (n > 5) perovskites were used to investigate the spin dynamics. Here, the n values are determined by the stoichiometric ratio of the perovskite precursor solutions. **Figure 6-2a** presents the absorption spectra of quasi-2D (n = 5) and the 2D/3D (n > 5) perovskite thin films fabricated with antisolvent spin-coating methods. The precursor solution of 2D/3D (n > 5) perovskite was prepared by mixing the 2D (n=5) perovskite with the 3D $MAPbBr_3$ perovskite solutions (volume ratio= 200:70). It can be seen that the 2D/3D perovskites exhibit a red-shifted band edge as compared with the quasi-2D perovskite due to the reduced 2D component. The bandgaps are determined to be 2.267 eV and 2.259 eV for quasi-2D (n=5) and 2D/3D (n>5) perovskites, respectively. The absorption peak close to 400 nm is attributed to the small portion of n=1 nanoplates (PEA_2PbBr_4) in the solution processed films.[144] Due to the higher concentration of PEA in quasi-2D n=5 perovskite, the n=1 nanoplates (PEA_2PbBr_4) are more easily to form and consequently give stronger absorption peak close to 400 nm, as compared with 2D/3D n>5 perovskite. As shown in the inset of **Figure 6-2b**, the PL peak for quasi-2D perovskite is located at 525 nm while the PL spectrum of 2D/3D (n > 5) perovskite is red-shifted to 533 nm, which is consistent with the red-shifted band edge in absorption spectrum. This indicates that the PL in quasi-2D perovskite is mainly from the n = 5 perovskite nanoplates while the PL in 2D/3D perovskite is more likely from the 3D component. Meanwhile, the quasi-2D perovskite gives stronger PL intensity as compared with 2D/3D perovskite. Generally, reducing the nanoplate

thickness by decreasing n value in quasi-2D perovskites leads to increased exciton binding energy and faster charge carrier recombination owing to quantum and dielectric confinements.[145, 146] By comparing the relationship between PL count and excitation intensity, we found that the power factor for quasi-2D n=5 perovskite is close to 1, while the 2D/3D (n>5) perovskite has the power factor of 1.62. This indicates that the monomolecular recombination from excitons dominates in the quasi-2D n=5 perovskite. In contrast, the bimolecular recombination from charge carriers dominantly occurs in 2D/3D (n>5) perovskite.

Hybrid metal halide perovskites carry both orbital (***L***) and spin (***S***) momentum, making the total exciton angular momentum ***J*** conserved quantum number. Consequently, the excited states are denoted as ***J*** states where $\boldsymbol{J} = \boldsymbol{L} + \boldsymbol{S}$.[31, 147] When the excited states develop a mutual interaction, this interaction can occur between orbital polarizations or between orbital magnetic dipoles, as schematically illustrated in **Figure 6-3**. Here, we define the former and latter as long-range and short-range orbit-orbit interaction, respectively. If the orbital polarization between excited states under circularly polarized photoexcitation is conserved before the occurrence of PL, the orbital magnetic dipoles can establish an order between light-emitting states. This gives rise to spin-polarized light-emitting states, leading to a spin-polarized PL. In contrast, if the orbital polarization between excited states under circularly polarized photoexcitation is completely relaxed before the occurrence of PL, the orbital magnetic dipoles become random between light-emitting states. This generates a non-spin-polarized PL. Here, we use circularly polarized time-resolved PL to directly monitor the spin lifetime of light-emitting states in 2D and 2D/3D perovskite thin films at room temperature. This method has been widely used to investigate the optical spin orientation in inorganic semiconductors.[148-150] **Figure 6-4a** shows the wavelength-integrated time-resolved PL decay traces of quasi-2D perovskite thin film under σ^+ photoexcitation at 405 nm with the power of 6μW while the detection is switched between σ^+ and σ^- polarizations. We can see that the PL intensity is enhanced by 11 % at time zero when switching the detection from σ^- to σ^+. This PL intensity difference between $\sigma^+$and σ^- detections at σ^+excitation gradually disappears. In particular, the curve fitting determines the spin lifetime τ_s of 2.5 ns. Meanwhile, we can see an appreciable change between σ^- and σ^+ detection in the time-integrated PL spectra within 20 ns time window under σ^+ excitation (**Figure 6-4b**). Here, the observed changes in both PL decay

dynamics and time-integrated PL spectra between σ^- to σ^+ detections at σ^+ excitation show that the spin-polarized states generated by a circularly polarized photoexcitation can indeed generate a circularly-polarized PL in the quasi-2D perovskite samples at room temperature. We further examined the excitation intensity dependence of spin lifetime to understand spin dephasing mechanism. It is can be seen in **Figure 6-4c** that when the pumping density increases from 4 μW to 17 μW, the spin lifetime is reduced from 3.4 ns to 0.9 ns. This indicates that the circularly photoexcitation generated spin-polarized excited states experience a mutual spin scattering under high excitation density, consequently reducing the spin lifetime. To investigate how orbit-orbit interaction can influence the spin lifetime, we further measured the 2D/3D perovskite films under the same circumstances. These time-resolved PL polarization measurements on the 2D/3D perovskite films do not detect any circularly polarized emission when switching the detection between σ^- and σ^+ polarizations under the σ^+ excitation at room temperature (**Figure 6-4d**). Meanwhile, the time-integrated PL spectra do not show any change between σ^- and σ^+ detection (**Figure 6-4e**). These results suggest an extremely short spin lifetime in 2D/3D perovskite films which could not be resolved by the setup used in this measurement.

Now, we identify the long-range and short-range orbit-orbit interactions occurring in quasi-2D and 2D/3D perovskite films by monitoring the change of PL (ΔPL) caused by switching the photoexcitation between linear and circular polarizations. Here ΔPL is defined by $\Delta PL = \frac{I_{circular} - I_{linear}}{I_{linear}}$, where I_{linear} and $I_{circular}$ are the PL intensities under linear and circular photoexcitations, respectively. We should note that a circularly polarized photoexcitation generates the excited states with the orbital magnetic dipoles in same direction while orbital polarizations are synchronized to rotate with parallel alignment. Contrarily, under a linearly polarized photoexcitation, the excited states are generated with the orbital dipoles in opposite directions while the orbital polarizations are opposite to rotate with anti-parallel alignment, as indicated in **Figure 6-5**. If long-range interaction between orbital polarization dominates the orbit-orbit interaction, the parallel alignment of orbital polarization between excited states under circularly polarized photoexcitation can avoid mutual dissociation, leading to a higher PL intensity. However, the anti-parallel alignment of orbital polarization between excited states under linearly

polarized photoexcitation can cause a mutual dissociation, generating a lower PL intensity. This leads to a positive ΔPL upon switching the photoexcitation from linear-to-circular polarization. Therefore, this presents a practical scenario to identify the long-range orbit-orbit interaction through orbital polarizations between excited states by using ΔPL measurements. Here, we can see in **Figure 6-6** that quasi-2D perovskite film shows a positive ΔPL upon switching the photoexcitation from linear-to-circular polarization. This provides an experimental indication that the long-range orbit-orbit interaction occurs through orbital polarizations between excited states. We should further note that, when the short-range orbit-orbit interaction becomes a dominant component through the interaction between orbital magnetic dipoles, a circularly polarized photoexcitation generates the orbital magnetic dipoles with the same direction between excited states while a linearly polarized photoexcitation leads to the orbital magnetic dipoles with opposite directions between excited states. This forms stronger and weaker total orbital magnetic dipole momentums under circularly and linearly polarized photoexcitations, respectively. Furthermore, the stronger total orbital magnetic dipole momentums can cause a larger spin flipping on optically generated light-emitting states, converting spin-allowed states into spin-forbidden states and leading to a lower PL intensity under circularly polarized photoexcitation as compared to the weaker total orbital magnetic dipole momentums under linearly polarized photoexcitation. Therefore, μhen short-range orbit-orbit interaction dominates through the interaction between orbital magnetic dipoles, switching the photoexcitation from linear-to-circular polarization gives rise to a negative ΔPL. Here, we can see that the 2D/3D perovskite film shows a negative ΔPL upon switching the photoexcitation from linear-to-circular polarization. This indicates that the short-range orbit-orbit interaction occurs between orbital magnetic dipoles in excited states in 2D/3D perovskites. The non-detectable spin lifetime in 2D/3D perovskite film indicates that the short-range orbit-orbit interaction between orbital magnetic dipoles causes a major spin dephasing in excited states.

To gain further insight on the spin dynamics of excited states, we performed magneto-PL measurements under circularly and linearly polarized photoexcitation in these 2D and 2D/3D perovskite films. We should note that magneto-PL has been widely observed in organic materials and hybrid perovskites at room temperature. Essentially, magneto-PL can be observed when a

magnetic field disturbs the populations on bright and dark states by introducing coherent or in-coherent spin precessions on electron-hole pairs in an excited state. There is a basic requirement to realize magneto-PL: the spin dynamics of excited states must be comparable with the field-induced spin-mixing time. When the field-induced spin-mixing can occur before the spin coherence is lost, magneto-PL can then be observed. Interestingly, we can see in **Figure 6-7a** that the 2D perovskite film shows detectable magneto-PL under circularly polarized photoexcitation. This observation further indicates that, when long-range orbit-orbit interaction is established between orbital polarization in excited states by using circular photoexcitation, the 2D perovskite film can demonstrate a long spin lifetime in excited states in nanosecond time window. Clearly, magneto-PL provides further evidence to show that long-range orbit-orbit interaction between orbital polarization plays an important role in maintaining the spin polarization in excited states in hybrid perovskites. In contrast, we can see in **Figure 6-7b** that the 2D/3D perovskite film, where the short-range orbit-orbit interaction dominates between orbital magnetic dipoles, does not show any magneto-PL. This further indicates that the short-range orbit-orbit interaction between orbital magnetic dipoles causes a spin dephasing, leading to a non-detectable spin lifetime of excited states in hybrid perovskites.

6.5 Conclusion

In summary, we have investigated the spin dynamics of excited states in quasi-2D and 2D/3D perovskite films with long-range and short-range orbit-orbit interactions. By measuring time-resolved circularly polarized PL with circularly polarized photoexcitation, we found that quasi-2D perovskite [$(PEA)_2(MA)_4Pb_5Br_{16}$ with n = 5] film demonstrates an extremely long spin lifetime in the order of nanoseconds in light-emitting excitons at room temperature. In contrast, the 2D/3D perovskite film shows a non-detectable spin lifetime within the nanosecond time window. Furthermore, the orbit-orbit interaction between light-emitting excitons was identified by monitoring the PL intensity while switching the photoexcitation between linear and circular polarization. We observed that the quasi-2D perovskite (n=5) film shows a long-range orbit-orbit interaction occurring between orbital polarization in excited states. Contrarily, the 2D/3D perovskite (n>5) film exhibits a short-range orbit-orbit interaction occurring between orbital magnetic dipoles in excited states. Because quasi-2D and 2D/3D perovskite films demonstrate

long and non-detectable spin lifetimes, we can conclude that the long-range and short-range orbit-orbit interactions function as primary factors to control the spin dynamics of light-emitting states in hybrid perovskites. Clearly, the long spin lifetime provides new opportunities to control the optoelectronic processes by using spin-polarized excited states in organic-inorganic hybrid perovskites.

Appendix

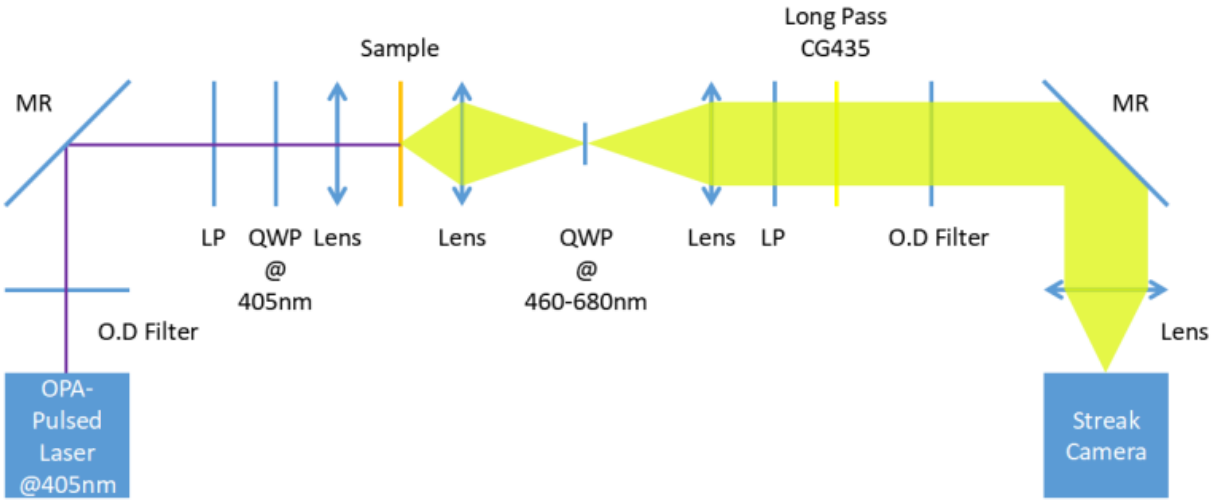

Figure 6-1 Principal experimental setup of circularly polarized time-resolved PL measurements.

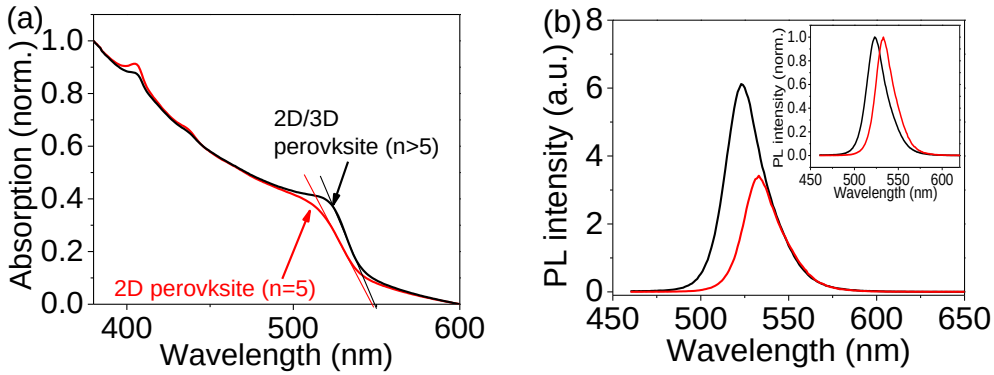

Figure 6-2 Spectral characteristics for quasi-2D (n=5) and 2D/3D (n>5) perovskites. (a) Absorption spectra. (b) PL spectra. The inset shows the normalized PL spectra.

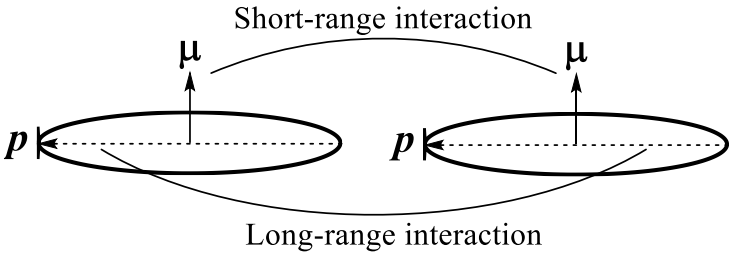

Figure 6-3 Long-range and short-range orbit-orbit interactions occur between orbital polarizations and magnetic dipoles in excited states.

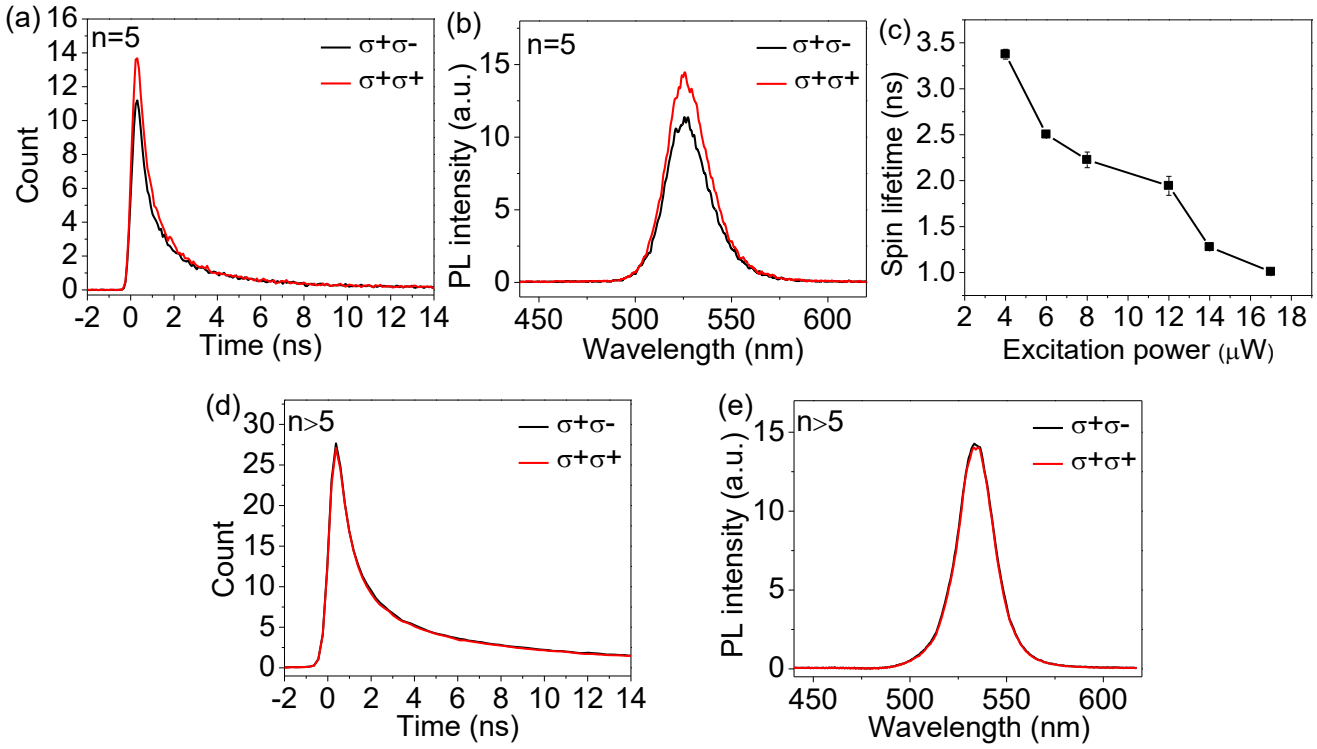

Figure 6-4 Excitation power dependent spin lifetime in quasi-2D (n=5) and 2D/3D (n>5) perovskite through circularly polarized time-resolved PL measurements. (a) wavelength-integrated PL decay dynamics under right-hand circularly polarized excitation (σ^+, 405 nm, excitation 6 μW), and σ^+ (right-hand)/σ^- (left-hand) detection for quasi-2D (n=5) sample; (b) time-integrated PL spectra (within 20 ns time window) under σ^+ excitation and σ^+/σ^- detection for quasi-2D (n=5) sample; (c) Spin lifetime as the function of excitation power for quasi-2D (n=5) sample; (d) wavelength-integrated decay dynamics under circularly polarized excitation (σ^+, 405 nm, excitation 6 μW), and σ^+/σ^- detection for 2D/3D (n>5) sample; (e) time-integrated PL spectra (within 20 ns time window) under σ^+ excitation and σ^+/σ^- detection for 2D/3D (n>5) sample.

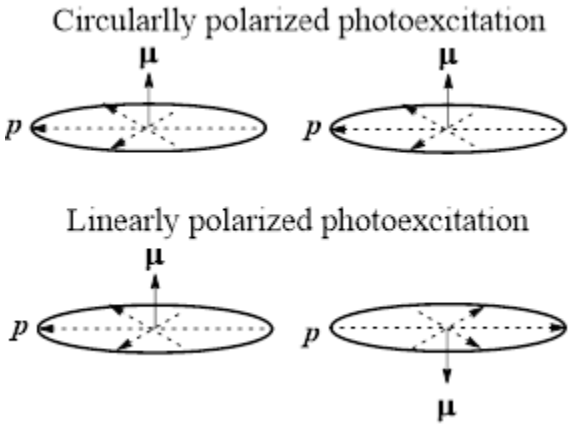

Figure 6-5 Orbital polarizations and magnetic dipoles are generated between excited states by circularly and linearly polarized photoexcitations.

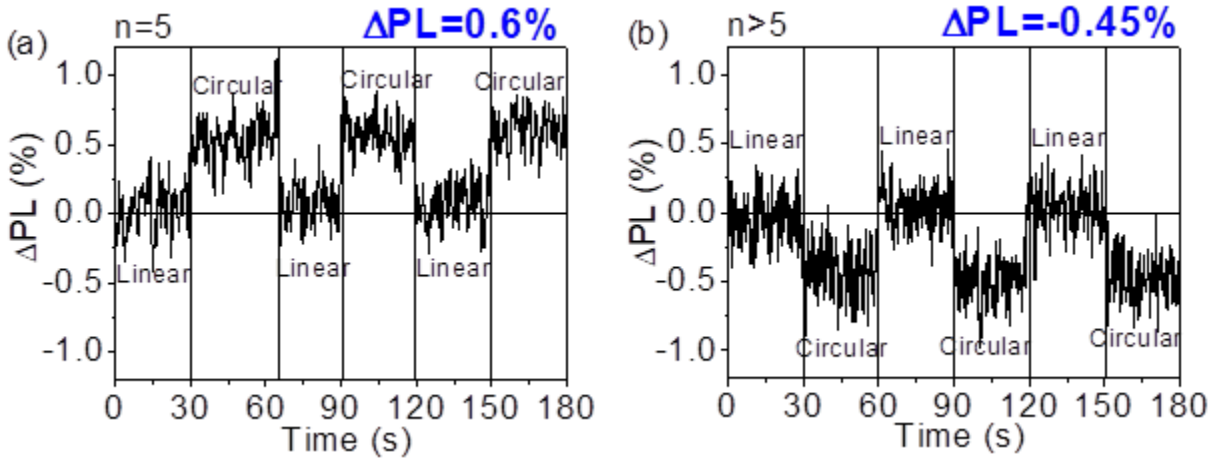

Figure 6-6 (a) Positive ΔPL in quasi-2D (n=5) perovskite and (b) negative ΔPL in 2D/3D (n>5) perovskite.

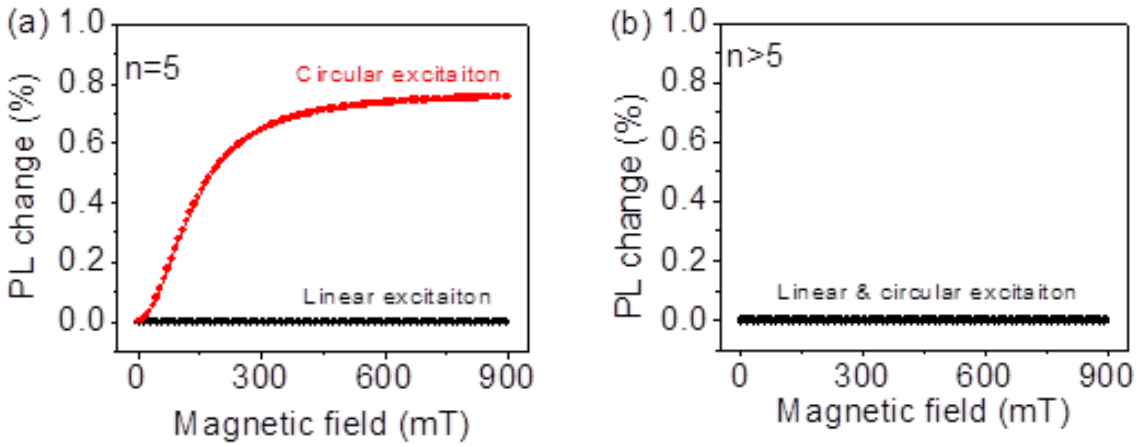

Figure 6-7 Circular/linear excitation modulated magneto-PL. (a) quasi-2D (n=5) perovskite. (b) 2D/3D (n>5) perovskite.

Chapter 7. Conclusion and Outlook

This dissertation was focused on the spin effects of excited states to reveal the fundamental working principle of the newly emerging organic semiconductor and hybrid perovskite systems through advanced optical, electrical, and magnetic characterizations. Addressing these issues is of great importance to gain an in-depth understanding of the key optoelectronic and spintronic processes and provide insightful guidance for the development of the next-generation organic and hybrid perovskite optoelectronics and spintronics. The overall conclusions can be divided into two categories with the focus on organic semiconductors and hybrid perovskites.

I. Organic semiconductors

In organic semiconductors with weak orbital angular momentum, the total angular momentum of the excitons in organics mainly results from total spin angular momentum $\mathbf{S}=\mathbf{S}_e+\mathbf{S}_h$ of the constituent electron and hole. The competition between the spin-conserving, mainly from exchange interaction, and the spin-mixing from internal magnetic interactions establishes an equilibrium on the singlet and triplet populations in electron-hole pairs. An external magnetic field can easily break this equilibrium and change the singlet and triplet populations in loosely bounded electron-hole pairs, leading to a variety of MFEs in organic semiconductors. By MFEs as the convenient technique to monitor the spin states in organic optoelectronic devices, we have revealed that 1) the spatially extended states are formed in the low dielectric constant F8BT organic microcavity light-emitting devices, responsible for the spectrally narrowing phenomenon in microcavity structures; 2) photogenerated electron-hole pairs can be directly dissociated in four-fold symmetry ClAlPc molecules due to the low electron-hole binding energy, leading to the high-efficiency in ClAlPc-based single active layer photovoltaic device. Furthermore, we have investigated the key spin-mixing process in the donor-acceptor type TADF molecules through magneto-optical methods. We confirmed the spin-orbital coupling is the dominating spin-flipping mechanism that converts the non-radiative triplets to radiative singlets. Finally, we have explored the spin, energy, and polarization parameters in exciplex systems with physically mixed donor and acceptor molecules for efficient light-emitting diodes. We have established the cooperative

relationship among the spin, energy, and polarization to gain an in-depth understanding of the spin-dependent light-emitting properties in exciplex systems. Inspired by the work, we further studied the detailed excited state behaviors of the high-efficiency exciplex host and phosphorescent dopant systems. Our studies reveal the efficient Foster and Dexter energy transfer channels from exciplex host to phosphorescent dopants as well as the critical role of polarization memory of the transient dipoles in determining the light-emitting efficiency through light out-coupling, providing a critical guideline to further advance the developments of organic light-emitting diodes.

II. Hybrid perovskites

Unlike the organic semiconductors with the **S** states. Hybrid perovskite materials possess a strong orbital field, in which the valence and conduction bands are mainly associated with cationic (Pb) *s* (l = 0) and *p* (l = 1) orbitals, respectively. The total angular momentum for an exciton in perovskites is $\boldsymbol{J}=\boldsymbol{J}_e+\boldsymbol{J}_h$ with J_e=1/2 and J_h=1/2. Consequently, spin-dependent optical selection rules allow the efficient manipulation of spin-polarized carriers or excitons in perovskites through circularly polarized light. By using the depth-sensitive polarized neutron reflectometry technique, we found that the optically induced magnetization can be observed with thicknesses up to ~7.5 nm into $MAPbBr_3$ layer in the presence of ferromagnetic Co when orbital magnetic dipoles are generated in the same direction under a circularly polarized photoexcitation. These studies represent an exciting discovery of the photoinduced room-temperature ferromagnetism in perovskite with heterostructure design and have far-reaching consequences, as it paves the way for the realization of new ferromagnetically tunable semiconductor materials through optical method for next-generation spin-related optoelectronics. Furthermore, we have investigated the spin dynamics of excited states in quasi-2D perovskite thin films through ultrafast laser spectroscopy. By measuring time-resolved circularly polarized PL with circularly polarized photoexcitation, we found that quasi-2D perovskite [$(PEA)_2(MA)_4Pb_5Br_{16}$ with n = 5] film demonstrates an extremely long spin lifetime in the order of nanoseconds in light-emitting excitons at room temperature. The long spin lifetime provides new opportunities to control the optoelectronic processes by using spin-polarized excited states in organic-inorganic hybrid perovskites.

Bibliography

[1] B. Hu, L. Yan, M. Shao, Adv. Mater., 21 (2009) 1500-1516.
[2] H. Xu, M. Wang, Z.-G. Yu, K. Wang, B. Hu, Adv. Phys., 68 (2019) 49-121.
[3] R. Merrifield, J. Chem. Phys, 48 (1968) 4318-4319.
[4] V. Ern, R. Merrifield, Phys. Rev. Lett., 21 (1968) 609.
[5] D. Sun, E. Ehrenfreund, Z.V. Vardeny, ChemCommun, 50 (2014) 1781-1793.
[6] V. Dediu, M. Murgia, F. Matacotta, C. Taliani, S. Barbanera, Solid State Communications, 122 (2002) 181-184.
[7] Z. Xiong, D. Wu, Z.V. Vardeny, J. Shi, Nature, 427 (2004) 821-824.
[8] E. Frankevich, A. Lymarev, I. Sokolik, F. Karasz, S. Blumstengel, R. Baughman, H. Hörhold, Phys. Rev. B, 46 (1992) 9320.
[9] J. Kalinowski, M. Cocchi, D. Virgili, P. Di Marco, V. Fattori, Chem. Phys. Lett., 380 (2003) 710-715.
[10] Ö. Mermer, G. Veeraraghavan, T. Francis, Y. Sheng, D. Nguyen, M. Wohlgenannt, A. Köhler, M.K. Al-Suti, M.S. Khan, Phys. Rev. B, 72 (2005) 205202.
[11] H. Zang, L. Yan, M. Li, L. He, Z. Gai, I. Ivanov, M. Wang, L. Chiang, A. Urbas, B. Hu, Sci. Rep., 3 (2013) 2812.
[12] J. Frenkel, Physical Review, 37 (1931) 17.
[13] G.H. Wannier, Physical Review, 52 (1937) 191.
[14] F. Nüesch, E. Forsythe, Q. Le, Y. Gao, L. Rothberg, J. Appl. Phys., 87 (2000) 7973-7980.
[15] Y. Wu, Z. Xu, B. Hu, J. Howe, Phys. Rev. B, 75 (2007) 035214.
[16] I. Žutić, J. Fabian, S.D. Sarma, Rev. Mod. Phys., 76 (2004) 323.
[17] M. Wu, J. Jiang, M. Weng, Phys. Rep., 493 (2010) 61-236.
[18] T. Basel, D. Sun, S. Baniya, R. McLaughlin, H. Choi, O. Kwon, Z.V. Vardeny, Adv. Electron. Mater., 2 (2016) 1500248.
[19] S. Baniya, Z. Pang, D. Sun, Y. Zhai, O. Kwon, H. Choi, B. Choi, S. Lee, Z.V. Vardeny, Adv. Funct. Mater., 26 (2016) 6930-6937.
[20] Y. Wang, K. Sahin-Tiras, N.J. Harmon, M. Wohlgenannt, M.E. Flatté, Phys. Rev. X, 6 (2016) 011011.
[21] H. Zang, Y. Liang, L. Yu, B. Hu, Adv. Energy Mater., 1 (2011) 923-929.
[22] Z. Xu, B. Hu, Adv. Funct. Mater., 18 (2008) 2611-2617.
[23] A.J. Heeger, Adv. Mater., 26 (2014) 10-28.
[24] Y.-C. Hsiao, T. Wu, M. Li, W. Qin, L. Yu, B. Hu, Nano Energy, 26 (2016) 595-602.
[25] D. Giovanni, H. Ma, J. Chua, M. Grätzel, R. Ramesh, S. Mhaisalkar, N. Mathews, T.C. Sum, Nano letters, 15 (2015) 1553-1558.
[26] P. Odenthal, W. Talmadge, N. Gundlach, R. Wang, C. Zhang, D. Sun, Z.-G. Yu, Z.V. Vardeny, Y.S. Li, Nature Physics, 13 (2017) 894.
[27] Z.-G. Yu, Y.S. Li, J. Phys. Chem. C, 123 (2019) 14701-14706.
[28] M. Hirasawa, T. Ishihara, T. Goto, K. Uchida, N. Miura, Physica B Condens. Matter, 201 (1994) 427-430.

[29] C. Zhang, D. Sun, C. Sheng, Y. Zhai, K. Mielczarek, A. Zakhidov, Z. Vardeny, Nature Physics, 11 (2015) 427.
[30] Y.-C. Hsiao, T. Wu, M. Li, Q. Liu, W. Qin, B. Hu, J. Mater. Chem. A, 3 (2015) 15372-15385.
[31] Z. Yu, Sci. Rep., 6 (2016) 28576.
[32] Y.C. Hsiao, T. Wu, M. Li, B. Hu, Adv. Mater., 27 (2015) 2899-2906.
[33] M. Wang, J. Lin, Y.-C. Hsiao, X. Liu, B. Hu, Nat. Commun., 10 (2019) 1614.
[34] M. Wang, Y.-Z. Li, H.-C. Chen, C.-W. Liu, Y.-S. Chen, Y.-C. Lo, C.-S. Tsao, Y.-C. Huang, S.-W. Liu, K.-T. Wong, B. Hu, Mater. Horiz., 7 (2020) 1171-1179.
[35] M. Knupfer, Appl. Phys. A, 77 (2003) 623-626.
[36] G.D. Scholes, G. Rumbles, Nat. Mater., 5 (2006) 683-696.
[37] J.H. Burroughes, D.D. Bradley, A. Brown, R. Marks, K. Mackay, R.H. Friend, P. Burns, A. Holmes, nature, 347 (1990) 539-541.
[38] I.D.W. Samuel, G.A. Turnbull, Chem. Rev., 107 (2007) 1272-1295.
[39] M. Baldo, R. Holmes, S. Forrest, Phys. Rev. B, 66 (2002) 035321.
[40] O. Mhibik, S. Forget, D. Ott, G. Venus, I. Divliansky, L. Glebov, S. Chénais, Light Sci. Appl., 5 (2016) e16026-e16026.
[41] S.R. Forrest, Nature, 428 (2004) 911.
[42] X. He, G. Zhu, J. Yang, H. Chang, Q. Meng, H. Zhao, X. Zhou, S. Yue, Z. Wang, J. Shi, Sci. Rep., 5 (2015) 17076.
[43] H.T. Chandran, T.W. Ng, Y. Foo, H.W. Li, J. Qing, X.K. Liu, C.Y. Chan, F.L. Wong, J.A. Zapien, S.W. Tsang, Adv. Mater., 29 (2017) 1606909.
[44] K. Cnops, B.P. Rand, D. Cheyns, B. Verreet, M.A. Empl, P. Heremans, Nat. Commun., 5 (2014) 3406.
[45] T. Mani, S.A. Vinogradov, J. Phys. Chem. Lett., 4 (2013) 2799-2804.
[46] J. Mezyk, R. Tubino, A. Monguzzi, A. Mech, F. Meinardi, Phys. Rev. Lett., 102 (2009) 087404.
[47] M. Wang, T. Chatterjee, C.J. Foster, T. Wu, C.-L. Yi, H. Yu, K.-T. Wong, B. Hu, J. Mater. Chem. C, 8 (2020) 3395-3401.
[48] M. Wang, H.S. Shin, F. Zhou, H. Xu, P. Prabhakaran, B. Dryzhakov, H. Su, K.-S. Lee, B. Hu, J. Phys. Chem. C, 124 (2020) 14832–14837.
[49] H. Uoyama, K. Goushi, K. Shizu, H. Nomura, C. Adachi, Nature, 492 (2012) 234.
[50] K. Goushi, K. Yoshida, K. Sato, C. Adachi, Nat. Photonics, 6 (2012) 253.
[51] P.L. Santos, J.S. Ward, P. Data, A.S. Batsanov, M.R. Bryce, F.B. Dias, A.P. Monkman, J. Mater. Chem. C, 4 (2016) 3815-3824.
[52] O. Bolton, K. Lee, H.-J. Kim, K.Y. Lin, J. Kim, Nat. Chem., 3 (2011) 205.
[53] N. Haase, A. Danos, C. Pflumm, A. Morherr, P. Stachelek, A. Mekic, W. Brütting, A.P. Monkman, J. Phys. Chem. C, 122 (2018) 29173-29179.
[54] T. Hosokai, H. Matsuzaki, H. Nakanotani, K. Tokumaru, T. Tsutsui, A. Furube, K. Nasu, H. Nomura, M. Yahiro, C. Adachi, Sci. Adv., 3 (2017) e1603282.
[55] F.B. Dias, K.N. Bourdakos, V. Jankus, K.C. Moss, K.T. Kamtekar, V. Bhalla, J. Santos, M.R. Bryce, A.P. Monkman, Adv. Mater., 25 (2013) 3707-3714.
[56] Y. Olivier, B. Yurash, L. Muccioli, G. D'Avino, O. Mikhnenko, J.-C. Sancho-Garcia, C. Adachi, T.-Q. Nguyen, D. Beljonne, Phys. Rev. Mater., 1 (2017) 075602.
[57] H. Noda, X.-K. Chen, H. Nakanotani, T. Hosokai, M. Miyajima, N. Notsuka, Y. Kashima, J.-L. Brédas, C. Adachi, Nat. Mater., (2019) 1-7.

[58] W.-L. Tsai, M.-H. Huang, W.-K. Lee, Y.-J. Hsu, K.-C. Pan, Y.-H. Huang, H.-C. Ting, M. Sarma, Y.-Y. Ho, H.-C. Hu, ChemCommun, 51 (2015) 13662-13665.
[59] T.D. Nguyen, G. Hukic-Markosian, F. Wang, L. Wojcik, X.-G. Li, E. Ehrenfreund, Z.V. Vardeny, Nat. Mater., 9 (2010) 345.
[60] P. Bobbert, T. Nguyen, F. Van Oost, v.B. Koopmans, M. Wohlgenannt, Phys. Rev. Lett., 99 (2007) 216801.
[61] Y. Sheng, T. Nguyen, G. Veeraraghavan, Ö. Mermer, M. Wohlgenannt, Phys. Rev. B, 75 (2007) 035202.
[62] T.D. Nguyen, Y. Sheng, J. Rybicki, G. Veeraraghavan, M. Wohlgenannt, J. Mater. Chem., 17 (2007) 1995-2001.
[63] J. Rybicki, T.D. Nguyen, Y. Sheng, M. Wohlgenannt, Synth. Met., 160 (2010) 280-284.
[64] R. Geng, T.T. Daugherty, K. Do, H.M. Luong, T.D. Nguyen, J. Sci. Adv. Mater. Devices, 1 (2016) 128-140.
[65] S. Liang, R. Geng, B. Yang, W. Zhao, R.C. Subedi, X. Li, X. Han, T.D. Nguyen, Sci. Rep., 6 (2016) 19461.
[66] M. Li, L. Li, R. Mukherjee, K. Wang, Q.G. Liu, Q. Zou, H. Xu, J. Tisdale, Z. Gai, I.N. Ivanov, D. Mandrus, B. Hu, Adv. Mater., 29 (2016).
[67] L. Yan, M. Wang, N. Raju, A. Epstein, L.-S. Tan, A. Urbas, L.Y. Chiang, B. Hu, J. Am. Chem. Soc., 134 (2012) 3549-3554.
[68] C. Grewer, H.-D. Brauer, The Journal of Physical Chemistry, 98 (1994) 4230-4235.
[69] F. Wilkinson, A.A. Abdel-Shafi, J. Phys. Chem. A, 103 (1999) 5425-5435.
[70] F.B. Dias, J. Santos, D.R. Graves, P. Data, R.S. Nobuyasu, M.A. Fox, A.S. Batsanov, T. Palmeira, M.N. Berberan‐Santos, M.R. Bryce, Adv. Sci., 3 (2016) 1600080.
[71] J. Gibson, A.P. Monkman, T.J. Penfold, ChemPhysChem, 17 (2016) 2956-2961.
[72] M.K. Etherington, J. Gibson, H.F. Higginbotham, T.J. Penfold, A.P. Monkman, Nat. Commun., 7 (2016) 13680.
[73] P.L. dos Santos, J.S. Ward, A.S. Batsanov, M.R. Bryce, A.P. Monkman, J. Phys. Chem. C, 121 (2017) 16462-16469.
[74] L. Ouahab, T. Enoki, Eur. J. Inorg. Chem., 2004 (2004) 933-941.
[75] N. Hanasaki, H. Tajima, M. Matsuda, T. Naito, T. Inabe, Phys. Rev. B, 62 (2000) 5839.
[76] C. Hintze, U.E. Steiner, M. Drescher, ChemPhysChem, 18 (2017) 6-16.
[77] M. Li, L. He, H. Xu, M. Shao, J. Tisdale, B. Hu, J. Phys. Chem. Lett., 6 (2015) 4319-4325.
[78] H.A. Al Attar, A.P. Monkman, Adv. Mater., 28 (2016) 8014-8020.
[79] D.-d. Zhang, K. Suzuki, X.-z. Song, Y. Wada, S. Kubo, L. Duan, H. Kaji, ACS Appl. Mater. Interfaces, 11 (2019) 7192-7198.
[80] C. Li, J. Liang, B. Liang, Z. Li, Z. Cheng, G. Yang, Y. Wang, Adv. Opt. Mater., (2019) 1801667.
[81] J.R. Lakowicz, Principles of fluorescence spectroscopy, Springer Science & Business Media2013.
[82] M. Wang, Y.H. Huang, K.S. Lin, T.H. Yeh, J. Duan, T.Y. Ko, S.W. Liu, K.T. Wong, B. Hu, Adv. Mater., 31 (2019) 1904114.
[83] Y. Liu, C. Li, Z. Ren, S. Yan, M.R. Bryce, Nat. Rev. Mater., 3 (2018) 18020.
[84] T.A. Lin, T. Chatterjee, W.L. Tsai, W.K. Lee, M.J. Wu, M. Jiao, K.C. Pan, C.L. Yi, C.L. Chung, K.T. Wong, Adv. Mater., 28 (2016) 6976-6983.
[85] D.H. Ahn, S.W. Kim, H. Lee, I.J. Ko, D. Karthik, J.Y. Lee, J.H. Kwon, Nat. Photonics, (2019) 1.

[86] M. Sarma, K.-T. Wong, ACS Appl. Mater. Interfaces, 10 (2018) 19279-19304.
[87] M. Colella, A. Danos, A.P. Monkman, J. Phys. Chem. Lett., 10 (2019) 793-798.
[88] M. Chapran, P.H. Pander, M. Vasylieva, G. Wiosna-Sałyga, J. Ulanski, F.B. Dias, P. Data, ACS Appl. Mater. Interfaces, (2019).
[89] B. Liang, J. Wang, Z. Cheng, J. Wei, Y. Wang, J. Phys. Chem. Lett., 10 (2019) 2811-2816.
[90] D.H. Ahn, H. Lee, S.W. Kim, D. Karthik, J. Lee, H. Jeong, J.Y. Lee, J.H. Kwon, ACS Appl. Mater. Interfaces, 11 (2019) 14909-14916.
[91] H. Sasabe, N. Toyota, H. Nakanishi, T. Ishizaka, Y.J. Pu, J. Kido, Adv. Mater., 24 (2012) 3212-3217.
[92] W.-Y. Hung, P.-Y. Chiang, S.-W. Lin, W.-C. Tang, Y.-T. Chen, S.-H. Liu, P.-T. Chou, Y.-T. Hung, K.-T. Wong, ACS Appl. Mater. Interfaces, 8 (2016) 4811-4818.
[93] H. Tanaka, T. Yasuda, K. Fujita, T. Tsutsui, Adv. Mater., 18 (2006) 2230-2233.
[94] F.B. Dias, T.J. Penfold, A.P. Monkman, Methods Appl. Fluoresc., 5 (2017) 012001.
[95] M.A. Baldo, D.F. O'Brien, Y. You, A. Shoustikov, S. Sibley, M.E. Thompson, S.R. Forrest, Nature, 395 (1998) 151-154.
[96] M. Baldo, M. Thompson, S. Forrest, Nature, 403 (2000) 750.
[97] E.W. Evans, Y. Olivier, Y. Puttisong, W.K. Myers, T.J. Hele, S.M. Menke, T.H. Thomas, D. Credgington, D. Beljonne, R.H. Friend, J. Phys. Chem. Lett., 9 (2018) 4053-4058.
[98] T. Ogiwara, Y. Wakikawa, T. Ikoma, J. Phys. Chem. A, 119 (2015) 3415-3418.
[99] T.-C. Lin, M. Sarma, Y.-T. Chen, S.-H. Liu, K.-T. Lin, P.-Y. Chiang, W.-T. Chuang, Y.-C. Liu, H.-F. Hsu, W.-Y. Hung, Nat. Commun., 9 (2018).
[100] A.M. Scott, M.R. Wasielewski, J. Am. Chem. Soc., 133 (2011) 3005-3013.
[101] N.J. Turro, V. Ramamurthy, V. Ramamurthy, J.C. Scaiano, Principles of molecular photochemistry: an introduction, University science books2009.
[102] R.A. Marcus, N. Sutin, Biochim. Biophys. Acta, 811 (1985) 265-322.
[103] C.-K. Moon, J.-S. Huh, J.-M. Kim, J.-J. Kim, Chem. Mater., 30 (2018) 5648-5654.
[104] S.Y. Kim, W.I. Jeong, C. Mayr, Y.S. Park, K.H. Kim, J.H. Lee, C.K. Moon, W. Brütting, J.J. Kim, Adv. Funct. Mater., 23 (2013) 3896-3900.
[105] N.R. Al Amin, K.K. Kesavan, S. Biring, C.-C. Lee, T.-H. Yeh, T.-Y. Ko, S.-W. Liu, K.-T. Wong, ACS Appl. Electron. Mater., 2 (2020) 1011-1019.
[106] X. Tang, L.-S. Cui, H.-C. Li, A.J. Gillett, F. Auras, Y.-K. Qu, C. Zhong, S.T. Jones, Z.-Q. Jiang, R.H. Friend, Nat. Mater., (2020) 1-7.
[107] T. Penfold, F. Dias, A. Monkman, ChemCommun, 54 (2018) 3926-3935.
[108] M. Flämmich, J. Frischeisen, D.S. Setz, D. Michaelis, B.C. Krummacher, T.D. Schmidt, W. Brütting, N. Danz, Org. Electron., 12 (2011) 1663-1668.
[109] P. Liehm, C. Murawski, M. Furno, B. Lüssem, K. Leo, M.C. Gather, Appl. Phys. Lett., 101 (2012) 253304.
[110] A. Graf, P. Liehm, C. Murawski, S. Hofmann, K. Leo, M.C. Gather, J. Mater. Chem. C, 2 (2014) 10298-10304.
[111] P. Kapusta, R. Erdmann, U. Ortmann, M. Wahl, J. Fluoresc., 13 (2003) 179-183.
[112] B. Valeur, M.N. Berberan-Santos, Molecular fluorescence: principles and applications, John Wiley & Sons2012.
[113] W. Nie, H. Tsai, R. Asadpour, J.-C. Blancon, A.J. Neukirch, G. Gupta, J.J. Crochet, M. Chhowalla, S. Tretiak, M.A. Alam, Science, 347 (2015) 522-525.
[114] K. Lin, J. Xing, L.N. Quan, F.P.G. de Arquer, X. Gong, J. Lu, L. Xie, W. Zhao, D. Zhang, C. Yan, Nature, 562 (2018) 245.

[115] J. Wang, C. Zhang, H. Liu, X. Liu, H. Guo, D. Sun, Z.V. Vardeny, Adv. Mater., (2019) 1904059.
[116] D. Sun, C. Zhang, M. Kavand, K.J. van Schooten, H. Malissa, M. Groesbeck, R. McLaughlin, C. Boehme, Z.V. Vardeny, arXiv preprint arXiv:1608.00993, (2016).
[117] J. Wang, C. Zhang, H. Liu, R. McLaughlin, Y. Zhai, S.R. Vardeny, X. Liu, S. McGill, D. Semenov, H. Guo, R. Tsuchikawa, V.V. Deshpande, D. Sun, Z.V. Vardeny, Nat. Commun., 10 (2019) 129.
[118] M. Zhou, J.S. Sarmiento, C. Fei, X. Zhang, H. Wang, J. Phys. Chem. Lett., (2020).
[119] O.H.-C. Cheng, D.H. Son, M. Sheldon, Nat. Photonics, 14 (2020) 365-368.
[120] D. Zhang, Y. Liu, M. He, A. Zhang, S. Chen, Q. Tong, L. Huang, Z. Zhou, W. Zheng, M. Chen, Nat. Commun., 11 (2020) 1-8.
[121] S. Yang, E. Vetter, T. Wang, A. Amassian, D. Sun, J. Phys. Mater., 3 (2020) 015012.
[122] H. Xu, P. Prabhakaran, S. Choi, M. Wang, K.-S. Lee, B. Hu, J. Phys. Chem. Lett., 11 (2019) 1-6.
[123] T. Dietl, Semicond. Sci. Technol., 17 (2002) 377.
[124] V. Lauter, H. Ambaye, R. Goyette, W.-T.H. Lee, A. Parizzi, Physica B Condens. Matter, 404 (2009) 2543-2546.
[125] F. Katmis, V. Lauter, F.S. Nogueira, B.A. Assaf, M.E. Jamer, P. Wei, B. Satpati, J.W. Freeland, I. Eremin, D. Heiman, Nature, 533 (2016) 513.
[126] J. Tornos, F. Gallego, S. Valencia, Y.H. Liu, V. Rouco, V. Lauter, R. Abrudan, C. Luo, H. Ryll, Q. Wang, Phys. Rev. Lett., 122 (2019) 037601.
[127] T.L. Meyer, A. Herklotz, V. Lauter, J.W. Freeland, J. Nichols, E.-J. Guo, S. Lee, T.Z. Ward, N. Balke, S.V. Kalinin, Phys. Rev. B, 94 (2016) 174432.
[128] V. Lauter-Pasyuk, Collection SFN, 7 (2007) s221-s240.
[129] F. Hellman, A. Hoffmann, Y. Tserkovnyak, G.S. Beach, E.E. Fullerton, C. Leighton, A.H. MacDonald, D.C. Ralph, D.A. Arena, H.A. Dürr, Rev. Mod. Phys., 89 (2017) 025006.
[130] S. Blundell, M. Gester, J. Bland, H. Lauter, V. Pasyuk, A. Petrenko, Phys. Rev. B, 51 (1995) 9395.
[131] V. Lauter-Pasyuk, H. Lauter, B. Toperverg, O. Nikonov, E. Kravtsov, M. Milyaev, L. Romashev, V. Ustinov, Physica B Condens. Matter, 283 (2000) 194-198.
[132] H. Zabel, K. Theis‐Bröhl, B.P. Toperverg, Handbook of magnetism and advanced magnetic materials, (2007).
[133] H. Lauter, V. Lauter-Pasyuk, B. Toperverg, L. Romashev, M. Milyaev, T. Krinitsina, E. Kravtsov, V. Ustinov, A. Petrenko, V. Aksenov, J. Magn. Magn. Mater, 258 (2003) 338-341.
[134] V. Lauter-Pasyuk, H. Lauter, B. Toperverg, O. Nikonov, E. Kravtsov, L. Romashev, V. Ustinov, J. Magn. Magn. Mater, 226 (2001) 1694-1696.
[135] M. Wang, H. Zou, J. Zhang, T. Wu, H. Xu, S. Haacke, B. Hu, J. Phys. Chem. Lett., 11 (2020) 3647-3652.
[136] M. Kepenekian, R. Robles, C. Katan, D. Sapori, L. Pedesseau, J. Even, ACS nano, 9 (2015) 11557-11567.
[137] M. Kim, J. Im, A.J. Freeman, J. Ihm, H. Jin, Proc. Natl. Acad. Sci. U. S. A., (2014) 201405780.
[138] Z. Chen, Y. Guo, E. Wertz, J. Shi, Adv. Mater., (2018) 1803514.
[139] X. Chen, H. Lu, Z. Li, Y. Zhai, P.F. Ndione, J.J. Berry, K. Zhu, Y. Yang, M.C. Beard, ACS Energy Lett., 3 (2018) 2273-2279.
[140] X. Hong, T. Ishihara, A. Nurmikko, Phys. Rev. B, 45 (1992) 6961.

[141] D. Giovanni, W.K. Chong, H.A. Dewi, K. Thirumal, I. Neogi, R. Ramesh, S. Mhaisalkar, N. Mathews, T.C. Sum, Sci. Adv., 2 (2016) e1600477.
[142] Y. Zhai, S. Baniya, C. Zhang, J. Li, P. Haney, C.-X. Sheng, E. Ehrenfreund, Z.V. Vardeny, Sci. Adv., 3 (2017) e1700704.
[143] D.B. Straus, S. Hurtado Parra, N. Iotov, J. Gebhardt, A.M. Rappe, J.E. Subotnik, J.M. Kikkawa, C.R. Kagan, J. Am. Chem. Soc., 138 (2016) 13798-13801.
[144] J. Byun, H. Cho, C. Wolf, M. Jang, A. Sadhanala, R.H. Friend, H. Yang, T.W. Lee, Adv. Mater., 28 (2016) 7515-7520.
[145] J.-C. Blancon, A.V. Stier, H. Tsai, W. Nie, C.C. Stoumpos, B. Traore, L. Pedesseau, M. Kepenekian, F. Katsutani, G. Noe, Nat. Commun., 9 (2018) 1-10.
[146] J. Cho, J.T. DuBose, P.V. Kamat, J. Phys. Chem. Lett., (2020).
[147] M.A. Becker, R. Vaxenburg, G. Nedelcu, P.C. Sercel, A. Shabaev, M.J. Mehl, J.G. Michopoulos, S.G. Lambrakos, N. Bernstein, J.L. Lyons, Nature, 553 (2018) 189.
[148] L. Lombez, D. Lagarde, P. Renucci, T. Amand, X. Marie, B. Liu, W. Wang, Q. Xue, D. Chen, Phys. Status Solidi C, 4 (2007) 475-477.
[149] D. Lagarde, A. Balocchi, P. Renucci, H. Carrère, F. Zhao, T. Amand, X. Marie, Z. Mei, X. Du, Q. Xue, Phys. Rev. B, 78 (2008) 033203.
[150] Y. Tang, W. Xie, K.C. Mandal, J.A. McGuire, C.-W. Lai, Phys. Rev. B, 91 (2015) 195429.

Appendix

Selected List of Publications

1. **M. Wang**, J. Lin, Y.-C. Hsiao, X. Liu, B. Hu. Investigating underlying mechanism in spectral narrowing phenomenon induced by microcavity in organic light emitting diodes. *Nature Communications*, **10**, (2019) 1614.
2. **M. Wang**, Y. H. Huang, K. S. Lin, T. H. Yeh, J. Duan, T. Y. Ko, S. W. Liu, K. T. Wong, B. Hu. Revealing the Cooperative Relationship between Spin, Energy, and Polarization Parameters toward Developing High-Efficiency Exciplex Light-Emitting Diodes. *Advanced Materials*, **31**, (2019) 1904114.
3. **M. Wang**, Y.-Z. Li, H.-C. Chen, C.-W. Liu, Y.-S. Chen, Y.-C. Lo, C.-S. Tsao, Y.-C. Huang, S.-W. Liu, K.-T. Wong, B. Hu. Unveiling the underlying mechanism of record-high efficiency organic near-infrared photodetector harnessing a single-component photoactive layer. *Materials Horizons*, **7**, (2020) 1171-1179.
4. **M. Wang**, T. Chatterjee, C. J. Foster, T. Wu, C.-L. Yi, H. Yu, K.-T. Wong, B. Hu. Exploring mechanisms for generating spin-orbital coupling through donor–acceptor design to realize spin flipping in thermally activated delayed fluorescence. *Journal of Materials Chemistry C*, **8**, (2020) 3395-3401.
5. **M. Wang**, H. Zou, J. Zhang, T. Wu, H. Xu, S. Haacke, B. Hu. Extremely Long Spin Lifetime of Light-emitting States in Quasi-2D Perovskites through Orbit-Orbit Interaction. *The Journal of Physical Chemistry Letters*, **11**, (2020) 3647-3652.
6. **M. Wang**, H. S. Shin, F. Zhou, H. Xu, P. Prabhakaran, B. Dryzhakov, H. Su, K.-S. Lee, B. Hu. Identifying Different Spin Mixing Channels Occurring in Charge-Transfer States. *The Journal of Physical Chemistry C*, **124**, (2020) 14832–14837.
7. H. Xu, **M. Wang** (Co-first), Z.-G. Yu, K. Wang, B. Hu. Magnetic field effects on excited states, charge transport, and electrical polarization in organic semiconductors in spin and orbital regimes. *Advances in Physics*, **68**, (2019) 49-121.
8. Y. Dou, **M. Wang** (Co-first), J. Zhang, H. Xu, B. Hu. Identifying Photoinduced Dipolar Polarization and Orbit–Orbit Interaction between Excitons in Organic–Inorganic Hybrid Perovskites. *Advanced Functional Materials*, (2020) 2003476.
9. **M. Wang**, H. Xu, T. Wu, H. Ambaye, J. Qin, J. Keum, I. N. Ivanov, V. Lauter, B. Hu, Optically Induced Static Magnetization in Metal Halide Perovskite for Spin-Related Optoelectronics. *Advanced Science*, accepted.
10. **M. Wang**, D. Luo, T.-H. Yeh, Y.-H. Huang, C.-L. Ko, W.-Y. Hung, S.-W. Liu, K.-T. Wong, B. Hu. Extended Polarization Memory on Light-Emitting Dipoles upon Reducing Coulomb Scattering in Exciplex-Hosted Iridium Complex System for Efficient OLEDs. Under review.

Vita

Miaosheng Wang received the B.S. degree in Materials Physics in June 2015 from the School of Physics and Technology at Wuhan University, China. Then he started to pursue his Ph.D. degree in the Department of Materials Science and Engineering at the University of Tennessee, Knoxville, USA, in August 2015. In Ph.D. studies, he has been working on the semiconductor fundamental physics for optoelectronics and spintronics through advanced optical, electrical, structural & magnetic characterizations. His dissertation research for a Ph.D. degree is focused on the spin effects of excited states in organic semiconductors and hybrid perovskites for optoelectronics and spintronics.